Measurements of CP Violation and K^0 Charge Radius using $K_L \to \pi^+\pi^-e^+e^-$ Decays.

Alexander Golossanov
Almaty, Kazakhstan

B.S., Kazakh State University, 1996

A Dissertation Presented to the Graduate Faculty
of the University of Virginia
in Candidacy for the Degree of
Doctor of Philosophy

Department of Physics
University of Virginia

May, 2005

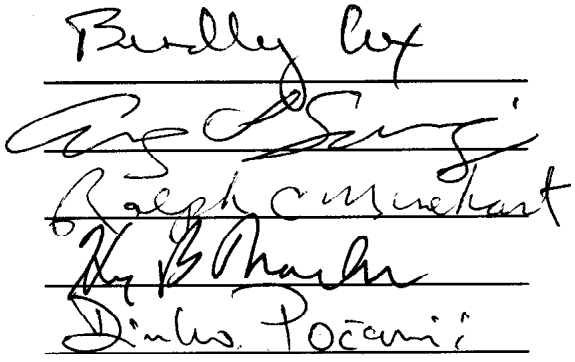

© Copyright by
Alexander Golossanov
All rights reserved
May 2005

Abstract

CP violation and K^0 charge radius were measured using $K_L \to \pi^+\pi^-e^+e^-$ decays. Specifically, a unique CP-violating decay-plane asymmetry was measured along with the parameters of individual contributions to the decay invariant amplitude: (*i*) CP-conserving magnetic dipole direct emission form factor, (*ii*) CP-conserving K^0 charge radius transition amplitude and (*iii*) an upper limit for the CP-violating electric dipole direct emission amplitude. The measurements were obtained from the data sample accumulated by KTeV experiment at Fermilab.

KTeV had two major goals: the measurement of direct CP violation parameter $Re\,(\varepsilon'/\varepsilon)$ and the study of rare kaon decays. The state of the art detector was constructed, commissioned, operated and maintained by an international collaboration of scientists from fourteen institutions. The $K_L \to \pi^+\pi^-e^+e^-$ data was accumulated over the 1997 and 1999 running periods. During that time hundreds of billions K_L decays took place in the KTeV fiducial decay region.

In the analysis of the rare decay mode $K_L \to \pi^+\pi^-e^+e^-$ 5241 candidate events were selected from the entire KTeV dataset. This data sample included an estimated background of $n = 204 \pm 14$ events. The data was analyzed using the method of maximum likelihood to obtain parameters of the decay invariant amplitude. Namely, coefficients of the magnetic dipole (M1) direct emission form

factor

$$\tilde{g}_{M1} = 1.11 \pm 0.12(stat) \pm 0.08(syst)$$

$$\frac{a_1}{a_2} = [-0.744 \pm 0.027(stat) \pm 0.032(syst)] \ (GeV)^2$$

and the amplitude of K^0 charge radius (CR) transition

$$|g_{CR}| = 0.163 \pm 0.014(stat) \pm 0.023(syst)$$

were measured; and an upper limit for the CP-violating electric dipole (E1) direct emission process

$$\frac{|g_{E1}|}{|g_{M1}|} < 0.04 \ (90\% \ CL) \ \ and \ \ \langle |g_{E1}| \rangle_{E^\star_\gamma} < 0.03 \ (90\% \ CL)$$

was determined. The result for g_{CR} allowed to determine the approximate value of the mean square charge radius of K^0

$$\left\langle r^2_{K^0} \right\rangle = [-0.077 \pm 0.007(stat) \pm 0.011(syst)] \ (fm)^2$$

in a novel way. Using the measured values for $\tilde{g}_{M1}$ and $\frac{a_1}{a_2}$ the average of $|g_{M1}|$ over the observed range of energies of the e^+e^- pair was calculated

$$\langle |g_{M1}| \rangle_{E^\star_\gamma} = 0.74 \pm 0.04 \ .$$

Finally, using the above values for the individual contributions in the invariant amplitude of the decay, the CP-violating decay-plane asymmetry was measured

$$\mathcal{A} = [13.6 \pm 1.4(stat) \pm 1.5(syst)] \ \% \ .$$

This is the most precise measurement of this unique asymmetry. It is the largest CP violation effect ever observed and the only one ever observed in an angular variable.

Dedicated to the memory of Anthony Ross "Tony" Barker (1961-2004)

Acknowledgements

The measurements presented here are based on the data set from KTeV experiment at Fermilab. I am grateful to my advisor, Bradley Cox, for giving me the opportunity to be a part of that collaboration and to play a leading role in the analysis of $K_L \to \pi^+\pi^-e^+e^-$ decays. I also thank him for his patience and advice during the writing of this thesis.

All the members of the KTeV collaboration and especially those from the University of Virginia High Energy Physics group contributed work, ideas and critique which drove and shaped the development of this analysis. My special thanks go to Alexander Ledovskoy for showing me the ropes and for his continuous help throughout this project. I thank Mike Arenton for helping with the computing and for answering many questions related to my work.

Many thanks to Diana Stokely, Valeri Jejer, Genya Kolomeisky, Pat Toale, Gloria Corti, Jason LaDue, Supriya Jaiswal, Ken Nelson, Melin Huang, Maxim Bychkov, Jason Ham, John Shields, Michael Ronquest, David Williams and Fred Ross for their help and companionship during the years spent at Fermilab and the University of Virginia. Finally, I am especially grateful to my mother, Lidia Sorokina, and my fiancee, Rebecca Edwards, for their constant help, love and support.

Alexander Golossanov

Charlottesville, Virginia

April 27, 2005

Contents

Chapter 1

Introduction

The aim of this thesis is to measure precisely a novel CP violation effect in the decay $K_L \to \pi^+\pi^- e^+ e^-$ as well as other features of the decay. The CP violation was discovered in 1964 by observing the decays of the long lived neutral kaon into two pions and has also been recently observed in the decays of B mesons. The origin of the phenomenon remains unknown despite the fact that it can be naturally accommodated in the formalism of the Standard Model.

There are three main reasons why CP violation is important. First, it provides connection to the existence of three families of quarks and leptons; second, it implies T violation if CPT is conserved; and third, it is needed to explain the matter-antimatter asymmetry in the universe.

Despite the fact that a long time has passed since the CP violation was discovered, there are only few measurements of this enigmatic phenomenon. The decay $K_L \to \pi^+\pi^- e^+ e^-$ offers another such measurement and is a valuable contribution to the study of CP violation.

The CP violation can be studied in decay $K_L \to \pi^+\pi^- e^+ e^-$ related to the decay $K_L \to \pi^+\pi^-\gamma^*$ through the Dalitz pair production $\gamma^* \to e^+e^-$. This possibility was suggested long ago [11] and has been recently investigated in detail by Sehgal et al [8, 9, 36]. The phenomenological model employed by Sehgal contains

the following contributions (see Figure 3.2) *(i)* a CP conserving amplitude associated with direct emission of a M_1 photon in $K_L \to \pi^+\pi^-\gamma$; *(ii)* an indirect CP violating amplitude related to the bremsstrahlung part of $K_L \to \pi^+\pi^-\gamma$; *(iii)* a charge radius pole contribution; *(iv)* the indirect CP violating amplitude associated with direct emission of an E_1 photon in $K_L \to \pi^+\pi^-\gamma$ and *(v)* direct CP violating term associated with the short-distance interaction $s\bar{d} \to e^+e^-$. The effects of direct CP violation are much smaller and are not accessible to KTeV. Therefore this contribution is neglected in this analysis.

The interference between the first two components generates a large CP violating asymmetry in the angle ϕ between the planes of e^+e^- and $\pi^+\pi^-$ in the K_L rest frame. Qualitatively, this effect was predicted shortly after the discovery of CP violation. In 1967 Dolgov and Ponomarev noted that rigorous conclusions about CP violation can be drawn from the *observation of an asymmetry* in the orientation of the e^+e^- and $\pi^+\pi^-$ planes in the decay $K_L \to \pi^+\pi^-e^+e^-$. However the measurement of this asymmetry required high statistics data samples of these decays. Indeed, this decay was not observed until detected by the KTeV experiment in 1998. The aforementioned work of Sehgal et al came just in time for the two upcoming kaon experiments: *KTeV* in United States and *NA48* in Europe. After discovering the decay in 1998 KTeV measured its branching ratio based on one day of data [34]. Then, in 2000 the asymmetry was measured based on a fraction of the KTeV total data set [67]. These measurements were confirmed later by experiments at KEK [68] and CERN [35]. The measurements presented in this thesis are based on the entire KTeV sample of $K_L \to \pi^+\pi^-e^+e^-$ decays, which to date is the largest in the world.

Besides the asymmetry, the decay $K_L \to \pi^+\pi^-e^+e^-$ includes a plethora of interesting physics topics. The measurement of $K_L \to \pi^+\pi^-e^+e^-$[34] requires the energy dependent form-factor for the M_1 photon emission. This favors the

vector meson dominance model for the hadronic electromagnetic current [13]. The knowledge of the precise values of the parameters in this form-factor is important for understanding of the hadronic structure of the kaon.

Furthermore, there is currently no explanation why the contribution from the direct emission E_1 process in $K_S \to \pi^+\pi^-\gamma$ is very small [8] compared to the direct emission M_1 contribution in $K_L \to \pi^+\pi^-\gamma$. The precise value of the M1 form-factor and the magnitude of the E1 contribution in K_L decay may help the understanding of this puzzle [10].

It has been pointed out long ago [20], that the decay $K_L \to \pi^+\pi^-e^+e^-$ also contains information about the structure of the neutral kaon via the charge radius pole contribution. The value of the form-factor for this process can be used to approximately determine the charge radius of the neutral kaon, which gives information about the charge distribution of the strange and down quarks composing the K^0[8].

Therefore, the study of the decay $K_L \to \pi^+\pi^-e^+e^-$ represents an opportunity to broaden our knowledge about the internal electromagnetic and hadronic structure of the neutral kaon and sheds more light on the intriguing phenomenon of CP violation.

The thesis is organized as follows. A review of kaon phenomenology and CP violation are presented in chapter 2. The phenomenological model for the decay $K_L \to \pi^+\pi^-e^+e^-$ is described in chapter 3. Chapter 4 discusses the KTeV experiment, including detector, trigger and data acquisition. The data mining, reconstruction of decays and selection of $K_L \to \pi^+\pi^-e^+e^-$ signal mode and $K_L \to \pi^+\pi^-\pi^0_D$ normalization mode statistical samples for the analysis are explained in chapter 5. The Monte Carlo simulation, based on the model described in chapter 3, is discussed in chapter 6. The analysis of the selected data samples is given in chapter 7, which describes the estimation of model parameters and

the measurement of the CP-violating asymmetry. This chapter also contains the calculation of the approximate value of the charge radius of the neutral kaon. The results of all the measurements are discussed in chapter 8.

Chapter 2

Neutral Kaons and CP Violation

In this chapter the neutral kaon system and the phenomenon of CP violation are briefly discussed. The literature on both subjects is vast and only the basic results are presented here. The extensive treatment and references for these topics are available in recently published monographs [3, 4, 5, 6].

2.1 The Neutral Kaons

The discovery of *neutral kaons* was announced in 1947 as the result of the experiments studying the interaction of cosmic rays with matter. These particles are *produced in the strong interactions*. The typical reaction is

$$\pi^- + p \rightarrow K^0 + \Lambda.$$

This is an example of the *associated production*, which is the fact that kaons are always produced in association with another particle (in this case $\Lambda-$hyperon). The attempt to explain this fact led to the introduction of the new quantum number called *strangeness*. In the above reaction the produced particles are assigned the opposite values of strangeness and are produced in pairs due to the fact that strangeness is conserved in the strong interaction.

The assignment of strangeness value $S = 1$ to K^0 makes it impossible for that particle to be it's own antiparticle, since the antiparticle would have the opposite values of *all* the quantum numbers, including the strangeness. Therefore there have to be two bound states corresponding to the neutral kaon with opposite strangeness

$$K^0 \neq \bar{K}^0.$$

These two particles can be distinguished in the strong interaction processes. For example, the reactions

$$K^0 + p \rightarrow n + K^+, \qquad \bar{K}^0 + n \rightarrow p + K^-$$

are possible, but the reaction

$$\bar{K}^0 + p \rightarrow n + K^+$$

has not been observed and is impossible because it would violate strangeness conservation. Thus there are two neutral kaons: K^0 and it's antiparticle $\bar{K}^0$. They have opposite values of strangeness and are produced in the strong interactions.

The *decay of K-mesons* occurs via the weak interaction, which does not conserve strangeness. This fact makes it impossible to distinguish K^0 and $\bar{K}^0$ by observing their decays, since the final states are identical for both particles. These two states can mix due to the presence of strangeness violating weak interaction and the decay of the whole K^0- $\bar{K}^0$ system must be considered. The quantum mechanical formalism for such decays leads to the introduction of two new weak eigenstates with well defined masses and decay rates

$$\left|K_1^0\right\rangle \equiv \frac{1}{\sqrt{2}}\left(\left|K^0\right\rangle + \left|\bar{K}^0\right\rangle\right), \qquad \left|K_2^0\right\rangle \equiv \frac{1}{\sqrt{2}}\left(\left|K^0\right\rangle - \left|\bar{K}^0\right\rangle\right)$$

which are the eigenstates of the symmetry operation, called *CP*,

$$CP\left|K_1^0\right\rangle = \left|K_1^0\right\rangle, \qquad CP\left|K_2^0\right\rangle = -\left|K_2^0\right\rangle.$$

The symbol $\boldsymbol{CP}$ stands for combined operation of *parity* and *charge conjugation* transformations. In general, the parity transformation $\boldsymbol{P}$ reverses the sign of all coordinates and changes the sign of the intrinsic parities of the bound states. The charge conjugation $\boldsymbol{C}$ changes particles to antiparticles and, therefore the sign of *all* the charges involved in a particular state. The effect of $\boldsymbol{CP}$ transformation on the neutral kaons can be (there is a freedom to choose the phase) defined as follows

$$\boldsymbol{CP}\left|\boldsymbol{K^0}\right\rangle \equiv \left|\bar{\boldsymbol{K}}^{\boldsymbol{0}}\right\rangle, \qquad \boldsymbol{CP}\left|\bar{\boldsymbol{K}}^{\boldsymbol{0}}\right\rangle \equiv \left|\boldsymbol{K^0}\right\rangle.$$

which fixes the relative phases between $\boldsymbol{K^0}$ and $\bar{\boldsymbol{K}}^{\boldsymbol{0}}$.

To summarize, there are two pairs of states: strong interaction eigenstates $\left(\boldsymbol{K^0},\ \bar{\boldsymbol{K}}^{\boldsymbol{0}}\right)$ and weak interaction eigenstates, which in the absence of CP violation are denoted as $\left(\boldsymbol{K_1^0},\ \boldsymbol{K_2^0}\right)$. These eigenstates correspond to different representations of the same physical system — neutral kaon. The $\boldsymbol{K_1^0}$ and $\boldsymbol{K_2^0}$ are each own antiparticle and have different masses and well defined decay rates. On the other hand $\boldsymbol{K^0}$ and $\bar{\boldsymbol{K}}^{\boldsymbol{0}}$ are antiparticles of each other and can be distinguished through their production, but have no definite decay rate. Each representation can be expressed in terms of the other:

$$\begin{aligned}\left|\boldsymbol{K_1^0}\right\rangle &= \frac{\boldsymbol{1}}{\sqrt{\boldsymbol{2}}}\left(\left|\boldsymbol{K^0}\right\rangle + \left|\bar{\boldsymbol{K}}^{\boldsymbol{0}}\right\rangle\right)\\ \left|\boldsymbol{K_2^0}\right\rangle &= \frac{\boldsymbol{1}}{\sqrt{\boldsymbol{2}}}\left(\left|\boldsymbol{K^0}\right\rangle - \left|\bar{\boldsymbol{K}}^{\boldsymbol{0}}\right\rangle\right)\end{aligned} \tag{2.1}$$

$$\begin{aligned}\left|\boldsymbol{K^0}\right\rangle &= \frac{\boldsymbol{1}}{\sqrt{\boldsymbol{2}}}\left(\left|\boldsymbol{K_1^0}\right\rangle + \left|\boldsymbol{K_2^0}\right\rangle\right)\\ \left|\bar{\boldsymbol{K}}^{\boldsymbol{0}}\right\rangle &= \frac{\boldsymbol{1}}{\sqrt{\boldsymbol{2}}}\left(\left|\boldsymbol{K_1^0}\right\rangle - \left|\boldsymbol{K_2^0}\right\rangle\right)\end{aligned} \tag{2.2}$$

2.2 CP Violation

The weak interaction violates several conservation laws, while the strong interaction respects all known conservation laws. In addition to already mentioned strangeness non-conservation the weak interaction violates conservation laws related to the transformations of parity P, charge conjugation C and the combined operation of CP.

The CP violation occurs in a peculiar way. Both P and C are violated maximally, whereas CP is almost completely conserved in the weak interaction processes. This peculiarity of CP violation is the reason for using 2 sets of notation for the neutral kaon system K^0-$\bar{K}^0$. K_1^0 and K_2^0 correspond to the short lived and long lived states under the assumption that CP is conserved. When CP violation of the neutral kaons is taken into account, physical states called K_L and K_S, respectively must be introduced. These states differ only slightly from the CP eigenstates due to small admixtures of the opposite CP eigenstate leading to the CP violating decays. This mixing is quantified by parameter ε :

$$|K_S\rangle = \left|K_1^0\right\rangle + \varepsilon \left|K_2^0\right\rangle, \qquad |K_L\rangle = \left|K_2^0\right\rangle + \varepsilon \left|K_1^0\right\rangle \tag{2.3}$$

where the normalization has been neglected. The equations (2.3) and (2.2) result in the following relationships:

$$\begin{aligned} |K_L\rangle &= \frac{1}{\sqrt{2}}\left((1+\varepsilon)\left|K^0\right\rangle + (1-\varepsilon)\left|\bar{K}^0\right\rangle\right) \\ |K_S\rangle &= \frac{1}{\sqrt{2}}\left((1+\varepsilon)\left|K^0\right\rangle - (1-\varepsilon)\left|\bar{K}^0\right\rangle\right) \end{aligned} \tag{2.4}$$

and

$$\begin{aligned} \left|K^0\right\rangle &= \frac{1}{\sqrt{2}}\left((1+\varepsilon)|K_S\rangle + (1-\varepsilon)|K_L\rangle\right) \\ \left|\bar{K}^0\right\rangle &= \frac{1}{\sqrt{2}}\left((1+\varepsilon)|K_S\rangle - (1-\varepsilon)|K_L\rangle\right) \end{aligned} \tag{2.5}$$

where again the normalization has been neglected. Thus the CP violation can occur due to the the small admixture of CP-odd and CP-even components in the K_L and K_S states. This phenomenon is referred to as *indirect violation* or *CP violation in the mixing* as opposed to *direct CP violation* or *CP violation in the amplitudes* when it occurs in the decay amplitudes themselves, e.g. when K_2^0 decays directly into two pions.

The parameter ε of the indirect CP violation is of the order 10^{-3}. The parameter $Re\,(\varepsilon'/\varepsilon)$ of the direct CP violation is of the order 10^{-3}, making the direct CP violation effects 3 orders of magnitude smaller than the indirect ones. Both parameters ε and $Re\,(\varepsilon'/\varepsilon)$ have been accurately measured:

$$|\varepsilon| = (2.284 \pm 0.014) \times 10^{-3} \tag{2.6}$$

$$Re\left(\frac{\varepsilon'}{\varepsilon}\right) = (1.67 \pm 0.26) \times 10^{-3} \tag{2.7}$$

The effects related to the direct CP violation are too small to be studied with the KTeV $K_L \to \pi^+\pi^- e^+ e^-$ data sample and are not considered in this thesis. **All future references to CP violation imply the indirect CP violation only**.

There are only a few experimental measurements of the CP violation. In the kaon system the CP violation has been observed in the decay $K_L \to \pi^+\pi^-$ and as charge asymmetry in the decays $K_L \to \pi^\pm l^\mp \nu$, where l refers to either electron or muon. The observables are defined as

$$\begin{aligned} \eta_{+-} &= \frac{A\,(K_L \to \pi^+\pi^-)}{A\,(K_S \to \pi^+\pi^-)} \\ &= |\eta_{+-}|\, e^{i\phi_{+-}}\,, \end{aligned} \tag{2.8}$$

$$\begin{aligned} \eta_{00} &= \frac{A\,(K_L \to \pi^0\pi^0)}{A\,(K_S \to \pi^0\pi^0)} \\ &= |\eta_{00}| e^{i\phi_{00}} \end{aligned} \tag{2.9}$$

and

$$\delta_L = \frac{\Gamma(K_L \to \pi^- l^+ \nu) - \Gamma(K_L \to \pi^+ l^- \nu)}{\Gamma(K_L \to \pi^- l^+ \nu) + \Gamma(K_L \to \pi^+ l^- \nu)} \tag{2.10}$$

All these parameters have been measured with high precision [1]. The measurement of η_{+-} (2.8)

$$\begin{aligned} |\eta_{+-}| &= (2.288 \pm 0.014) \times 10^{-3} \\ \phi_{+-} &= (43.5 \pm 0.7)^\circ \end{aligned} \tag{2.11}$$

is relevant to this thesis, since this parameter enters the expression for the decay amplitude of the decay $K_L \to \pi^+\pi^- e^+ e^-$ (chapter 3).

Chapter 3

Rare Decay $K_L \to \pi^+\pi^-e^+e^-$

The decay $K_L \to \pi^+\pi^-e^+e^-$ represents a valuable contribution to the study of CP violation by providing a measurement of CP-violating asymmetry resulting from the interference of CP-violating and CP-conserving components of the underlying decay $K_L \to \pi^+\pi^-\gamma$. This asymmetry is encrypted in the polarization state of the photon and is transported through Dalitz pair production $\gamma^* \to e^+e^-$ into the decay $K_L \to \pi^+\pi^-e^+e^-$, where it can be observed and measured.

This chapter begins with the discussion of the decay $K_L \to \pi^+\pi^-\gamma$, which leads to the phenomenological model of the decay $K_L \to \pi^+\pi^-e^+e^-$. Then the connection between the photon polarization and the asymmetry is explained and the definition of the asymmetry is given. The discussion is based mostly on the recent development of the phenomenological model by L .Sehgal et al [8, 9, 36] and earlier work performed by various authors including A. Dolgov, L. Ponomarev, G. Costa, P. Kabir and H. Chew [11, 26, 12].

3.1 The $K_L \to \pi^+\pi^-\gamma$ Decay Contributions

The decays $K_L \to \pi^+\pi^-e^+e^-$ and $K_L \to \pi^+\pi^-\gamma$ have been long discussed theoretically in connection to the CP violation observed in the decay $K_L \to \pi^+\pi^-$, see section 2.2. The total invariant amplitude for the radiative decay

$K_L \to \pi^+\pi^-\gamma$ can be a function of all possible gauge and Lorenz invariant combinations of the 4-vectors describing the decay. If the momenta of the involved particles are labeled as

$$K_L(P) \to \pi^+\left(p^+\right)\pi^-\left(p^-\right)\gamma(k,\ \varepsilon) \tag{3.1}$$

with ε being the photon polarization vector, then the only possible invariants up to the third order in momenta are (see [14] and Section 3.1 in [15]):

$$\frac{p^+\cdot\varepsilon}{p^+\cdot k} - \frac{p^-\cdot\varepsilon}{p^-\cdot k} \tag{3.2}$$

$$\epsilon_{\mu\nu\rho\sigma}k^\nu p^{+\rho}p^{-\sigma}\varepsilon^\mu \tag{3.3}$$

$$\left(p^-\cdot k\right)\left(p^+\cdot\varepsilon\right) - \left(p^+\cdot k\right)\left(p^-\cdot\varepsilon\right) \tag{3.4}$$

Conventionally all the individual contributions to the total invariant amplitude are divided into electric and magnetic terms. The electric term has contributions from the internal bremsstrahlung and direct emission processes, whereas the magnetic term is due exclusively to the direct emission process, i.e.

$$\mathcal{M}\left(K_L \to \pi^+\pi^-\gamma\right) = \mathcal{M}_{IB} + \mathcal{M}_E + \mathcal{M}_M \tag{3.5}$$

where the term

$$\mathcal{M}_{IB} = e\,|f_S|\,\eta_{+-}\left[\frac{p^+\cdot\varepsilon}{p^+\cdot k} - \frac{p^-\cdot\varepsilon}{p^-\cdot k}\right] \tag{3.6}$$

represents the amplitude due to the of *internal bremsstrahlung* radiation from one of the pions in the underlying CP violating decay $K_L \to \pi^+\pi^-$; the factor $|f_S|$ is defined by

$$\Gamma\left(K_S \to \pi^+\pi^-\right) = \frac{|f_S|^2}{16\pi M_K}\left[1 - \frac{4M_\pi^2}{M_K^2}\right]^{\frac{1}{2}}, \tag{3.7}$$

the η_{+-} is given by equations (2.8) and (2.11). The last two terms in (3.5) are the *direct emission* amplitudes for the radiation of electric and magnetic type:

$$\begin{aligned}\mathcal{M}_M &= e\,|f_S|\,G_M\epsilon_{\mu\nu\rho\sigma}k^\nu p^{+\rho}p^{-\sigma}\varepsilon^\mu \\ \mathcal{M}_E &= e\,|f_S|\,G_E\left[\left(p^-\cdot k\right)\left(p^+\cdot\varepsilon\right) - \left(p^+\cdot k\right)\left(p^-\cdot\varepsilon\right)\right]\end{aligned} \tag{3.8}$$

where the form factors $G_{M,E}$ are the functions of $(p^+ + p^-) \cdot k$ and

$$s_\pi = \left(p^+ + p^-\right)^2 \tag{3.9}$$

and can be expanded in terms of electric and magnetic multipoles for the photon states with well defined parity and angular momentum.

Generally, the quantum state of a photon can be given in terms of the photon momentum and helicity $(\vec{p},\ \lambda)$. The helicity can have only two values $\lambda = \pm 1$, corresponding to photon with the right/left circular polarization. Alternatively, the total angular momentum and parity can be given. There is an accepted terminology to describe the states of a photon with certain total angular momentum and parity. A photon with a total angular momentum j and parity $(-1)^j$ is called $Ej-photon$ (or electric $2j$-pole), and a photon with a total angular momentum j and parity $(-1)^{j+1}$ is called $Mj-photon$ (or magnetic $2j$-pole).

The photon eigenvalue for the charge conjugation operator is $C = -1$ and therefore the electric and magnetic dipole states can be described as follows:

$$\begin{aligned} E1-photon: &\quad j=1,\ P=-1,\ CP=+1 \\ M1-photon: &\quad j=1,\ P=1,\ CP=-1 \end{aligned} \tag{3.10}$$

A virtual photon has the same quantum numbers as a real photon, except that its mass and longitudinal momentum component are non-zero.

The lowest order contributions to the amplitudes in equation (3.5) correspond to treating the form factors in the equations (3.8) as constants and taking into account only the following physical processes:

1. $\mathcal{M}_{IB}$: CP-violating *bremsstrahlung radiation* of E1 photon with CP=+1.
2. $\mathcal{M}_{E1}$: CP-violating *direct emission* of E1 photon with CP=+1.
3. $\mathcal{M}_{M1}$: CP-conserving *direct emission* of M1 photon with CP=-1.

In this approximation the amplitude (3.5) and it's contributions (3.6) and (3.8) can be expressed as follows, (see figure 3.1 for the diagrams corresponding to all four contributions):

$$\mathcal{M}\left(K_L \to \pi^+\pi^-\gamma\right) = \mathcal{M}_{IB} + \mathcal{M}_{E1} + \mathcal{M}_{M1} \tag{3.11}$$

where

$$\mathcal{M}_{IB} = g_{IB}\left[\frac{p_\mu^+}{p^+\cdot k} - \frac{p_\mu^-}{p^-\cdot k}\right]\varepsilon^{\,\mu} \tag{3.12}$$

$$\mathcal{M}_{M1} = \frac{g_{M1}}{M_K^4}\epsilon_{\mu\nu\rho\sigma}k^\nu p^{+\rho}p^{-\sigma}\varepsilon^{\,\mu} \tag{3.13}$$

$$\mathcal{M}_{E1} = \frac{g_{E1}}{M_K^4}\left[\left(p^-\cdot k\right)p_\mu^+ - \left(p^+\cdot k\right)p_\mu^-\right]\varepsilon^{\,\mu} \tag{3.14}$$

with the common factor $e\,|f_S|$ in (3.6) and (3.8) omitted. The relative strength of each contribution is given by the complex coefficients:

$$g_{IB} = |\eta_{+-}|\, e^{i\phi_{+-}} e^{i\delta_0\left(M_K^2\right)} \tag{3.15}$$

$$g_{M1} = i\,|g_{M1}|\, e^{i\delta^1(s_\pi)} \tag{3.16}$$

$$g_{E1} = |g_{E1}|\, e^{i\phi_{+-}} e^{i\delta_1(s_\pi)} \tag{3.17}$$

where $\delta_0 \equiv \delta_0^0$ and $\delta_1 \equiv \delta_1^1$. The functions $\delta_J^I(s_\pi)$ are the strong interaction phase shifts of the $\pi^+\pi^-$ system in the state with isospin I and angular momentum J. The variable s_π is defined by equation (3.9) and represents the square of the invariant mass for the $\pi^+\pi^-$ system. The phase shift $\delta_0\left(M_K^2\right)$ for the pions in the *s-wave* state at $s_\pi = M_K^2$ is present in the amplitude (3.16) due to the Low theorem [24] for the bremsstrahlung of low energy photons. The *p-wave* pion state phase shift $\delta_1(s_\pi)$ is determined by the Watson theorem [25] according to which the direct emission of M1 photon produces a $\pi^+\pi^-$ pair in the $J = 1$ p-wave state. The factor i in the amplitude (3.17) is the consequence of requiring CPT invariance [26].

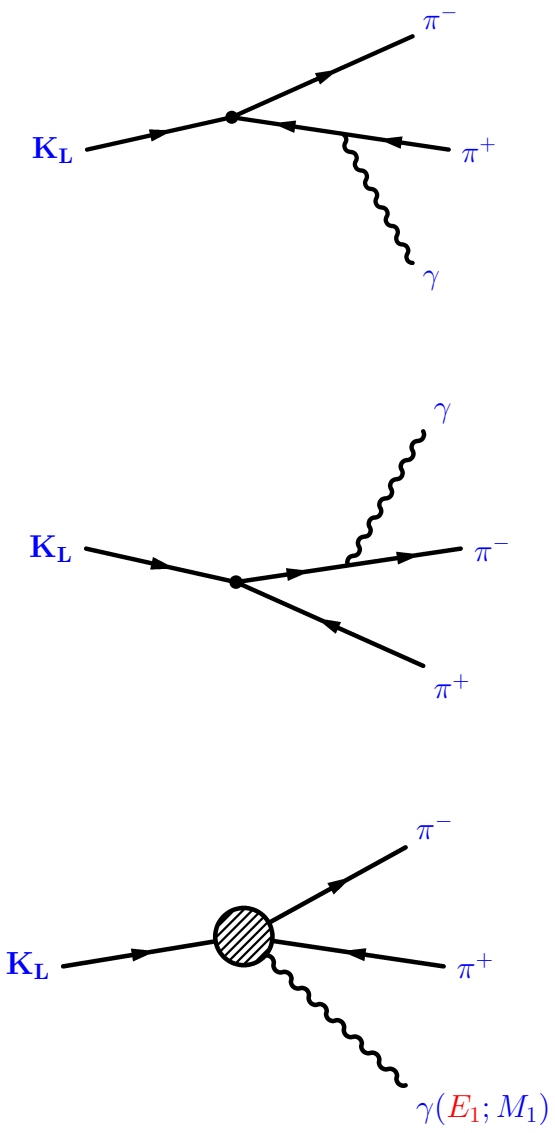

Figure 3.1: Diagrams illustrating the contributions to the decay $K_L \to \pi^+\pi^-\gamma$: CP-violating internal bremsstrahlung (top and middle); CP-violating $E1$ and CP-conserving $M1$ direct emission processes (bottom).

Introducing the two independent variables ω (the photon energy in the K_L rest frame) and θ (the angle between π^+ and γ in the $\pi^+\pi^-$ rest frame) results [36] in the following expressions for the bremsstrahlung and magnetic contributions (the $\mathcal{M}_{E1}$ contribution is much smaller and makes no difference for the expression (3.21)):

$$\mathcal{M}_{IB} = \left(\frac{2M_K}{\omega}\right) \frac{g_{IB}}{1-\beta^2 cos^2\theta} \tag{3.18}$$

$$\mathcal{M}_{M1} = g_{M1} \tag{3.19}$$

where the common factor $e\,|f_S|$ was omitted and

$$\beta = \sqrt{1 - \frac{4M_\pi^2}{s_\pi}} \tag{3.20}$$

with invariant mass squared s_π given by equation (3.9). The differential decay rate for $K_L \to \pi^+\pi^-\gamma$ before summing over photon polarizations has the form [36]

$$\frac{d\Gamma}{d\phi} \sim 1 + A sin^2\phi + B cos^2\phi + C sin 2\phi \tag{3.21}$$

where ϕ is the angle between polarization vector ε and the normal to the $\pi^+\pi^-$ plane in the decay $K_L \to \pi^+\pi^-\gamma$. The coefficient A is proportional to the bremsstrahlung energy dependent amplitude (3.18) squared and B is proportional to the M1 constant amplitude (3.19) squared, whereas C is proportional to the product of the two. The implications of the expression (3.21) will be discussed in section 3.3 in connection with the CP-violating asymmetry observed in the decay $K_L \to \pi^+\pi^- e^+ e^-$.

3.2 $K_L \to \pi^+\pi^- e^+ e^-$ Phenomenological Model

The *standard model* of particle physics provides several theoretical methods to calculate the invariant amplitude of a hadronic decay: (*i*) direct numerical calculation can be done using *lattice QCD*; (*ii*) *perturbative QCD* can be used in the high

energy limit; (*iii*) in the low energy limit the *chiral perturbation theory* becomes applicable; (*iv*) finally, a *phenomenological model* can be constructed based on the experimental observations and general theoretical considerations.

Lattice QCD calculations for $K_L \to \pi^+\pi^- e^+ e^-$ are not yet available and perturbative QCD is not applicable. Several models based on the chiral perturbation theory calculations are available [27, 28, 29, 30], but are not considered in this thesis.

The invariant amplitude for $K_L \to \pi^+\pi^- e^+ e^-$ used in this analysis was calculated within the phenomenological model developed by L. Sehgal et al [8, 9]. and is analogous to the invariant amplitude for $K_L \to \pi^+\pi^-\gamma$ (3.11)

$$\mathcal{M}\left(K_L \to \pi^+\pi^- e^+ e^-\right) = \mathcal{M}_{IB} + \mathcal{M}_{M1} + \mathcal{M}_{E1} + \mathcal{M}_{CR} \tag{3.22}$$

See figure 3.2 for the diagrams corresponding to all four contributions.

The first three terms in the equation (3.22) are obtained from the corresponding contributions to $K_L \to \pi^+\pi^-\gamma$ (see equations (3.12) to (3.17)) by replacing photon polarization vector ε with electromagnetic current $\frac{e}{k^2}\bar{u}(k^+)\gamma^\mu v\,(k^-)$. The last term represents the *CP-conserving pole contribution* arising from the $J = 0$ transition $K_L \to K_S\gamma^\star$ present only in the case of the virtual photon, when the photon momentum squared $k^2 \neq 0$. This transition was first considered by Zeldovich [19]. Later the possibility of determining the radius of the neutral kaon using it's contribution to the decay $K_L \to \pi^+\pi^- e^+ e^-$ was studied by Kondratyuk, Ponomarev and Zakharov [20]. In the framework of the employed phenomenological model this pole amplitude $\mathcal{M}_{CR}$ is approximated [23] by the charge radius diagram shown in the figure 3.2 and expressed as follows:

$$\mathcal{M}_{CR} \;=\; \frac{g_{CR}}{M_K^2}\left[k^2 P_\mu - (P\cdot k)\,k_\mu\right]\frac{e\,|f_S|\,\frac{e}{k^2}\bar{u}(k^+)\gamma^\mu v\,(k^-)}{k^2 - 2P\cdot k} \tag{3.23}$$

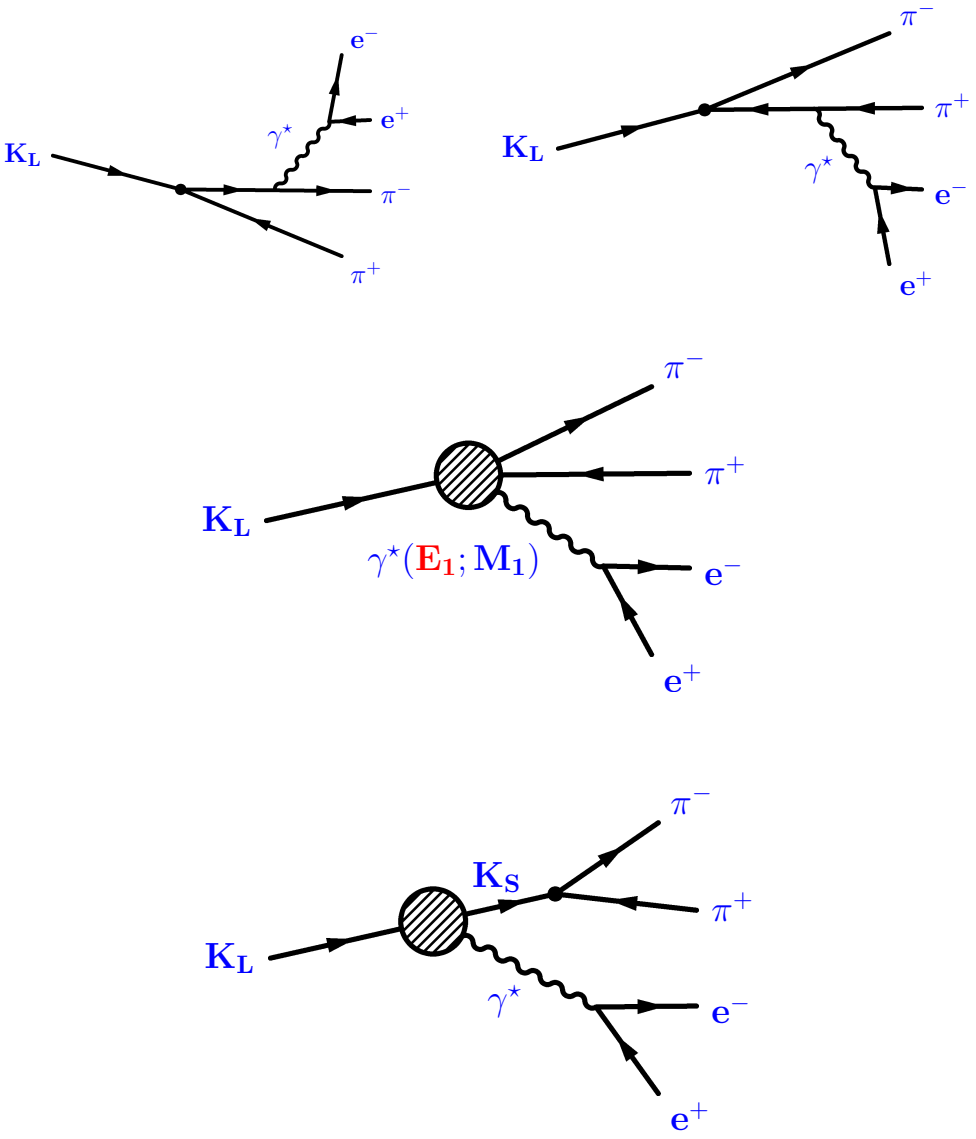

Figure 3.2: The contributions to the decay $K_L \to \pi^+\pi^- e^+ e^-$: CP-violating internal bremsstrahlung (top); CP-violating $E1$ and CP-conserving $M1$ direct emission processes (middle); CP-conserving charge radius diagram (bottom). Compare with analogous diagrams for decay $K_L \to \pi^+\pi^-\gamma$ on figure 3.1.

where $|f_S|$ defined by equation (3.7). The complex coefficient g_{CR} is given by

$$g_{CR} = |g_{CR}|\, e^{i\delta_0(s_\pi)} = -\frac{1}{3}\left\langle r^2_{K^0}\right\rangle M_K^2 e^{i\delta_0(s_\pi)} \tag{3.24}$$

where $\left\langle r^2_{K^0}\right\rangle$ stands for the mean square charge radius of K^0 and the strong interaction phase shift δ_0 function corresponds to the *s-wave* state of the pions with the invariant mass squared s_π (3.9).

The phenomenological model described above was extended and refined in several ways. First, the form factor $|g_{M1}|$ was expanded to include the dependence on the energy of the electron positron pair:

$$|g_{M1}| = \tilde{g}_{M1}\left[1 + \frac{a_1/a_2}{\left(M_\rho^2 - M_K^2\right) + 2M_K\left(E_{e^+} + E_{e^-}\right)}\right] \tag{3.25}$$

This [1] expression for the form factor was suggested [14] in the analysis of the decay $K_L \to \pi^+\pi^-\gamma$ on the basis of vector meson dominance model [13], and was found to be necessary to explain both $K_L \to \pi^+\pi^-\gamma$ [16] and $K_L \to \pi^+\pi^- e^+ e^-$ [34] data. Here $\tilde{g}_{M1}$ is the constant defining the strength of M1 contribution. The parameter a_1/a_2 depends on the angle θ_P for the octet-singlet mixing of the pseudoscalar mesons $\eta - \eta'$ (see [14] and Section 13.2 in [1]). The M_ρ is the mass of the ρ meson.

Next, the values for the final state interaction $\pi^+\pi^-$ phase shifts δ_0^0 and δ_1^1 (see discussion after equation (3.17)) were parametrized by functions based on fits [33] to a K_{e4} data sample of 400,000 events from the experiment BNL-E865 [32] (figure 3.3). These functions for the phase shifts depend on the invariant mass of the $\pi^+\pi^-$ system $M_{\pi\pi} = \sqrt{s_\pi}$, see equation (3.9):

$$\delta_J^I = arctan\left\{\sqrt{1 - \frac{4M_\pi^2}{s_\pi}}\cdot q^{2J}\cdot f\cdot\left(\frac{4M_\pi^2 - s_J^I}{s_\pi - s_J^I}\right)\right\} \tag{3.26}$$

[1] In case of $K_L \to \pi^+\pi^-\gamma$ the sum of electron energies is replaced by the energy of the photon.

where the δ_J^I is in radians,

$$f = \left(A_J^I + B_J^I q^2 + C_J^I q^4 + D_J^I q^6\right) \tag{3.27}$$

and

$$q = \sqrt{\frac{s_\pi}{4M_\pi^2} - 1} \tag{3.28}$$

is the pion momentum in $\pi^+\pi^-$ rest frame. The numerical values of the coefficients are:

$$\begin{aligned} A_0^0 = 0.220; \quad A_1^1 = 0.379 \times 10^{-1} \\ B_0^0 = 0.268; \quad B_1^1 = 0.140 \times 10^{-4} \\ C_0^0 = -0.139 \times 10^{-1}; \quad C_1^1 = -0.673 \times 10^{-4} \\ D_0^0 = -0.139 \times 10^{-2}; \quad D_1^1 = 0.163 \times 10^{-7} \end{aligned} \tag{3.29}$$

$$s_0^0 = 36.77 M_\pi^2; \quad s_1^1 = 30.72 M_\pi^2 \tag{3.30}$$

Finally, radiative corrections must be applied to the charged particles in the final state of the decay $K_L \to \pi^+\pi^-e^+e^-$. The package PHOTOS [31] was used to evaluate these radiative corrections. The default configuration was used except for the value of the infrared cut-off parameter XPHCUT $= \frac{2 \cdot E_{min}}{M_{parent}}$ (see [31]). This parameter was XPHCUT $= 0.0000143$ which corresponds to photon cut-off $E_{min} = 1\ KeV$ in case of pions, i.e. when $M_{parent} = M_\pi$.

The partial decay width for the decay $K_L \to \pi^+\pi^-e^+e^-$ is given by

$$\Gamma(K_L \to \pi^+\pi^-e^+e^-) = \int d\Gamma = \int_V \left(\sum_{spins} \left|\mathcal{M}^2\right| \right) dV \tag{3.31}$$

where the phase-space volume element

$$dV = \frac{d^3p_{\pi^+}}{2E_{\pi^+}} \frac{d^3p_{\pi^-}}{2E_{\pi^-}} \frac{d^3p_{e^+}}{2E_{e^+}} \frac{d^3p_{e^-}}{2E_{e^-}} \delta^{(4)}\left(p_f - p_i\right) \tag{3.32}$$

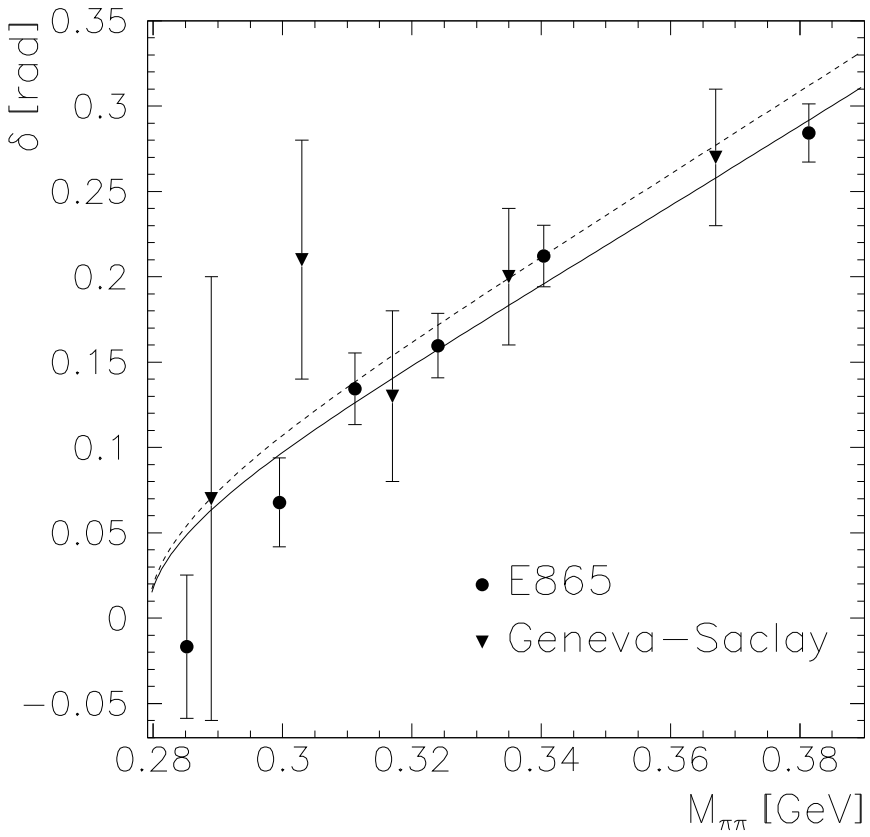

Figure 3.3: The strong interaction phase shift function $\delta_0 - \delta_1$ obtained from a sample of more than 400,000 K_{e4} decays by E865 collaboration [32]. The triangles show older data. The fits to both data sets are shown as well.

and the square of the total invariant amplitude (3.22) is summed over the spins of all the particles in the final state. The particle momenta and energies appearing in the expression (3.32) are not independent. In general, the total number of degrees of freedom n, required to describe a many-body decay in the rest frame of the decaying particle, is given by the expression

$$n = 3N - 10, \text{ for N} \geq 4 \tag{3.33}$$

where N is the total number of particles involved in the process (including the decaying particle); and 10 comes from 4 conservation laws and 6 degrees of freedom to fix the kaon rest frame in space. In this model for the $K_L \to \pi^+\pi^- e^+ e^-$ the 5 independent variables, chosen to describe the phase-space point x, were:

$$x \equiv (\phi, cos\theta_e, cos\theta_\pi, M_{ee}, M_{\pi\pi}) \tag{3.34}$$

where $M_{ee} \equiv \sqrt{s_e}$ and $M_{\pi\pi} \equiv \sqrt{s_\pi}$ (see (3.9)) are the invariant masses of e^+e^- and $\pi^+\pi^-$ systems and angles are defined in the figure 3.4.

Using these variables the $K_L \to \pi^+\pi^- e^+ e^-$ differential decay rate can be written as

$$d\Gamma = \mu\left(s_\pi, s_e, cos\theta_\pi, cos\theta_e, \phi\right) ds_\pi ds_e dcos\theta_\pi dcos\theta_e d\phi \tag{3.35}$$

where μ is the decay *matrix element*, i.e. the spin-averaged total invariant amplitude squared expressed in terms of the five independent variables (3.34) with all the necessary coefficients. Integration over all variables except ϕ leads [8] to the following dependence for the differential decay rate in this variable:

$$\frac{d\Gamma}{d\phi} = \Gamma_1 cos^2\phi + \Gamma_2 sin^2\phi + \Gamma_3 sin\phi \cdot cos\phi \tag{3.36}$$

The coefficient Γ_1 is proportional to the internal bremsstrahlung amplitude (3.18) squared and Γ_2 is proportional to the M1 direct emission amplitude (3.19) squared, whereas the Γ_3 is proportional to the product of the two.

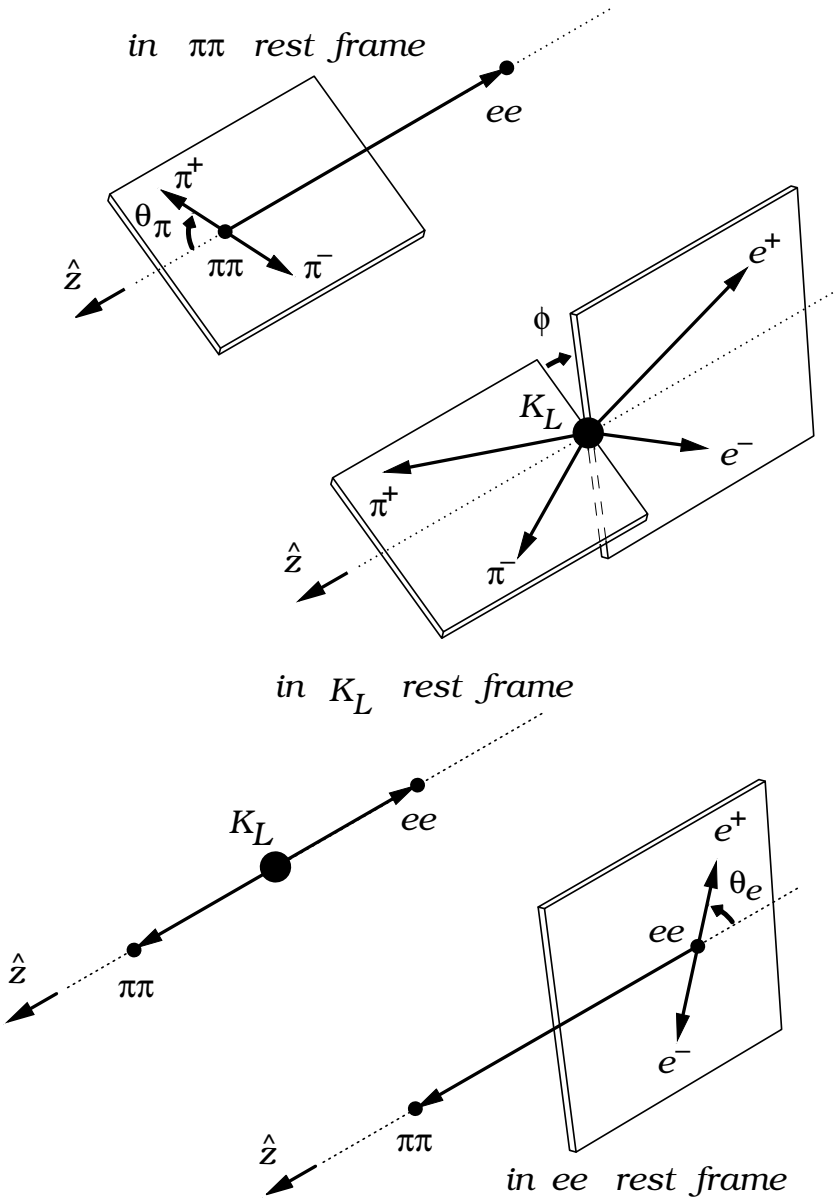

Figure 3.4: Definition of the angles ϕ, θ_e and θ_π used in the kinematic description of the decay $K_L \to \pi^+\pi^-e^+e^-$. The unit vector $\hat{z}$ points in the direction from '*ee*' to '$\pi\pi$', which denote centers of mass for the e^+e^- and $\pi^+\pi^-$ systems, correspondingly. Other vectors represent momenta of e^+, e^-, π^+, π^-, e^+e^- and $\pi^+\pi^-$ as shown.

3.3 The CP Violating Asymmetry

The CP-violating decay-plane asymmetry in the decay $K_L \to \pi^+\pi^- e^+ e^-$ is the result of the interference between the the CP-violating amplitude $\mathcal{M}_{IB}$ and CP-conserving amplitude $\mathcal{M}_{M1}$, equation (3.22). This CP violation ultimately originates in the decay $K_L \to \pi^+\pi^-$ where its strength is given by the parameter η_{+-} (2.8). The radiative decay $K_L \to \pi^+\pi^-\gamma$ has the information about this CP violation encrypted in the oblique polarization of the photon. The decay $K_L \to \pi^+\pi^- e^+ e^-$ serves as the analyzer of this polarization, where this oblique polarization of the photon in $K_L \to \pi^+\pi^-\gamma$ can be observed as an asymmetry in angular distribution $d\Gamma/d\phi$ (3.36), where ϕ is the angle between $\pi^+\pi^-$- and e^+e^--planes (figure 3.4).

In the case of $K_L \to \pi^+\pi^- e^+ e^-$, i.e. $K_L \to \pi^+\pi^-\gamma^* \to \pi^+\pi^- e^+ e^-$, the orientation of the e^+e^- plane will be determined by the polarization of the photon. In the Dalitz pair production $\gamma^* \to e^+e^-$ the electrons and positrons are predominantly emitted towards directions close to the photon polarization plane ($\vec{k}$, $\vec{\varepsilon}$), while the number of particles emitted in the direction perpendicular to the polarization plane will be much smaller. Therefore the e^+e^- plane acts as an analyzer of the photon polarization.

For the small energies of the photon in $K_L \to \pi^+\pi^-\gamma$, and for small M_{ee} in the decay $K_L \to \pi^+\pi^- e^+ e^-$, the bremsstrahlung (3.18) becomes the dominating contribution and the ϕ distributions (see equations (3.21) and (3.36) and comments after them about the energy dependence of the coefficients) correspondingly become

$$\begin{aligned} \frac{d\Gamma}{d\phi} &\sim 1 + B\cos^2\phi \\ \frac{d\Gamma}{d\phi} &\sim \Gamma_2 \cos^2\phi \,. \end{aligned} \tag{3.37}$$

In this case the polarization vector of the photon in $K_L \to \pi^+\pi^-\gamma$, and the normal to the e^+e^- plane in $K_L \to \pi^+\pi^- e^+e^-$, become perpendicular to the $\pi^+\pi^-$ plane. For the large photon energies in $K_L \to \pi^+\pi^-\gamma$, and large M_{ee} values in $K_L \to \pi^+\pi^- e^+e^-$, the ϕ distribution is dominated by pure $M1$ contribution

$$\begin{aligned} \frac{d\Gamma}{d\phi} &\sim 1 + A sin^2\phi \\ \frac{d\Gamma}{d\phi} &\sim \Gamma_1 sin^2\phi \end{aligned} \tag{3.38}$$

with the polarization vector of the photon in $K_L \to \pi^+\pi^-\gamma$, and the normal to the e^+e^- plane in $K_L \to \pi^+\pi^- e^+e^-$, approaching position parallel to the $\pi^+\pi^-$ plane.

In the intermediate region the interference between bremsstrahlung and $M1$ contribution causes the ϕ distribution to be of the form given by equations (3.21) and (3.36) with the angle between the polarization vector of the photon in $K_L \to \pi^+\pi^-\gamma$, and the normal to the e^+e^- plane in the decay $K_L \to \pi^+\pi^- e^+e^-$, to be oriented predominantly at approximately $\pi/4$ with respect to the $\pi^+\pi^-$ plane. The exact value of this angle, and therefore of the CP-violating asymmetry, is determined by the relative strength and relative phases in these contributions given in equations (3.16) and (3.17). Therefore it is crucial for the accurate measurement of the asymmetry to have the most accurate values for these parameters.

This decay-plane asymmetry is large, despite the fact that it is related to the small parameter ε (through η_{+-}). This effect represents a unique situation in which the CP violation effects of order 10^{-3} in the K_L wave function are magnified into a very large CP-odd, T-odd effect in the photon polarization transported into the decay $K_L \to \pi^+\pi^- e^+e^-$ as CP-violating asymmetry in the differential decay rate [36].

The asymmetry is defined as

$$\mathcal{A} = \frac{\int_0^{\pi/2} \frac{d\Gamma}{d\phi} + \int_{\pi}^{3\pi/2} \frac{d\Gamma}{d\phi} - \int_{\pi/2}^{\pi} \frac{d\Gamma}{d\phi} - \int_{3\pi/2}^{2\pi} \frac{d\Gamma}{d\phi}}{\int_0^{2\pi} \frac{d\Gamma}{d\phi}} \tag{3.39}$$

$$= \frac{\mathcal{N}_{sin\phi cos\phi > 0.0} - \mathcal{N}_{sin\phi cos\phi < 0.0}}{\mathcal{N}_{sin\phi cos\phi > 0.0} + \mathcal{N}_{sin\phi cos\phi < 0.0}} \tag{3.40}$$

where Γ is the differential decay rate (3.36), $\mathcal{N}$ is the number of e vents, ϕ is the angle between the e^+e^- and $\pi^+\pi^-$ planes in K_L rest frame (see figure 3.4).The quantity $sin\phi \cdot cos\phi$ can be calculated as follows

$$sin\phi \cdot cos\phi = \frac{1}{2} sin2\phi = (\hat{n_{ee}} \times \hat{n_{\pi\pi}}) \cdot \hat{z}\, (\hat{n_{ee}} \cdot \hat{n_{\pi\pi}}) \tag{3.41}$$

where the $\hat{n}$'s represent the unit normals to the e^+e^- and $\pi^+\pi^-$ planes and $\hat{z}$ is the direction of $\pi^+\pi^-$ system in the K_L rest frame, see figure 3.4.

Chapter 4

KTeV Experiment

KTeV[1] consists of two related experiments E832/E799-II in the Fermilab[2] fixed target program. The goal of E832 was to measure the direct CP violation parameter $Re\,(\varepsilon'/\varepsilon)$ using decays $K_{L,S} \to \pi\pi$. The goal of E799-II was the detection and measurement of many rare K_L decays. Both experiments used the same beamline and apparatus with minor changes in configuration to address the specific needs of each of them. The design, construction and operation of KTeV involved extensive research and state-of-the-art technology. Here the KTeV experiment is outlined mostly from the perspective of E799-II and even then, the focus is only on the components relevant to this analysis of $K_L \to \pi^+\pi^-e^+e^-$. There are many excellent documents describing the details of this unique apparatus. The details and references to the other sources related to both E799-II [38, 39, 40, 41] and E832 [42, 43, 44, 49] parts of the project can be found elsewhere.

KTeV collected data in 1996-1997 and then again in 1999-2000. These two separate runs are referred to as **'97** and **'99**, respectively. The detector and Tevatron were upgraded and operating conditions changed during the period between **'97** and **'99** runs. The differences between **'97** and **'99** will be explained as they arise in the context of this chapter.

[1]The name KTeV stands for "kaons at the Tevatron".
[2]The full name of the lab is Fermi National Accelerator Laboratory (FNAL).

KTeV was located in the NM (Neutrino Muon) beamline, where "KTeV Target Hall" and "KTeV Experimental Hall" were constructed, to take advantage of the new K_L beam. It had a typical structure for a fixed target experiment. The Tevatron accelerator provided a proton beam which struck the target in KTeV beamline area and produced a beam of neutral kaons. The K^0 flux then passed through a set of sweeping magnets and collimators and entered the KTeV detector which recorded information about the *kaon decays-in-flight*.

4.1 The Neutral Kaon Beam Production

KTeV used two side by side almost parallel neutral kaon beams. This feature was specifically designed for the purposes of E832 in order to measure K_L and K_S decays simultaneously. For E799-II both beams were identical and provided K_L's. In this discussion of the $K_L \rightarrow \pi^+\pi^-e^+e^-$ analysis the terms "beams", "KTeV beam" or simply the "beam" would be used interchangeably. The earlier set of Fermilab experiments with neutral kaons (E731, E773 and E799-I) provided valuable experience used to design the clean and well-collimated neutral beams.

The neutral beams were produced in the KTeV Target Hall (also called NM2 area), located upstream of the KTeV Experimental Hall. The Fermilab *Tevatron* provided the proton beam. The protons were accelerated by the $53\ MHz$ radio-frequency (RF) resonant cavities up to the energy of $800\ GeV$, which took $40\ s$. The beam was then extracted from the Tevatron and delivered to the target for a duration of $20\ s$ in '97 and $40\ s$ in '99 run, which resulted in $2 - 4 \times 10^{12}$ and $6 - 10 \times 10^{12}$ protons per spill in '97 and '99 .

Due to the $53\ MHz$ RF micro-structure, the protons arrived bunched in "buckets". The duration of each bucket was about $1 - 2\ ns$ and the interval between the buckets was $18.9\ ns$. This RF signal from Tevatron was used to synchronize the elements of the trigger with the bucket structure (section 4.3).

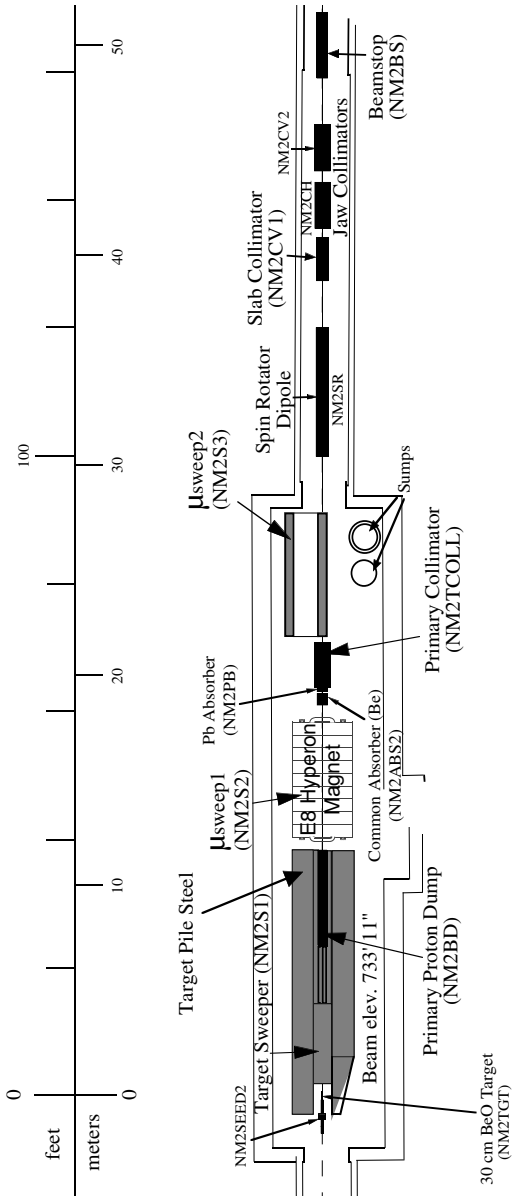

Figure 4.1: The KTeV beamline.

The neutral beam production target was a $\mathbf{30}\ \boldsymbol{cm}$ (about one proton interaction length) long *beryllium oxide* (BeO) rod with transverse dimensions $\mathbf{3} \times \mathbf{3}\ \boldsymbol{mm^2}$. The center of the target was chosen as the origin of the *right-handed* rectangular coordinate system used in the experiment. The z-axis was directed horizontally along the KTeV beam direction and the y-axis pointed vertically upwards. The proton beam was focused on the target to a spot size with RMS of $\mathbf{250}\ \boldsymbol{\mu m}$ in x and y directions. The position of the proton beam on the target was continuously monitored and adjusted using specially designed software called "Autotune" [50]. Both the proton beam and the target were tilted downwards by $\mathbf{4.8}\ \boldsymbol{mr}$ with respect to the z-axis to reduce the ratio of kaons to neutrons in the KTeV beams by moving away from the zero production angle.

The $\mathbf{90}^\circ$ *monitor* was located perpendicular to the beam about $\mathbf{2}\ \boldsymbol{m}$ away from the target. It consisted of three scintillator counters that viewed the target through a small hole in the shielding. The coincidence of the signal in all three counters produced a set of *accidental trigger* events. Such events were recorded and were later used in Monte Carlo simulation to model the accidental activity in the detector (chapter 6).

The residual proton beam was dumped into a block of copper (NM2BD) and the charged particles produced in the target were removed by a set of sweeping magnets NM2S1, NM2S2 and NM3S3 located downstream of the target (figure 4.1). Absorbers were used to reduce contamination to the neutral $\boldsymbol{K^0}$beam. A beryllium absorber was used to reduce the neutron and photon component of the beam, since neutrons have higher interaction cross-section than kaons. The remaining photons were removed by the lead absorber.

A system of collimators defined a square aperture for the two beams. The beams were shaped by the collimators so that they could pass through the square *beam holes* in the detector components to reduce the rate and radiation damage

from interactions with the beam. The beams entered KTeV decay region $93\ m$ downstream of the target with the average momentum of the kaons $70\ GeV/c$ and neutral kaon flux of about $2\ MHz$. The beam also contained about $6\ MHz$ flux of neutrons and small amounts of other particles which had not yet decayed at this distance from the target.

4.2 The KTeV Detector

The detector provided the measurement and identification of charged particles and photons necessary for the trigger decision (see section 4.3) and for the decay reconstruction (see section 5.1). The main components of the KTeV detector were decay region, magnetic spectrometer consisting of drift chambers and magnet, transition radiation detectors, electromagnetic calorimeter, and photon/muon veto system, see figures 4.2 and 4.3. Each component is described below from upstream to downstream along the beam.

4.2.1 The Decay Region

The decay region was the place in the detector where the kaons decayed. It was constructed from a telescopic array of 9 vacuum pipes connected by flanges and hermetically sealed by circular windows on both ends. The position of the decay region with respect to the neutral beam production target was chosen to allow most of K_S's to decay before they reached the decay region. It began at $z = 93\ m$ with the upstream most pipe of $18\ in$ in diameter and ended at $z = 159\ m$ with a pipe of $96\ in$ in diameter. This "telescopic structure" applies to the whole KTeV detector in the sense that cross section of detector components increased with the distance from the target. This was done to increase the geometric acceptance of the detector.

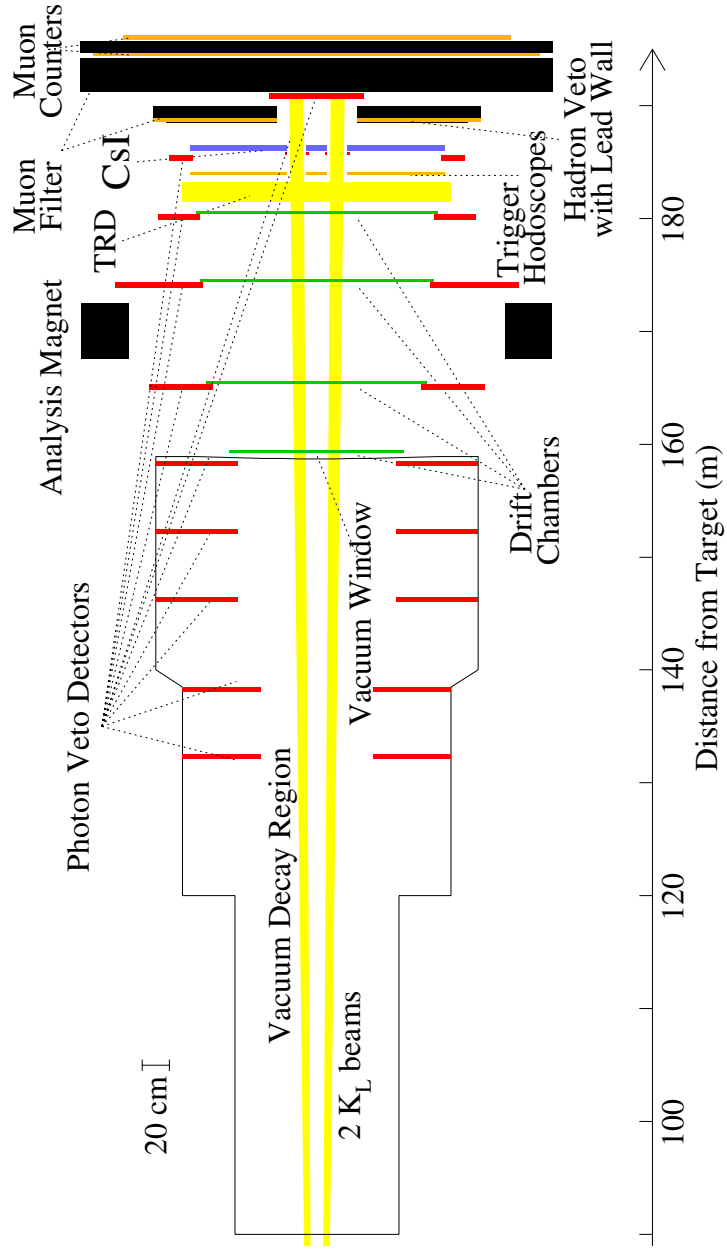

Figure 4.2: Schematic drawing of KTeV apparatus.

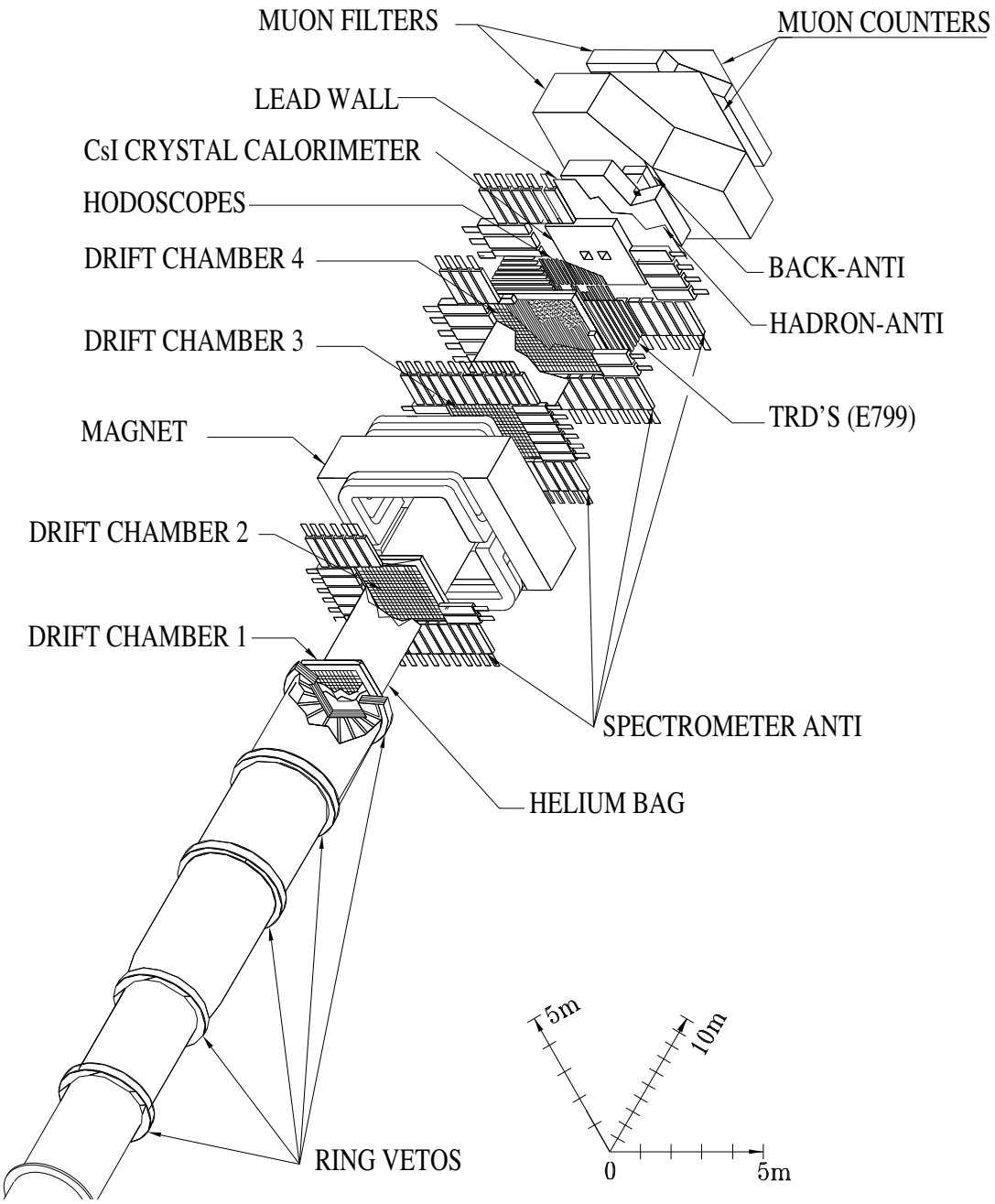

Figure 4.3: 3D drawing of the KTeV apparatus.

The vacuum inside the decay region was on the order of $10^{-6}\ torr$ to minimize the particle interactions with matter. The *vacuum window* at $z = 158.9\ m$ was made out of Kevlar laminated with Mylar ($0.14\ \%$ radiation length). Kevlar weave was used for mechanical strength and Mylar sheet provided a gas seal. This window was made thin to minimize the scattering of the decay products.

The two K_L beams entered the decay region and a fraction of K_L's decayed in flight into various final states. The decay products then left the decay region through the thin vacuum window and entered the magnetic spectrometer. The undecayed K_L's, along with other particles in the beam, continued through the beam holes in the detector components and were dumped at the end of the detector.

4.2.2 The Charged Particles Spectrometer

The function of the spectrometer was to trace the trajectories and measure the momentum of the charged particles. The spectrometer consisted of a dipole magnet and four planar drift chambers, see figure 4.3. The magnet had an aperture of $3 \times 2\ m^2$ and provided a $200\ MeV$ ($150\ MeV$) transverse *momentum kick* in '97 ('99) runs deflecting the charged particles in the horizontal plane (xz-plane). The momentum kick is the change in the x-component of the particle's momentum in the field of the analysis magnet. The magnet polarity was reversed every other day to minimize any possible left/right systematic effects. Two chambers were located upstream and two downstream of the analysis magnet to enable the position measurement before and after the magnetic deflection. The cross section of the chambers increased with distance from the target to increase the detector acceptance.

The *drift chambers* measured the x and y position of the charged particles with the resolution of about $100\ \mu m$. Each chamber consisted of a thick aluminum frame with mylar windows on each side. The wires were strung inside the the

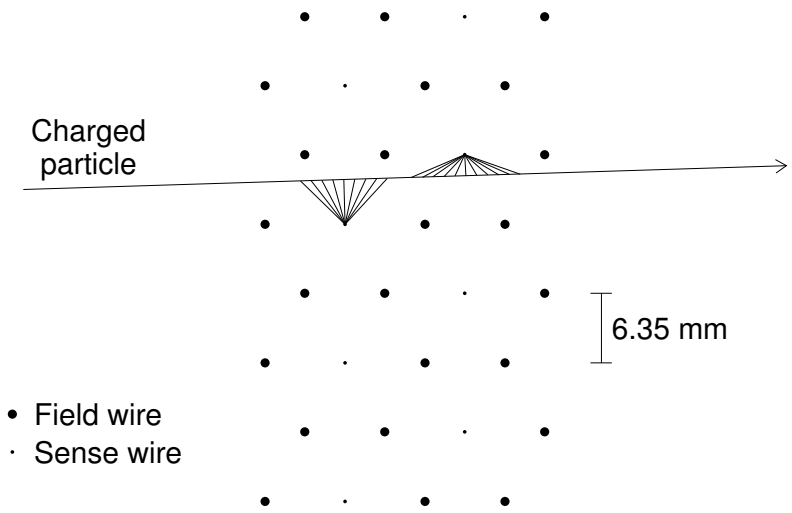

Figure 4.4: The cell of the drift chamber has hexagonal geometry. The ionization electrons drift from the traversing the cell charged particle to the sense wires.

frame in vertical and horizontal direction to measure the x and y positions, correspondingly. Both vertical and horizontal wires formed two adjacent "planes of wires". Each such plane consisted of $\mathbf{6.35}\ \boldsymbol{mm}$ wide *hexagonal cells* formed by cathode *field wires* ($\mathbf{4}\ \boldsymbol{mil}$ gold-plated aluminum) surrounding an anode *sense wire* ($\mathbf{1}\ \boldsymbol{mil}$ tungsten), see figure 4.4. The two planes within each vertical and horizontal pair were offset by half the cell spacing to resolve left/right ambiguity. A constant flow of gas was maintained through the chambers. The gas was $\mathbf{50/50}$ mixture of argon/ethane and $(\mathbf{0.5 - 1.0})\%$ alcohol to provide the optimal drift of ionization electrons. The high voltage was typically between $\mathbf{2450}$ and $\mathbf{2600}\ \boldsymbol{V}$.

Charged particles traversed the drift chambers and ionized the gas inside. The ionization electrons drifted to the closest anode sense wires and the readout from this wires registered a *hit*, i.e. the pulse in the analog signal. The electron *drift velocities* for the gas mixture and high voltage were typically about $\mathbf{50}\ \boldsymbol{\mu m/ns}$ with

the maximum *drift time* across the cell of $\mathbf{150}\ \boldsymbol{ns}$. The analog signals from the chambers passed through the amplifiers and discriminators and then were split between the trigger (section 4.3) and Lecroy 3373 time-to-digital converter modules (TDC's). The TDC counts were later used to obtain the drift times, which along with position of the hits on the wires were used to reconstruct the tracks of the charged particles (section 5.1.1). Downstream of the spectrometer particles traversed an array of transition radiation detectors (section 4.2.6) and $\boldsymbol{VV'}$ trigger hodoscope system before they entered the electromagnetic calorimeter.

4.2.3 The Trigger Hodoscope

The $\boldsymbol{VV'}$ *trigger hodoscope* was an essential part of the trigger (section 4.3). It was located just upstream of the calorimeter to provide fast information about the charged particles entering this detector. It consisted of two overlapping planes of scintillators arranged as shown on the figure 4.5. Each scintillator was wrapped in black paper and read out by a phototube.

4.2.4 The Calorimeter

The KTeV calorimeter [51] was an array of $\mathbf{868}$ *large* $\mathbf{0.05 \times 0.05 \times 0.5}\ \boldsymbol{m^3}$ and $\mathbf{2232}$ *small* $\mathbf{0.025 \times 0.025 \times 0.5}\ \boldsymbol{m^3}$ crystals of pure *cesium iodide* (CsI), see figure 4.6. Fifty centimeters of CsI corresponds to 27 radiation lengths which allows containment of almost complete longitudinal shower development from the high energy electrons and photons, but is relatively transparent to hadrons.

The CsI blocks were individually wrapped with reflective and black paper. The scintillation light in each crystal was viewed by Hamamatsu photomultiplier tubes R5364 and R5330 for small and large blocks, respectively. The analog signal output of these tubes was then digitized by individual ADC's mounted on the phototube bases with an optical cookie. These ADC's were specifically designed for KTeV

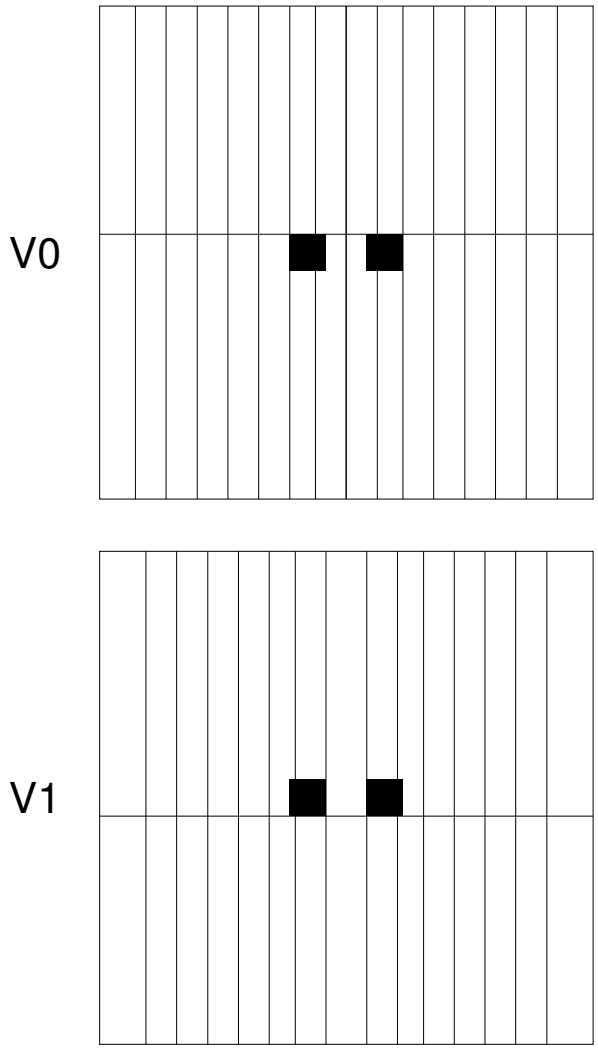

Figure 4.5: The arrangement of trigger hodoscope scintillators. The planes are $\mathbf{95}\ \boldsymbol{cm}$ squares and the beam holes in the middle are $\mathbf{14}\ \boldsymbol{cm}$ squares. The plane $\boldsymbol{V}$ was located upstream of the plane $\boldsymbol{V'}$.

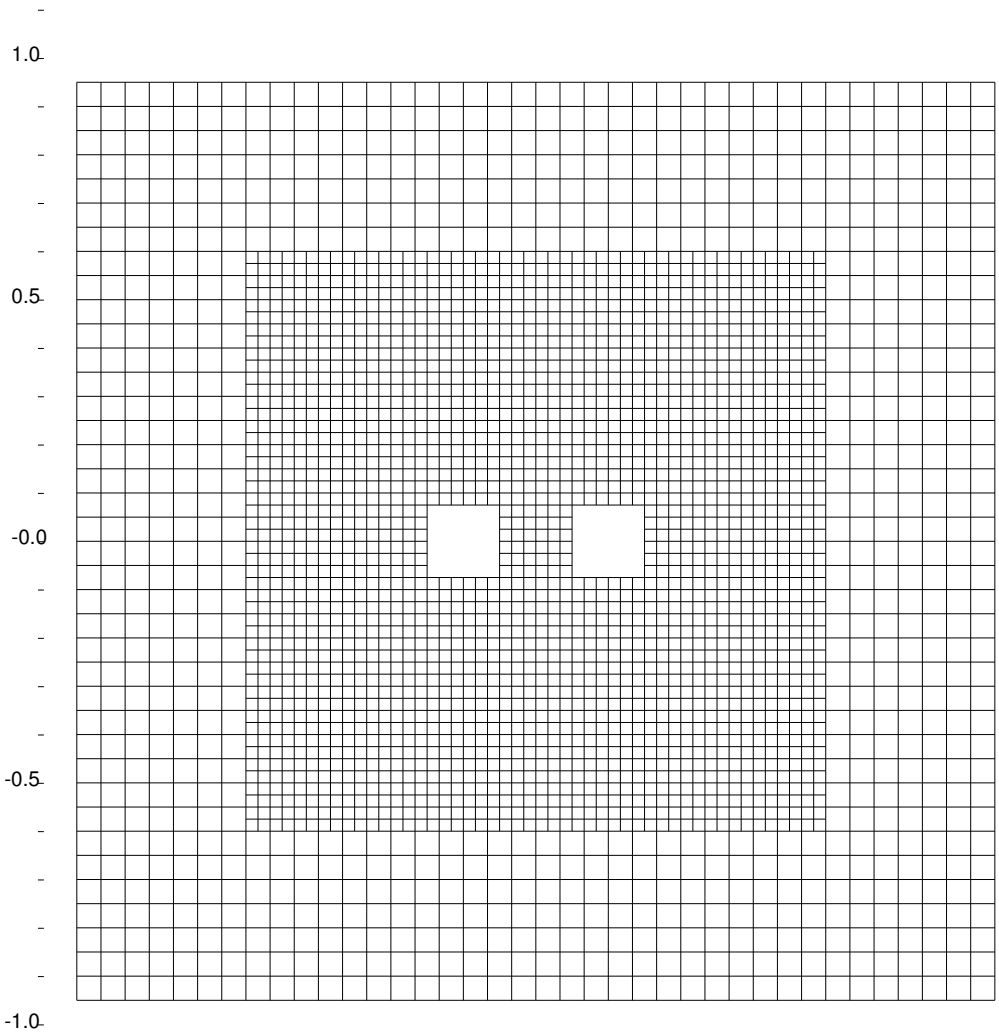

Figure 4.6: The arrangement of 3100 CsI blocks in the calorimeter. The transverse size of the array is $\mathbf{1.9}\ \boldsymbol{m}$ square and the two beam holes in the middle are $\mathbf{0.15}\ \boldsymbol{m}$ squares located $\mathbf{0.3}\ \boldsymbol{m}$ apart (center to center). Each block is $\mathbf{0.5}\ \boldsymbol{m}$ deep.

[52] and the entire readout system was called *digital photomultiplier* (DPMT). This readout technique minimized electronic noise and to allowed to measure energies from few MeV to $100\ GeV$. The digital signal from the DPMTs was converted to the measurement of energy. The response from each DPMT was first aligned by measuring the response to a laser pulse monitored by a PIN diode with an ADC readout. Then the electrons from K_{e3} decays with momentum measured in the analysis magnet were used to calibrate the detector energy by tuning the energy/momentum ratio $\frac{E}{P}$ to be one.

The calorimeter measured the position and energy of electrons and photons with the position resolution of approximately $1\ mm$ for small blocks and $2\ mm$ for large blocks and an average energy resolution under 1% in the energy range up to $200\ GeV$.

4.2.5 The Photon Veto System

The photon veto system consisted of multiple ring and square counters which were inserted along the length of the detector, see figures 4.2 and 4.3. This veto system was the essential part of the trigger and defined sharp apertures and edges that define the transverse detector acceptance.

The system included five *ring veto counters* (RC's) along the decay region (the last counter RC10 is framing first drift chamber); four *spectrometer anti* (SA's) counters framing the three downstream drift chambers and the calorimeter; two collar anti (CA) rectangular "picture-frames" around the calorimeter beam holes; and *beam-hole anti* (BA) detector located behind the CsI calorimeter. See section 4.2.6 for the description of the BA and the muon and hadron veto detectors.

The transverse layout of RC's and SA's was similar, except that both inner and outer perimeters of SA's were rectangular and the RC's had square apertures and the outer perimeters were circular. The apertures and the outer perimeters of

the counters increased with the distance from the target. Figure 4.7 shows the aperture coverage of RC7 and CA veto detectors.

The SA and RC counters were built with multilayered lead/scintillator sandwiched modules. Different photomultiplier tube read out each module. The CA consisted of layers of tungsten and scintillator. The analog signals from the detectors of the veto system were recorded by 10-bit LRS 4300 analog-to-digital converter modules (ADC's). The signals were also split out and sent through discriminators to the trigger.

4.2.6 The Muon System and Other Components

The remaining components of the KTeV detector, shown on the figures 4.2 and 4.3, were *helium bags*, *transition radiation detectors*, *hadron anti*, *beam-hole anti*, and the *muon identification* system.

The muon system consisted of the filter and the counters. The $\mathbf{3}\ \boldsymbol{m}$ steel wall was followed by rectangular bank of scintillators (MU2). One more meter of steel wall was placed in front of the two rectangular banks of scintillators arranged in $\boldsymbol{x}$- and $\boldsymbol{y}$-directions (MU3). The signals from MU2 were used in the trigger for $\boldsymbol{K_L \to \pi^+\pi^- e^+ e^-}$ decays to veto events with muons.

A set of eight transition radiation detectors (TRD's) was located between the spectrometer and the trigger hodoscopes. Each detector contained radiator (polypropylene felt mats with beam holes in the center) and a multi-wire proportional chamber. The purpose of these detectors was discrimination between pions and electrons. In this analysis however the energy and momentum of a particle measured in calorimeter and spectrometer were sufficient to distinguish out pions from electrons (section 6.4). *The transition radiation detectors were not therefore used*.

Large helium bags, see figure 4.3, were installed between the drift chambers of the spectrometer to minimize the multiple scattering of the decay products,

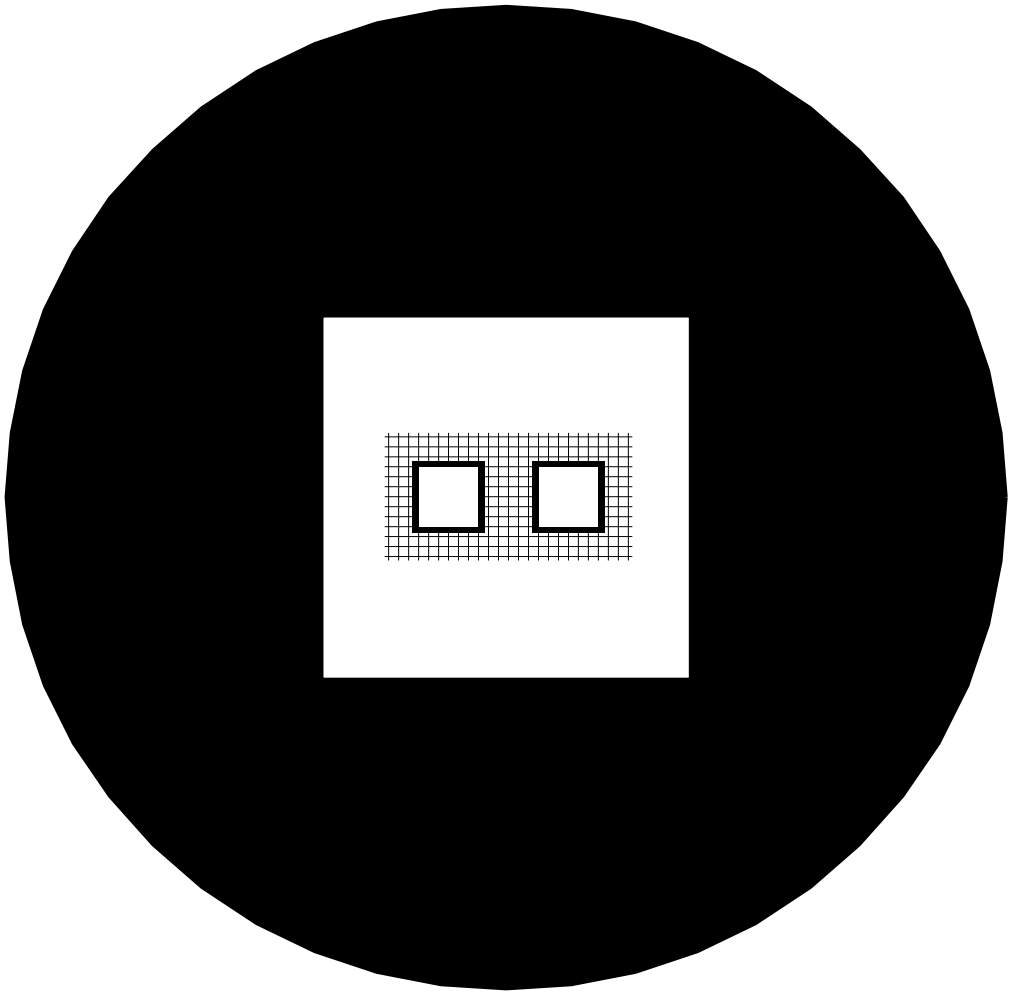

Figure 4.7: The veto aperture defining the transverse geometrical acceptance of the KTeV detector. The neutral beams are into the page in this plot and the two beam-hole centers are separated by $\mathbf{0.3}\ \boldsymbol{m}$. The aperture coverage of the veto detectors are shown as solid *black areas*. All five photon ring veto counters (RC's) (see figures 4.2 and 4.3) had the same transverse layout with the square aperture about 1 meter (it increased with the RC number). Ring veto RC7 defined the detector aperture and the collar anti (CA) framed the beam holes in the CsI calorimeter. The *grid* represents the crystals in the central region of the calorimeter, see figure 4.6. The rest of the calorimeter crystals, the wires of the drift chambers and the beam-hole vetoes are not shown (*white space*).

The neutral kaon beam passed through the holes in the CsI calorimeter into the veto detector, called the *back anti* or BA, installed in the beam region downstream of the calorimeter, and finally were absorbed in the steel wall of the muon filter (figure 4.2). Most particles were absorbed there except for muons and neutrinos.

4.3 The 4-track Trigger

The function of the trigger was to process the information from the detector and to provide the decision for the data acquisition system about either to write the information from the detector elements to tape or not. Only one out of about 10^5 protons, contained in one Tevatron bucket, hitting the target produced a kaon which was able to reach the decay volume. Only a few percents of these kaons decay and only three out of about 10^7 decays were be $K_L \rightarrow \pi^+\pi^-e^+e^-$! The trigger was designed to reject most of the uninteresting events occurring in the detector, while being as efficient as possible in selecting decays of interest. Only the trigger used to select the $K_L \rightarrow \pi^+\pi^-e^+e^-$ decays is explained here. The complete KTeV trigger system was described elsewhere, e.g. see chapter 3 in [38].

The KTeV trigger had three levels and it's timing was synchronized to the the proton beam pulses delivered by Tevatron, see section 4.1. During the beam extraction (SPILL) the Tevatron dumped to KTeV a $1-2\ ns$ long "bucket of protons" every $19\ ns$, i.e. at the rate of $53\ MHz$. Therefore the *level 1* trigger (L1) decision had to be accomplished every $19\ ns$, using the fastest analog signals from the detector in order to introduce no dead-time. The digitization of the signals from the drift chambers and calorimeter began only if L1 decided to accept an event. If L1 accepted the event, the *level 2* trigger (L2) system, based on more sophisticated processors which analyzed the digital signals from these detector elements, acted on the event. If L2 accepted the event, the entire detector was read out and the information was sent to the *level 3* (L3) trigger software, which ran in parallel on

24 independent 200-MHz processors, performing a quick reconstruction of decays and applying loose kinematic requirements.

The *4-track* trigger was one of sixteen beam triggers available in E799 configuration (KTeV beam trigger # 4), but for the purposes of the analysis presented in this thesis it would sometimes simply referred to as the *trigger*. This trigger was specifically designed to search for the $K_L \to \pi^+\pi^- e^+ e^-$ decay. The definition of the trigger can be written as follows:

$$\begin{aligned} \texttt{4TRK} \quad = \quad & \texttt{GATE} * \texttt{3V\_TIGHT} * \texttt{2DC12\_MED} * \texttt{ET\_THR1} * \texttt{!MU2} * \texttt{PHVBAR1} \\ & * \texttt{!CA} * \texttt{34\_HCY} * \texttt{3HC2X} * \texttt{YTF\_UDO} * \texttt{HCC\_GE2} \end{aligned} \tag{4.1}$$

where all the symbols represent the elements of the trigger and their meanings are summarized in the table 4.3. In the following sections each element of the trigger is explained in more detail.

4.3.1 Level 1 Requirements

At level 1 the 4-track trigger vetoed events with particles leaving fiducial volume of the detector and events with muons which pass 4 meters of steel, while requiring that there were enough hits in the drift chambers and trigger hodoscopes and the total energy deposited in the calorimeter was more than minimum kaon energy. The L1 elements were as follows:

`GATE` This trigger element was set if the proton beam (see section 4.1) was being delivered to KTeV target.

`3V_TIGHT` At least 3 scintillators were hit in V bank and 3 scintillators were hit in V′ bank of the trigger hodoscopes, see section 4.2.3.

`2DC12_MED` The sense wires in both x- and y-views of the drift chambers DC1 and DC2 (see section 4.2.2) were grouped in the “paddles”. The paddle

Trigger Element	**Trigger Level**	**Description**
GATE	1	Was used in '97 to veto the "fast spill" to the neutrino center. In '99 this element was simply equivalent the SPILL signal.
3V_TIGHT	1	Require at least 3 hits in V bank and 3 hits in V′ bank.
2DC12_MED	1	Have at least 2 paddles hit in 3 views out of 4 DC OR views. The remaining 4th view must have at least 1 paddle hit.
ET_THR1	1	Require that total energy deposit in the calorimeter is at least $\mathbf{11}\ \boldsymbol{GeV}$
!MU2	1	Veto events with at least 1 hit (15 mV, 0.2 MIP) in MU2
PHVBAR1	1	Veto events with at least 500 MeV of energy deposited in RC's or events with at least 400 MeV in the SA's
!CA	1	Veto events with at least 14 GeV of energy deposited in the Collar-Anti
34_HCY	2	Require at least 3 hits in 4 Y-view planes of DC1 and DC2 and 4 hits in in 4 Y-view planes of DC3 and DC4.
3HC2X	2	DC2 Hit Counting in X-view: require at least 3 hits in X-view of DC2 or that counting is not complete yet.
YTF_UDO	2	Y Track Finder (YTF): require one good track in the upper half and one good track in lower half or one good central track, or that counting is not complete yet.
HCC_GE2	2	Require at least 2 hardware clusters or that counting is not complete yet.

Table 4.1: The E799 4-TRACK Trigger Elements

spanned 16 wires (8 wires in each of the adjacent planes) of the chamber view and was $\mathbf{10.2}\ \boldsymbol{cm}$ wide. This trigger element required that at least two such paddles were hit in three out four available views. The fourth view had to had at least one paddle hit.

`ET_THR1` The analog signals from all the 3100 calorimeter photomultipliers (see section 4.2.4) were summed. This analog sum was used to approximately determine the energy deposited in the entire CsI calorimeter. This trigger element required that the total energy was higher than the threshold of $\mathbf{11}\ \boldsymbol{GeV}$, corresponding to the minimum kaon energy.

`!MU2` Required that there were no hits in the MU2 counters from the muon system, see section 4.2.6.

`PHBAR1` The energy in any of RC counters was less than $\mathbf{500}\ \boldsymbol{MeV}$ and the SA's had less than $\mathbf{400}\ \boldsymbol{MeV}$, see section 4.2.5.

`!CA` The collar anti had no counter with the energy above $\mathbf{14}\ \boldsymbol{MeV}$, see section 4.2.5 and figure 4.7.

4.3.2 Level 2 Requirements

At level 2 the event was accepted only if information from the drift chambers and calorimeter was consistent with the possibility of at least three particles in the final state, two of which could be electrons or positrons. The L2 elements were as follows:

`34_HCY` The signals from the drift chambers were analyzed by the sophisticated *hit-counting system* based on custom built hardware processors (see section 3.4 in [40] for detailed discussion of the system). The system verified

hit timing information and counted the number of hit wire pairs in complimentary views of the drift chambers. This trigger element was based on the result provided by the hit counting system. It required that at least three hits in four y-views of the drift chambers DC1 and DC2 and at least four hits in all four y-views of chambers DC3 and DC4.

`3HC2X` This trigger element also used the hit-counting system and required that at least three hits were found in x-view of chamber DC2 or that the system had not completed the counting yet.

`YTF_UD0` Another L2 processor, called the *y-track finder* (YTF), used the information from the hit-counting system to search for one track in both the upper and the lower halves of the drift chambers. It required one good track in the upper and one good track in the lower half or one good central track or that the hit-counting system had not finished counting yet.

`HCC_GE2` A special *hardware cluster counter* (HCC) counted the number of energy "clusters" in the calorimeter using the information from the CsI photomultipliers, see section 4.2.4. The clusters, defined in section 5.1, were based on the energy deposited in the calorimeter. The HCC counted number of hardware clusters, i.e. clusters containing at least $\mathbf{1}\ \boldsymbol{GeV}$ of energy. This trigger element required that at least two hardware clusters were found.

4.3.3 Level 3 Requirements

At level 3 the software required three tracks coming from a common vertex. The positions and energies of the decay products were reconstructed according to the techniques described in the section 5.1.2. All good L3 triggers from the entire spill (see section 4.1) had all event information from the detector buffered into the memory. The L3 trigger had $\mathbf{60}\ \boldsymbol{sec}$ in $\boldsymbol{'97}$ and $\mathbf{80}\ \boldsymbol{sec}$ in $\boldsymbol{'99}$ to analyze

the L2 accepted events without introducing any dead-time. In order to meet this processing time constraint, the L3 software was simplified compared to the off-line analysis programs described in chapter 5.

4.4 The Data Collection

During the data taking all events satisfying any of the KTeV E799-II sixteen beam triggers were written on-line to the Digital Linear Tapes (DLT's) in the round-robin fashion. After the data was collected, the events satisfying only the 4-track trigger were selected off-line and spooled to separate set of DLT tapes. Each output tape could contain data from several runs. On the other hand some long runs could be split between several tapes. The output events contained the CsI and HCC information in the squeezed format, and all other data in the raw format. There were about 140 million events and about 260 million events written to tape in $'97$ and in $'99$, respectively. This data set contained the $K_L \to \pi^+\pi^-e^+e^-$ decays used in this analysis.

Chapter 5

Data Selection

The data used in this analysis was accumulated during the 1997 and 1999 running periods, when KTeV was operating in E799 mode. All events that satisfied the on-line 4-track trigger requirements were selected off-line from the raw data tapes and stored on separate Digital Linear Tapes (DLT). These events were then processed by an offline program which performed reconstruction of decays from the digitized information written during the on-line data taking. This program also performed initial data reduction and the reduced output was written to another set of DLT tapes. These were processed by a final analysis program to select the final $K_L \rightarrow \pi^+\pi^-e^+e^-$data sample and a normalization sample of $K_L \rightarrow \pi^+\pi^-\pi^0_D$ decays. In the following sections each step is described in more detail.

5.1 Reconstruction of Decay Products

All the final state particles in the decay $K_L \rightarrow \pi^+\pi^-e^+e^-$ are charged and, therefore, the trajectories for each particle can be reconstructed from the hits left in the drift chambers and from the position of the cluster of energy deposited in the calorimeter. The TDC counts stored for each event during the data acquisition provided all necessary information from the drift chambers. The calorimeter

information was available in terms of the ADC counts from the digital photomultiplier tubes. This section explains how the detector readout information was used to reconstruct the trajectories, momenta and energies of the decay products along with their identification and the position of the decay vertex. The software used for this purpose is contained in the KTEVANA package (v5_06) written by and for the members of KTeV collaboration. Only the main ideas relevant to the reconstraction $K_L \to \pi^+\pi^-e^+e^-$ and $K_L \to \pi^+\pi^-\pi^0_D$ decays are outlined here; the detailed description of the algorithms in that package can be found elsewhere, e.g. see chapter 6 in [42], chapter 6 in [38], chapter 4 in [46] and chapter 5 in [47], and references wherein.

5.1.1 The Tracks In The Spectrometer

The TDC counts read out from the drift chambers during the data taking were used to obtain the drift times for each possible chamber hit. These drift times were then converted to the *drift distances* using the maps obtained using K_{e3} data and special muon calibration runs (see section 5.3 in [43] for the discussion of how such maps were obtained). To have an unambiguous position in the chamber an in-time pair of hits was required in the adjacent planes for both x- and y- views. Figure 4.4 shows one such *hit pair*. The sum of drift distances for each pair was required to be equal to the cell spacing $6.35\ mm$ within $1\ mm$ tolerance. The combinations of the hit pairs then were searched to obtain possible tracks in xz- and yz-planes separately.

The tracks in the yz-planes were obtained by fitting the combinations of hits in chambers two and three to a straight line connecting hit pairs in chambers one and four. If the fit χ^2 for straight line was acceptable, then the track was considered to be a candidate. All available hit pairs were searched for possible tracks in this way. If no track candidates were found the event was rejected.

The tracks in xz-plane were bent in the magnet and the bending angle was reconstructed from the track segments upstream and downstream of the the magnet. The upstream segments were obtained from chambers one and two and the downstream tracks from chambers three and four. All possible track segments which matched within $6\ mm$ at the center of the magnet were combined to make a complete track. If less than two complete tracks were found then the the event was rejected.

The information from the drift chambers along was not enough to reconstruct the complete particle trajectories in three dimensions. After the track candidates in xz- and yz-planes were found, the position of clusters of energy deposited in calorimeter was used to match these x- and y-track projections. The matching technique is explained in section 5.1.3.

5.1.2 The Energy In The Calorimeter

The electro-magnetically interacting particles leave most of their energy in the CsI crystals of the calorimeter. The electromagnetic showers in this medium produce scintillating light with the intensity proportional to the energy of the incoming particle. This light is converted to electric charge and then to ADC counts by the digital photomultiplier tube (section 4.2.4). During the reconstruction process, the deposited energy for each crystal block in the calorimeter was obtained from the digital photomultiplier ADC values by using conversion coefficients derived from K_{e3} electron data.

The blocks with maximum energy deposit of more than $0.1\ GeV$ were designated as *seed blocks*. Around each seed block an array of crystals was formed to represent the energy cluster. The size of these arrays was 7×7 for small blocks and 3×3 for large blocks. The *raw cluster energy* was calculated by summing the energies of all the blocks in the array.

The *cluster position*, in the xy-plane of the face of the calorimeter, was determined using the ratios of the energy in the seed block to the energies in the adjacent blocks. The position resolution was better than $1\ mm$ for small blocks and better than $2\ mm$ for large blocks (see section 4.5.1 in [44]).

The raw cluster energy was adjusted by multiple corrections to account for the calorimeter geometry and a number of other second order effects. The corrections applied in this analysis included the missing block correction, the threshold correction and the sneaky-energy correction. The *missing block* correction was applied to the clusters located near the beam holes or the edges of the CsI calorimeter (see figure 4.6). Some blocks could be missing in the 7×7 and 3×3 crystal arrays of these marginal clusters. This would result in the underestimation of the energy measurement. The transverse shower profiles simulated with GEANT were used to correct the energy in such clusters with missing blocks. The *sneaky-energy* correction was applied to the clusters located close to the beam holes. Parts of the electro-magnetic shower could span the hole and would end up in the crystals on both sides of a beam hole. The sneaky-energy correction took into account this effect. required This correction was based on the measurement of clusters from the electrons in the K_{e3} decays from data. The *threshold* correction compensated for another underestimation of energy, which resulted from the sparsification of the readout from the digital photomultipliers. The detailed discussion of the energy corrections can be found in the section 4.2.4 of [45].

5.1.3 The Charge Particle Trajectories

The particle trajectories and decay vertex for each potential decay were reconstructed based on the track candidates in separate views and the position of the energy clusters. The *matching* of the tracks to the positions of the clusters of energy in the calorimeter was used to form the three dimensional trajectories from

the separate track candidates in x- and y-views. The *vertexing* algorithm used iterative procedure to determine the vertex z-position using the upstream intercepts of these three dimensional trajectories.

To reconstruct the trajectories, the y-tracks and the downstream segments of the x-tracks were projected to the calorimeter and matched to the clusters. If a cluster was found to be within $\mathbf{7}\ cm$ from the intercepts in each view then these x- and y- track candidates were matched to each other to form the three-dimensional trajectory based on the position of the cluster. This cluster was then associated with this 3D-trajectory and was not used to search for photon clusters.

To find the position of the vertex, the y-tracks were combined with the the upstream segments of the x-tracks. The possible z-positions of the vertex were determined by fitting the intersections of y-tracks to the intersections of x-tracks and matching the upstream and downstream segments of the x-tracks in the magnet. If possible *vertex candidates* (i.e. a combination of reconstructed three-dimensional trajectories consistent with four particles coming out of a common vertex within the decay volume) were found, then a set of *final corrections* to the drift chamber hits was applied to account for: the time required for the *signal propagation* from the wires to the readout electronics modules, the *rotations* of the chambers around the z-axis, the *angle* between the track and the chamber plane, etc (see section 4.4.2 in [46] for details). The tracks were then re-fit based on the corrected hits from the drift chambers and used to fit for the *vertex z-position* and to obtain the corrected three-dimensional trajectories. After that two χ^2-values were calculated for each corrected vertex candidate: one at the vertex and one at the magnet z-positions. The *vertex* χ^2 was calculated using the sum of these two χ^2-values weighted by the errors due to the resolution in the drift chambers and the effects of the multiple scattering. A vertex candidate with the smallest χ^2-values

and with the best quality of the drift chamber hits was chosen as the final decay vertex.

5.1.4 The Momentum and Particle Identification

The *momentum* $\boldsymbol{P}$ *for each particle* was calculated based on the bending of the particle's trajectory in the magnet. The direction of the particle deflection and the polarity of the magnetic field were used to obtain the *sign* of electric charge of the particles. To distinguish electrons and positrons from the pions, i.e. to perform *particle ID*, the energy $\boldsymbol{E}$ measured in the calorimeter was compared to the momentum of the track matched to the corresponding cluster. The electrons and positrons deposited almost all of their energy in the calorimeter, whereas hadronically interacting pions would deposit only a fraction of their energy (section 4.2.4). Since all particles are moving nearly at the speed of light, the *ratio* $\frac{\boldsymbol{E}}{\boldsymbol{P}}$ would be close to unity for electrons and positrons, and less than one for pions.

In this analysis, the energy measured in the calorimeter was used *only* for the particle identification. After each particle in the final state was identified it was assigned the appropriate mass value ($\boldsymbol{M_e}$ or $\boldsymbol{M_\pi}$). The momentum and the mass of the particles provided all the necessary information to calculate any kinematic quantity, including the energies of each particle, for a particular decay. A number of such quantities will be used in the next sections to select the clean statistical samples of the decays $\boldsymbol{K_L \to \pi^+\pi^- e^+ e^-}$ and $\boldsymbol{K_L \to \pi^+\pi^-\pi^0_D}$.

5.2 Initial Data Reduction

The 4-track trigger data set (see section 4.4) was analyzed to reconstruct the decay products and to perform the initial data reduction. Although different programs were used to accomplish this task for the **'97** and **'99** data, the differences were only in the version (v4_12 for **'97** and v5_03 for **'99**) of the KTEVANA software

package used and the detector calibration constants. The data reduction steps were the same for both the running periods. The initial selection process filtered the 4-track triggers into *two data subsets*. All the requirements for the reduced subsets are described in this section. The same event was allowed to belong to both subsets if it satisfied the requirements for both.

The subset 4TRKPT containing the $K_L \rightarrow \pi^+\pi^-e^+e^-$ candidates had the requirements summarized in the following logical expression:

$$\texttt{4TRKPT} = \texttt{T3TRAK} * \texttt{KTCLUS} * \texttt{COMBIN} * \texttt{T3FVTX4} * \texttt{PT2ONE} \quad (5.1)$$

The candidates for the $K_L \rightarrow \pi^+\pi^-\pi^0_D$ subset (4TRKGPT) had requirements:

$$\texttt{4TRKGPT} = \texttt{T3TRAK} * \texttt{KTCLUS} * \texttt{COMBIN} * \texttt{T3FVTX4} * \texttt{PT2TWO} \quad (5.2)$$

These symbols for the selection criteria are explained below.

T3TRAK The x- and y-tracks were reconstructed according to the *tracking* procedure described in the section 5.1.1. This step was considered successful if at least two x-tracks and one y-track were found, thus allowing for the possibility of two x-tracks in the xz-plane. The distributions of the number of x- and y-track candidates (NXTRK and NYTRK, correspondingly) are shown at the top of the figure 5.1.

KTCLUS The energy clusters were reconstructed as explained in section 5.1.2. This *clustering* procedure was successful if no problems occurred during the cluster reconstruction. The events were rejected if no clusters could be found. The distribution of the number of found clusters (NCLUS) is shown at the bottom of the figure 5.1.

COMBIN The product COMBIN = NXTRK * NYTRK * NCLUS was calculated at this stage. In order to save processing time, if this product was greater than 30,000 (see figure 5.2) the further processing was not done.

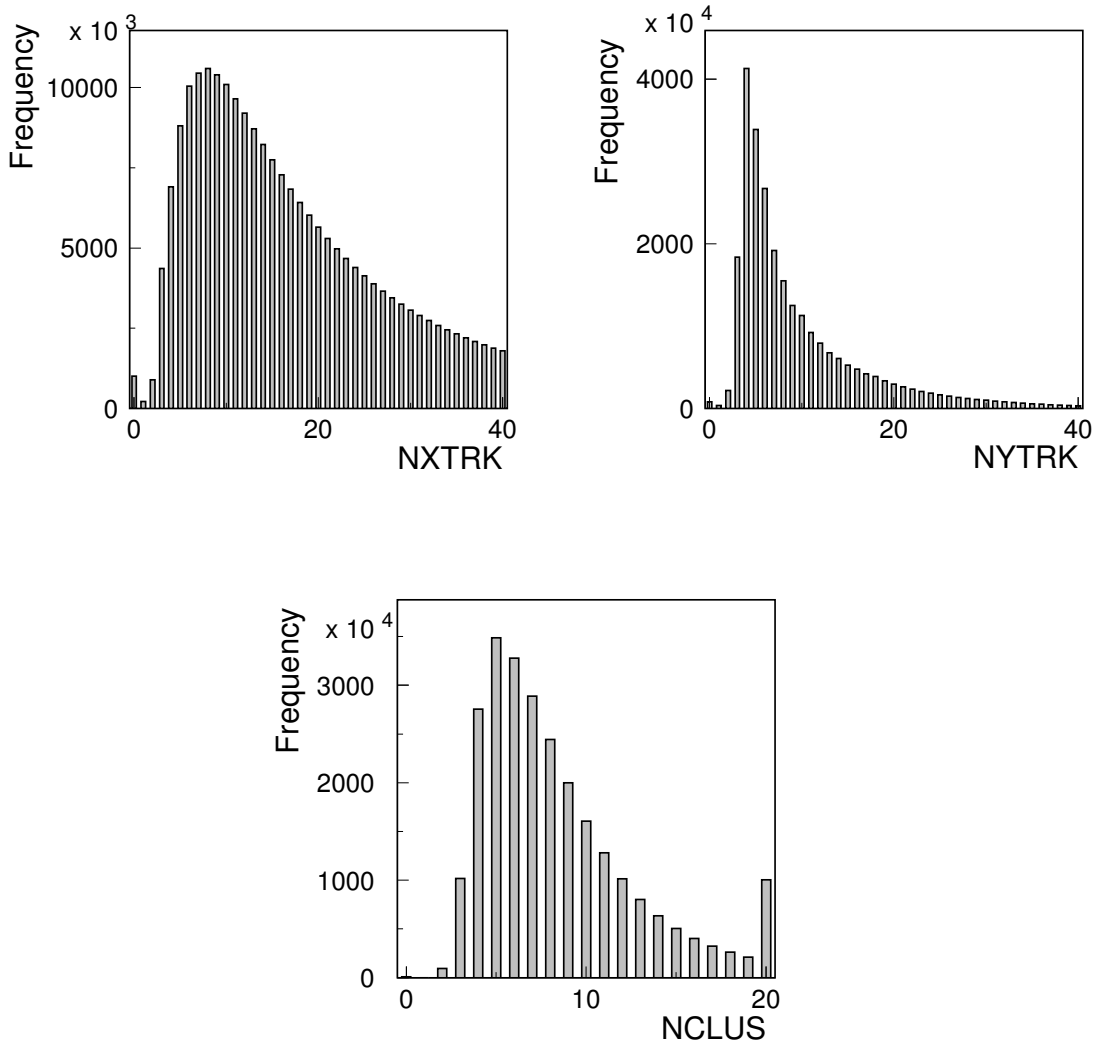

Figure 5.1: The distributions of the number of x- and y-tracks found by the tracking algorithm described in the section 5.1.1 (top); and the distribution of the number of clusters in the calorimeter found by the clustering algorithm described in section 5.1.2 (bottom). The first two distributions are plotted after the `T3TRAK` and the third after `KTCLUS` stages, respectively.

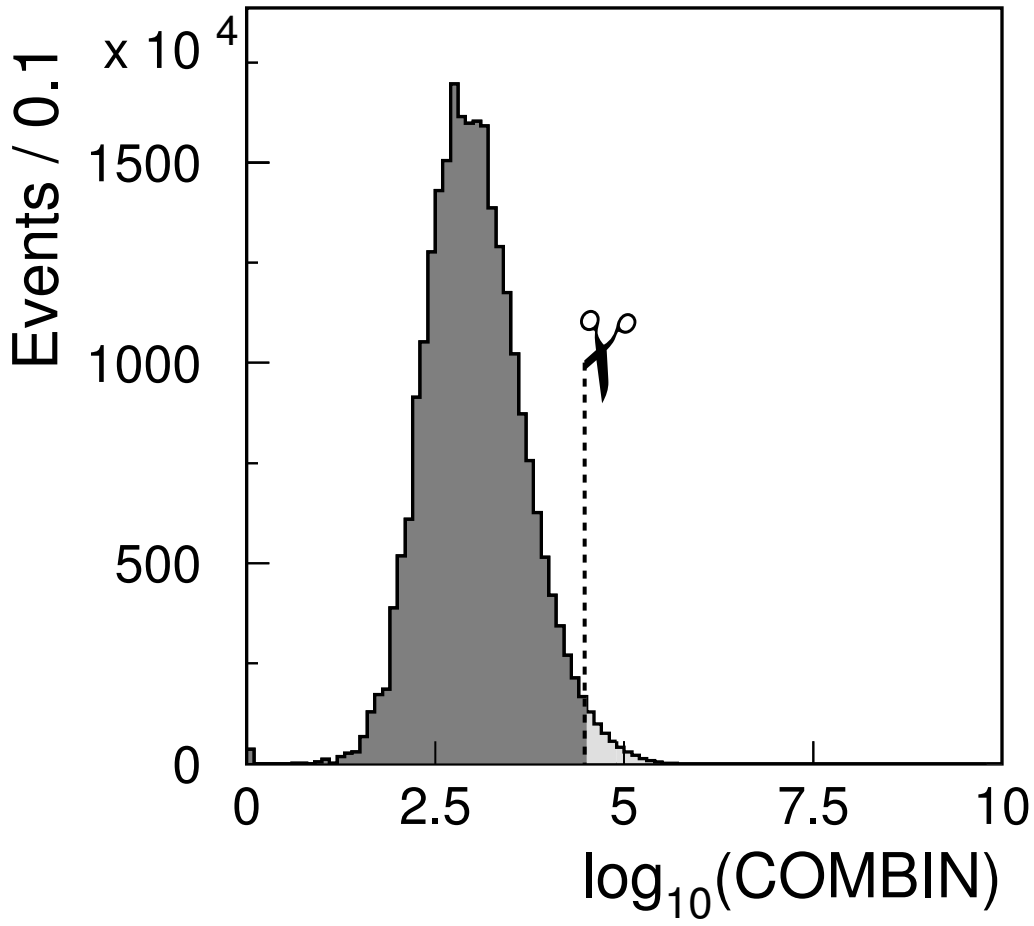

Figure 5.2: The distribution of the quantity log_{10} (COMBIN) (see section 5.2) for events from 4-track trigger data set. The distribution is plotted after the KTCLUS stage. The dashed line represents the cut value, i.e. the events are kept if COMBIN $< 30,000$ ($log_{10}(30,000) \approx 4.477$).

`T3FVTX4` The search for the 4-track vertex was done according to the *vertexing* procedure outlined in section 5.1.3. One out of four tracks was allowed to have no associated cluster and could point down the beam hole or outside of the calorimeter. This stage considered to be successful if a vertex was found. Effectively, this requirement *constrained the number of tracks to be at least four*, since a 4-track vertex was required. The distribution of the number of tracks for the event where the vertex was found is shown in figure 5.3.

`PT2ONE` At this point, the kinematic quantity $\boldsymbol{P_t^2}$, the component of the total momentum of the decay products *transverse to the line of flight of the kaon* (see figure 5.4), was calculated. To select the possible candidates for the $\boldsymbol{K_L \rightarrow \pi^+\pi^-e^+e^-}$ decay, it was required that $\boldsymbol{P_t^2 < 0.0004\ GeV/c^2}$, where the $\boldsymbol{P_t^2}$ was calculated for the four tracks forming the vertex found at the stage `T3FVTX4`. The distributions for the $\boldsymbol{P_t^2}$ values for $\boldsymbol{K_L \rightarrow \pi^+\pi^-e^+e^-}$ candidates are shown on the bottom of the figure 5.5.

`PT2TWO` To select the possible candidates for the $\boldsymbol{K_L \rightarrow \pi^+\pi^-\pi^0_D}$ decay, it was required that $\boldsymbol{P_t^2 < 0.0004\ GeV/c^2}$. The value $\boldsymbol{P_t^2}$ was calculated for the four tracks forming the vertex *and* a cluster not associated with a track (therefore could have possibly come from a γ). All such unmatched clusters were checked and the *minimum* value of the $\boldsymbol{P_t^2}$ was chosen. The top plots on the figure 5.5 show the $\boldsymbol{P_t^2}$ distribution for the $\boldsymbol{K_L \rightarrow \pi^+\pi^-\pi^0_D}$ candidates.

The table 5.1 gives the number of events for sub-sets `4TRPT` and `4TRGPT`, showing the split between $\boldsymbol{'97}$ and $\boldsymbol{'99}$.

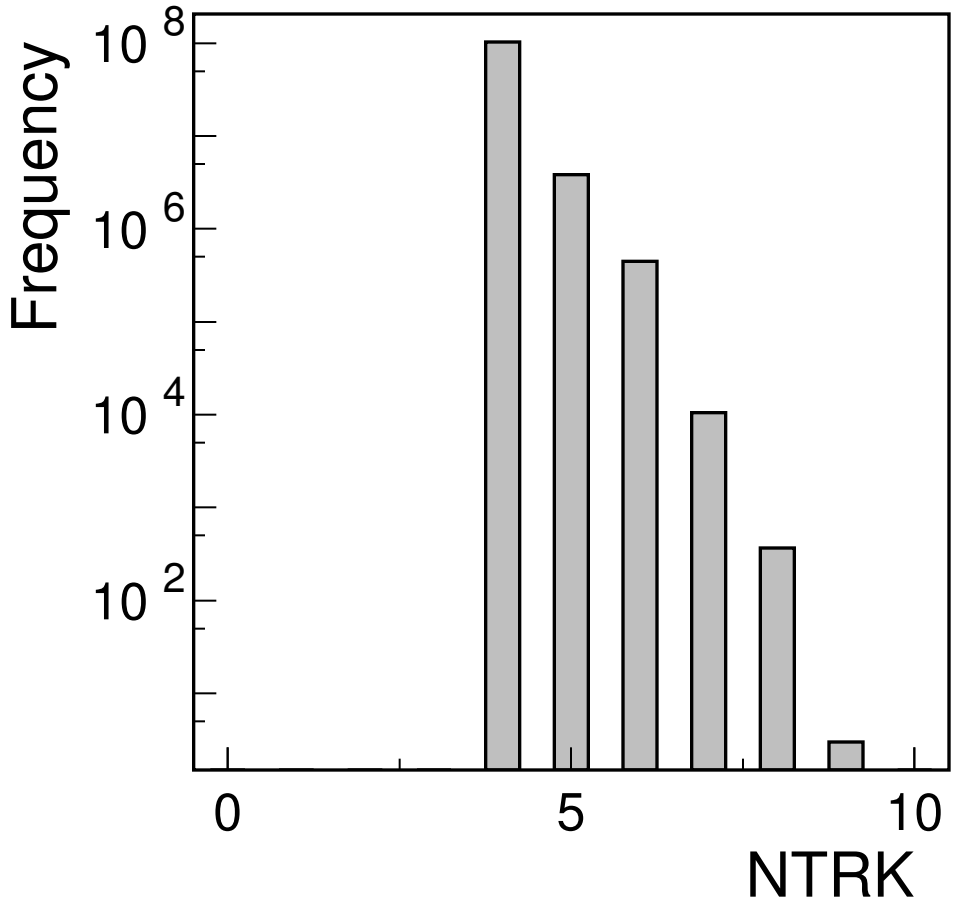

Figure 5.3: The distributions of the number of three-dimensional tracks after the 4-track vertex was found, i.e. at the stage after the requirement `T3FVTX4` was met (see section 5.1.3).

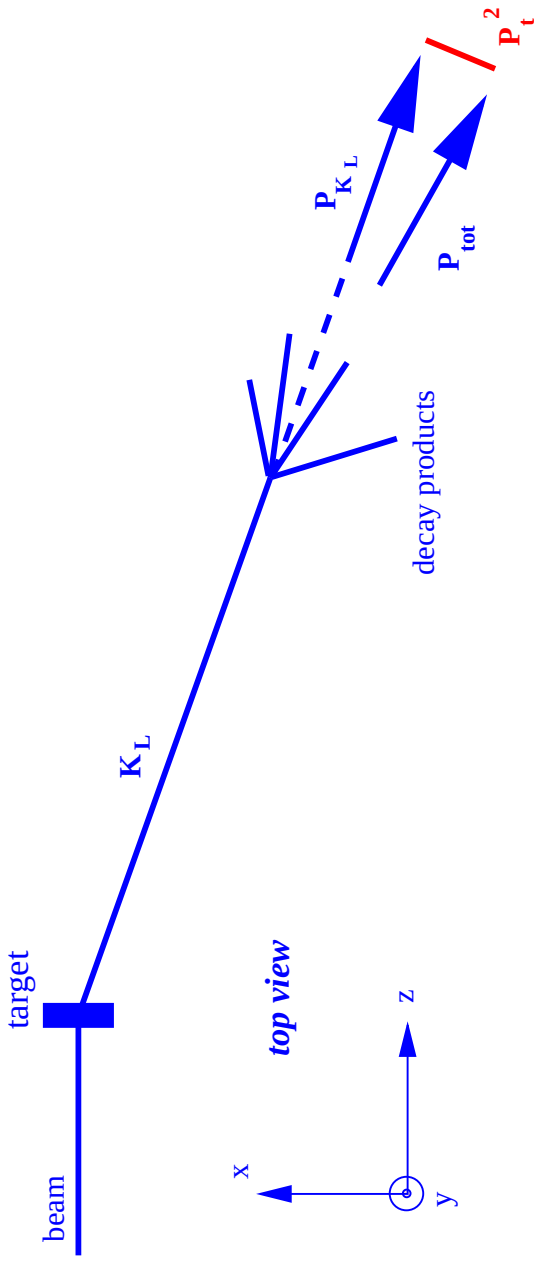

Figure 5.4: The illustration of the kinematic variable $\boldsymbol{P_t^2}$.

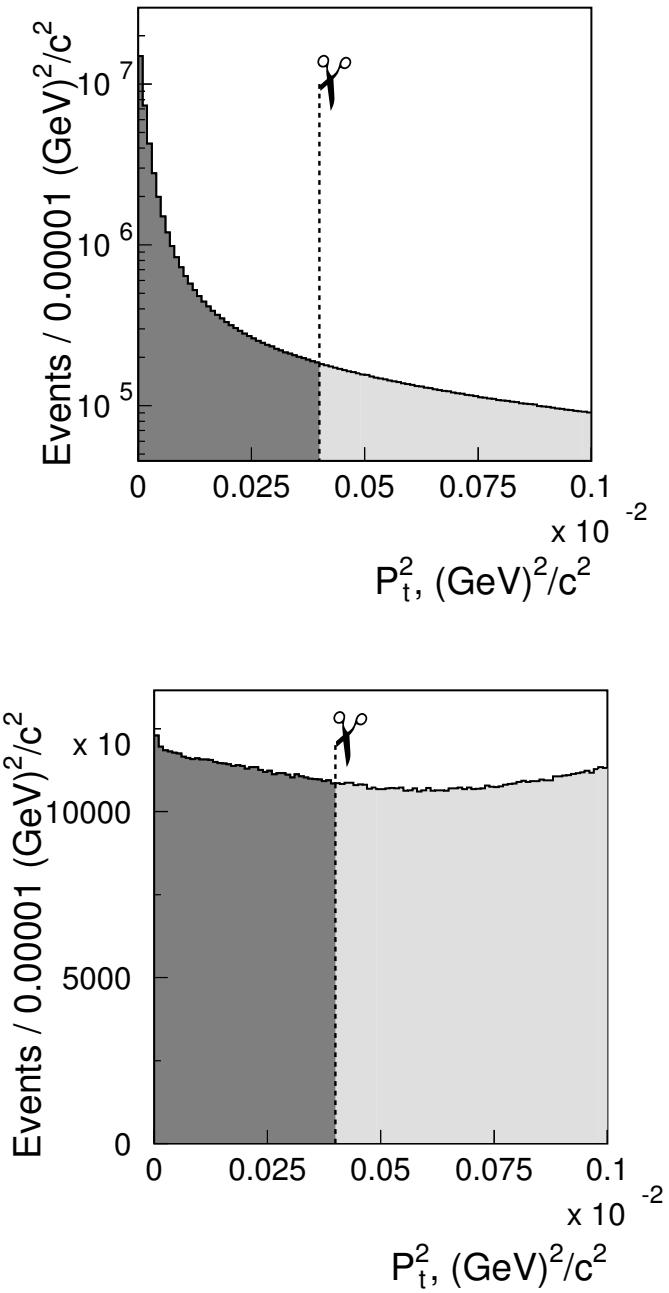

Figure 5.5: The $\boldsymbol{P_t^2}$ distributions for the $\boldsymbol{K_L \to \pi^+\pi^-\pi^0_D}$ candidates (top, note logarithmic ordinate scale) and $\boldsymbol{K_L \to \pi^+\pi^- e^+e^-}$ candidates (bottom), see section 5.2. The ordinate axis scale is logarithmic. The dashed line represents the cut value, i.e. the events are kept if $\boldsymbol{P_t^2 < 0.0004}$.

Data Set	N'^{97}	N'^{99}	$N'^{97+'99}$
4TRK (triggers)	141,782,019	262,543,446	404,325,465
4TRPT ($\pi\pi ee$ cand.)	2,578,570	4,558,013	7,136,583
4TRGPT ($\pi\pi\pi^0_D$ cand.)	25,970,536	45,876,658	71,847,194

Table 5.1: The initial reduction of the 4-track trigger data set. See section 5.2 for details. The `4TRK` refers to the events satisfying the 4-track trigger defined by the equation (4.1), see section 4.4. `4TRKPT` and `4TRKPT` represent the candidates for $K_L \to \pi^+\pi^- e^+e^-$ and $K_L \to \pi^+\pi^-\pi^0_D$ and are defined by equations (5.1) and (5.2), respectively.

5.3 Selection of $K_L \to \pi^+\pi^- e^+e^-$ Sample

All events (**'97** and **'99**) which satisfied the requirements as explained in section 5.2, were processed with a final analysis program to select the *final data sample of* $K_L \to \pi^+\pi^- e^+e^-$ *decays*. The decays were reconstructed again and the latest software available at the time was used. A number of selection criteria was applied to the reconstructed events to improve the quality of the reconstructed decays and suppress the possible backgrounds.

The major contributions to the background for the $K_L \to \pi^+\pi^- e^+e^-$ signal sample are the following decays: $K_L \to \pi^+\pi^-\pi^0_D$ with the missing photon; $K_L \to \pi^+\pi^-\gamma$ with the photon conversion in the material of the detector; overlapping K_{e3} decays and the decay $K_S \to \pi^+\pi^- e^+e^-$. A number of cuts was designed to reduce these backgrounds as described in section 5.3.1. The detailed statistics for this process of data reduction is shown in the table 5.2. All the selec-

tion criteria can be symbolically summarized by:

$$\begin{aligned} \texttt{PPEE} \quad = \quad & \texttt{GRUNS} * \texttt{T3TRAK} * \texttt{KTCLUS} * \texttt{COMBIN} * \texttt{T3FVTX4} * \texttt{NTRK} \\ & * \texttt{TWOPAIR} * \texttt{PMPM} * \texttt{LPOKIN} * \texttt{MEE} * \texttt{TRIG} * \texttt{VTXCHI} * \texttt{ZVTX} \\ & * \texttt{TPT2ONE} * \texttt{EKAON} * \texttt{MAGOFF} * \texttt{TEOP} * \texttt{HCLUS} * \texttt{MKAON} \end{aligned} \tag{5.3}$$

The requirements for T3TRAK, KTCLUS, COMBIN and T3FVTX4 were summarized in the section 5.2. The rest of the mnemonic symbols for the selection criteria are described below.

5.3.1 Selection Criteria

GRUNS At the startup of the experiment the detector components had to be tuned and optimized. The data taken during that time was not reliable and was excluded from this analysis. The following requirement was applied to the range of the KTeV runs to be included in the data set: 8245-10970 and 14625-15548 for **'97** and **'99** , correspondingly.

NTRK Require only 4 tracks in each event.

TWOPAIR Require two pion tracks and two electron tracks based on the particle ID obtained from the ratio of energy over momentum $\frac{E}{p}$, see TEOP below.

PMPM Require the two pion tracks and two electron tracks with the correct combination of signs for the charge, i.e. $e^+e^-\pi^+\pi^-$.

LPOKIN The $\left[P_L^2\right]_{\pi^0}$cut. This is the cut specifically designed to suppress the background from the $K_L \rightarrow \pi^+\pi^-\pi^0_D$ events. It puts requirements on the $P^2_{\pi^0}$ — the square of the longitudinal momentum of the possible π^0 in the reference frame where the sum of the π^+ and π^- momenta is orthogonal to the kaon momentum. Required $\left[P_L^2\right]_{\pi^0} < -0.025\ GeV^2/c^2$

Cut	**Meaning**	N	$\varepsilon = \frac{N^{cut}}{N_{\texttt{4TRKPT}}}$
4TRKPT	*Reduced 4-track trigger data*.	$\mathbf{7,136,580}$	$\mathbf{1.000}$
GRUNS	Restrict range of runs.	$\mathbf{6,972,730}$	$\mathbf{9.770 \times 10^{-1}}$
T3TRAK	Reconstruct particle tracks.	$\mathbf{6,972,730}$	$\mathbf{9.770 \times 10^{-1}}$
KTCLUS	Reconstruct energy clusters.	$\mathbf{6,972,730}$	$\mathbf{9.770 \times 10^{-1}}$
COMBIN	Reject high multiplicity events.	$\mathbf{6,972,650}$	$\mathbf{9.770 \times 10^{-1}}$
T3FVTX4	Reconstruct 4-track vertex.	$\mathbf{6,957,320}$	$\mathbf{9.749 \times 10^{-1}}$
NTRK	Require 4 tracks.	$\mathbf{6,835,300}$	$\mathbf{9.578 \times 10^{-1}}$
TWOPAIR	Require 2 π's and 2 e's.	$\mathbf{4,446,750}$	$\mathbf{6.231 \times 10^{-1}}$
PMPM	Require $\pi^+\pi^-e^+e^-$.	$\mathbf{4,336,890}$	$\mathbf{6.077 \times 10^{-1}}$
LPOKIN	Suppress $K_L \to \pi^+\pi^-\pi^0_D$.	$\mathbf{256,750}$	$\mathbf{3.598 \times 10^{-2}}$
MEE	Suppress $K_L \to \pi^+\pi^-\gamma$ decays.	$\mathbf{204,488}$	$\mathbf{2.865 \times 10^{-2}}$
TRIG	Verify trigger requirements.	$\mathbf{122,629}$	$\mathbf{1.718 \times 10^{-2}}$
VTXCHI	Require good vertex quality.	$\mathbf{67,479}$	$\mathbf{9.455 \times 10^{-3}}$
ZVTX	Constrain vertex z-position.	$\mathbf{63,809}$	$\mathbf{8.941 \times 10^{-3}}$
TPT2ONE	Momentum conservation.	$\mathbf{14,865}$	$\mathbf{2.083 \times 10^{-3}}$
EKAON	Constrain kaon energy range.	$\mathbf{13,869}$	$\mathbf{1.943 \times 10^{-3}}$
MAGOFF	Match tracks in the magnet.	$\mathbf{11,057}$	$\mathbf{1.549 \times 10^{-3}}$
TEOP	Tighten particle ID for e's.	$\mathbf{9,915}$	$\mathbf{1.389 \times 10^{-3}}$
HCLUS	Require hardware clusters for e's.	$\mathbf{9,786}$	$\mathbf{1.371 \times 10^{-3}}$
MKAON	Constrain kaon mass region.	$\mathbf{5,241}$	$\mathbf{7.344 \times 10^{-4}}$

Table 5.2: Summary of cuts for the selection of $K_L \to \pi^+\pi^-e^+e^-$ data sample. The meaning of each cut is explained in more detail in sections 5.2 and 6.4. The input into the selection procedure is the reduced data sample obtained according to selection criteria summarized in section 5.2. The output is the $K_L \to \pi^+\pi^-e^+e^-$ data sample used in this analysis. In the table N is the number of events after a cut and ε is the ratio of the number of events after a particular cut over the number of events on the input.

`MEE` Cut on the M_{ee} to reject the background from the $K_L \to \pi^+\pi^-\gamma$ decays, where the photon externally converted into e^+e^--pair in the material of the vacuum window. Required $M_{ee} > 0.002\ GeV/c^2$.

`TRIG` The elements of the 4-track trigger defined in equation (4.1) were verified with the reconstructed quantities to inure that the selected event would have satisfied the trigger.

`VTXCHI` The cut on the vertex χ^2, see section 5.1.3. The four reconstructed tracks form a vertex within decay volume with $\chi^2_{vtx} < 30$.

`ZVTX` The cut on the vertex Z position (z_{vtx}). This is the fiducial cut to make sure that the vertex is located within the decay pipe. Required $95\ m < z_{vtx} < 158\ m$.

`TPT2ONE` The tight 4-track P_t^2cut to suppress background from any background with missing particles. Required $P_t^2 < 6.0 \times 10^{-5}\ GeV^2/c^2$.

`EKAON` The kaon energy cut. This cut is designed to cut the background from $K_S \to \pi^+\pi^-e^+e^-$decays. Required $E_{\pi\pi ee} < 200\ GeV$.

`MAGOFF` Cuts on the tracks matching at the magnet. Require x-offsets a the magnet to be less than 0.0015 m and 0.003 m for pion and electron tracks, respectively.

`TEOP` The $\frac{E}{P}$ cut, i.e. particle ID$'s$ for pions and electrons. For electrons this ratio is close to unity and for the hadrons it less than one. Require $0.95 < \frac{E}{p} < 1.05$ for the electrons.

`HCLUS` Require hardware clusters for the electrons. No such requirement was imposed on pions.

`MKAON` The kaon mass cut. Required $\mathbf{0.492\,GeV/c^2 < M_{\pi\pi ee} < 0.504\,GeV/c^2}$.

5.3.2 The Final Sample

The final sample of $K_L \to \pi^+\pi^- e^+e^-$ decays contained $\mathbf{5241}$ candidate events. The $\pi\pi ee$ mass distribution, before the kaon mass cut `MKAON`, is shown on the figure 5.6. The background remaining in this sample was estimated with a fit. The "wings" (outside the `MKAON` region) of the mass distribution were fit to a *background-shape function*, which was chosen as a sum of *Gaussian and seventh order polynomial*. This function then was extrapolated into the mass peak (inside the `MKAON` region) and the number of background events was calculated as the integral of that function within the limits defined by the kaon mass cut `MKAON`, see figure 5.7. The estimated background was $\mathbf{204}$ events. Two components to the uncertainty on this number were considered. First, the uncertainty due to the errors on the fit parameters of the background-shape function was calculated using the error matrix of this parameters obtained with MINUIT software package [63]. Another contribution was obtained by varying the the wing regions used for the fit. The result for the background estimation is as follows:

$$n = 204 \pm 14 \tag{5.4}$$

where $14 \approx \sqrt{7^2 + 12^2}$ for the two contributions.

5.4 Selection of $K_L \to \pi^+\pi^-\pi^0_D$ Sample

To select $K_L \to \pi^+\pi^-\pi^0_D$ data sample all (both '97 and '99) events from the subset `4TRKGPT` were processed with analysis program similar to the one used to select $K_L \to \pi^+\pi^- e^+e^-$ decays. All requirements can be summarized as

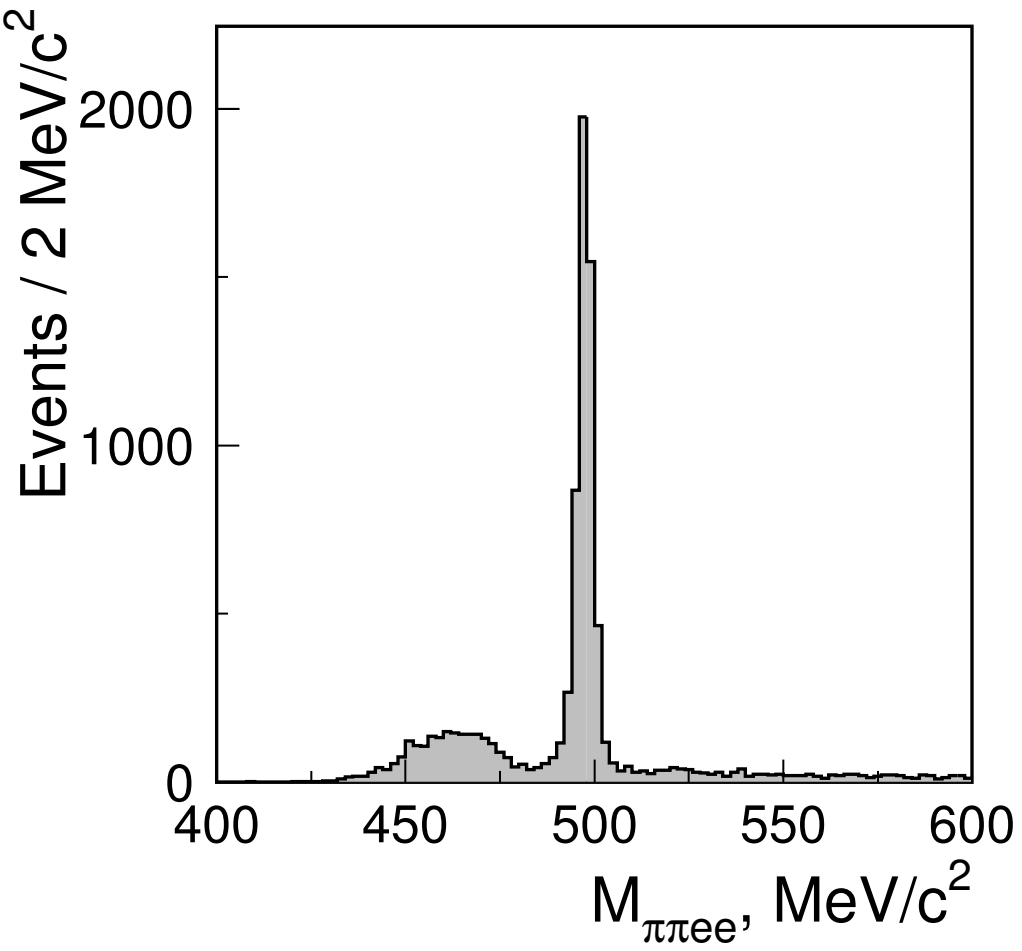

Figure 5.6: The $\pi\pi ee$ invariant mass distribution for the $K_L \to \pi^+\pi^- e^+ e^-$ candidates after all cuts except the kaon mass cut. The "hump" on the left is mostly due to the remaining background from $K_L \to \pi^+\pi^-\pi^0_D$ decays.

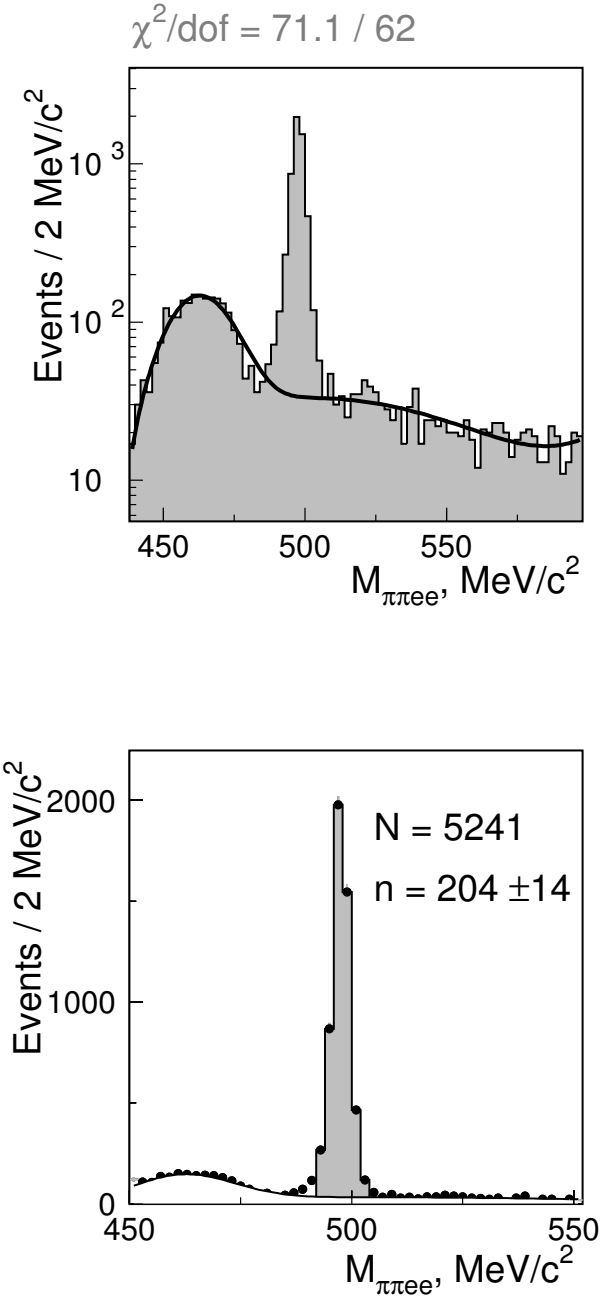

Figure 5.7: Background fit and subtraction for the final $K_L \to \pi^+\pi^- e^+ e^-$ data sample.

follows:

$$\begin{aligned} \texttt{PMZD} \quad = \quad & \texttt{GRUNS} * \texttt{T3TRAK} * \texttt{KTCLUS} * \texttt{COMBIN} * \texttt{T3FVTX4} * \texttt{NTRK} \\ & * \texttt{TWOPAIR} * \texttt{PMPM} * \texttt{RPOKIN} * \texttt{MEE} * \texttt{MEEG} * \texttt{TRIG} * \texttt{VTXCHI} * \texttt{ZVTX} \\ & * \texttt{TPT2TWO} * \texttt{EG} * \texttt{EKAON} * \texttt{MAGOFF} * \texttt{TEOP} * \texttt{HCLUS} * \texttt{MKAON} \end{aligned} \tag{5.5}$$

where the selection criteria were identical to ones for the decay $\boldsymbol{K_L \to \pi^+\pi^- e^+ e^-}$, with two additional cuts to account for the presence of the photon and $\boldsymbol{\pi^0}$ and change in the meaning and value of the $\boldsymbol{P^2_{\pi^0}}$ cut

`MEEG` The cut on $\boldsymbol{M_{ee\gamma}}$, i.e. the $\boldsymbol{\pi^0}$ mass cut. Required the $\boldsymbol{M_{ee\gamma}}$ to be within $\boldsymbol{10\ MeV}$ of the $\boldsymbol{\pi^0}$mass.

`TPT2TWO` The loose 4-track $\boldsymbol{P_t^2}$cut to suppress background from any background with missing particles. Required $\boldsymbol{P_t^2 < 2.0 \times 10^{-4}\ GeV^2/c^2}$.

`EG` The photon energy cut `EG`. Required the $\boldsymbol{E_\gamma > 1\ GeV}$.

`RPOKIN` This $\boldsymbol{\left[P_L^2\right]_{\pi^0}}$ cut had different value and meaning in comparison to the `LPOKIN`. In the case of $\boldsymbol{K_L \to \pi^+\pi^-\pi^0_D}$ this cut was necessary to insure that the $\boldsymbol{\pi^0}$ satisfied the kinematic constraint on it's momentum. The requirement was $\boldsymbol{\left[P_L^2\right]_{\pi^0} > 0\ GeV^2/c^2}$, to avoid the resolution effects on the value of the longitudinal component of $\boldsymbol{\pi^0}$ momentum.

The detailed statistics for the selection process is given in the table 5.3 The final sample of the $\boldsymbol{K_L \to \pi^+\pi^-\pi^0_D}$ decays contained $\boldsymbol{14,629,750}$ events and virtually no background, see figure 5.8 for the mass distribution. The wings of that distributions are most likely contain poorly reconstructed $\boldsymbol{K_L \to \pi^+\pi^-\pi^0_D}$ decays. But even if one would assume that all the events in the wings came from some unknown background the level of such background would be negligible. To illustrate this point the wings were fitted to the *ninth order polynomial*, and the

Cut	**Meaning**	N	$\varepsilon = \frac{N^{cut}}{N_{\texttt{4TRKGPT}}}$
4TRKGPT	*Reduced 4-track trigger data*.	$\mathbf{71,847,200}$	$\mathbf{1.000}$
GRUNS	Restrict range of runs.	$\mathbf{70,108,300}$	$\mathbf{9.758 \times 10^{-1}}$
T3TRAK	Reconstruct particle tracks.	$\mathbf{70,108,300}$	$\mathbf{9.758 \times 10^{-1}}$
KTCLUS	Reconstruct energy clusters.	$\mathbf{70,108,300}$	$\mathbf{9.758 \times 10^{-1}}$
COMBIN	Reject high multiplicity events.	$\mathbf{70,107,600}$	$\mathbf{9.758 \times 10^{-1}}$
T3FVTX4	Reconstruct 4-track vertex.	$\mathbf{69,989,600}$	$\mathbf{9.742 \times 10^{-1}}$
NTRK	Require 4 tracks.	$\mathbf{69,255,500}$	$\mathbf{9.639 \times 10^{-1}}$
TWOPAIR	Require 2 π's and 2 e's.	$\mathbf{48,765,000}$	$\mathbf{6.787 \times 10^{-1}}$
PMPM	Require $\pi^+\pi^-e^+e^-$.	$\mathbf{48,328,400}$	$\mathbf{6.727 \times 10^{-1}}$
RPOKIN	Remove resolution effects.	$\mathbf{41,055,000}$	$\mathbf{5.714 \times 10^{-1}}$
MEE	Suppress $K_L \to \pi^+\pi^-\gamma$ decays.	$\mathbf{28,700,100}$	$\mathbf{3.995 \times 10^{-1}}$
MEEG	Constrain π^0 mass region.	$\mathbf{25,583,700}$	$\mathbf{3.561 \times 10^{-1}}$
TRIG	Verify trigger requirements.	$\mathbf{19,604,400}$	$\mathbf{2.729 \times 10^{-1}}$
VTXCHI	Require good vertex quality.	$\mathbf{18,929,700}$	$\mathbf{2.635 \times 10^{-1}}$
ZVTX	Constrain vertex z-position.	$\mathbf{18,533,500}$	$\mathbf{2.580 \times 10^{-1}}$
TPT2TWO	Momentum conservation.	$\mathbf{18,075,200}$	$\mathbf{2.516 \times 10^{-1}}$
EG	Photon minimum energy.	$\mathbf{18,033,700}$	$\mathbf{2.510 \times 10^{-1}}$
EKAON	Constrain kaon energy range.	$\mathbf{17,966,500}$	$\mathbf{2.501 \times 10^{-1}}$
MAGOFF	Match tracks in the magnet.	$\mathbf{17,077,400}$	$\mathbf{2.377 \times 10^{-1}}$
TEOP	Tighten particle ID for e's.	$\mathbf{15,670,600}$	$\mathbf{2.181 \times 10^{-1}}$
HCLUS	Require hardware clusters for e's.	$\mathbf{15,394,900}$	$\mathbf{2.143 \times 10^{-1}}$
MKAON	Constrain kaon mass region.	$\mathbf{14,629,800}$	$\mathbf{2.036 \times 10^{-1}}$

Table 5.3: Summary of cuts for the selection of $K_L \to \pi^+\pi^-\pi^0_D$ data sample. The meaning of each cut is explained in more detail in section 5.4. See caption to table 5.2 for the meaning of N and ε .

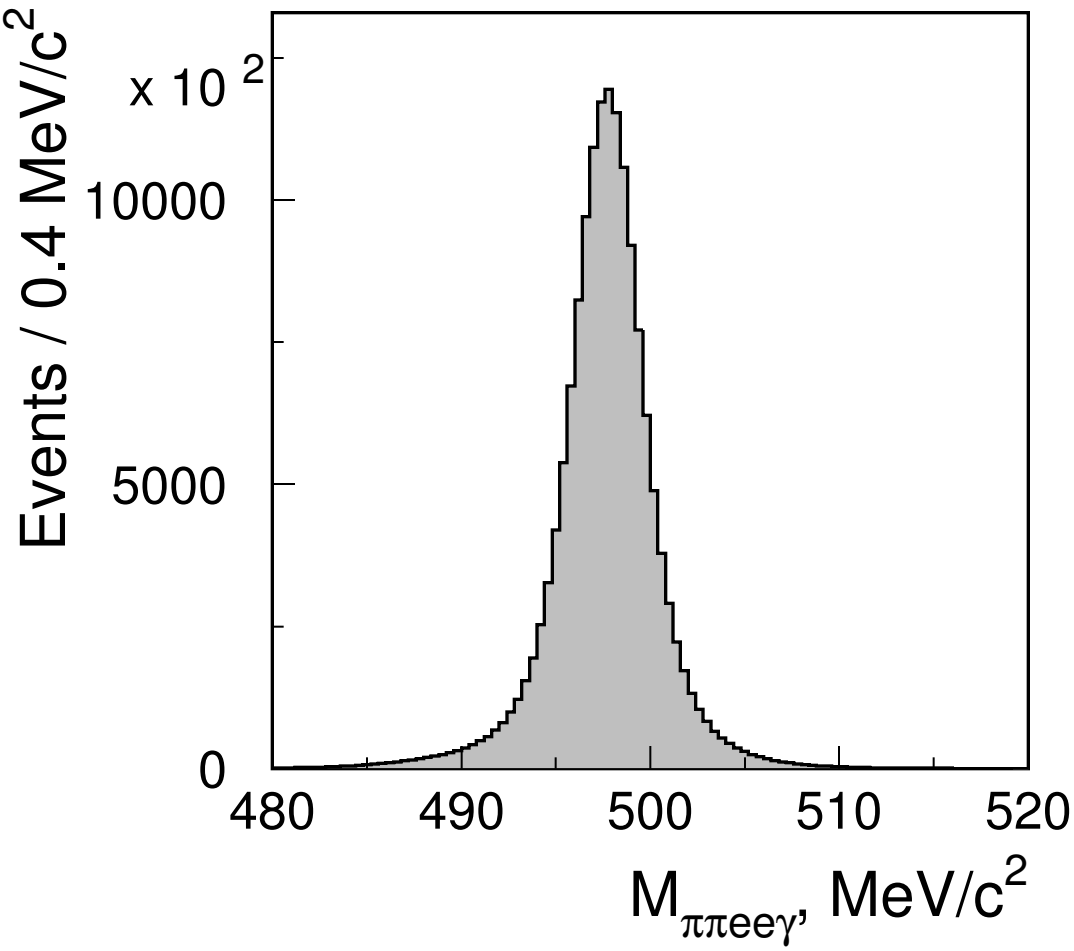

Figure 5.8: The $\pi\pi ee\gamma$ invariant mass distribution for the $K_L \to \pi^+\pi^-\pi^0_D$ candidates after all cuts except the kaon mass cut. The signal has virtually no background, see figure 5.9.

number of possible background events was estimated in a way similar to the case of $K_L \rightarrow \pi^+\pi^-e^+e^-$ (figure 5.9). This estimation resulted in approximately 1700 events, i.e. four orders of magnitude less than the sample size.

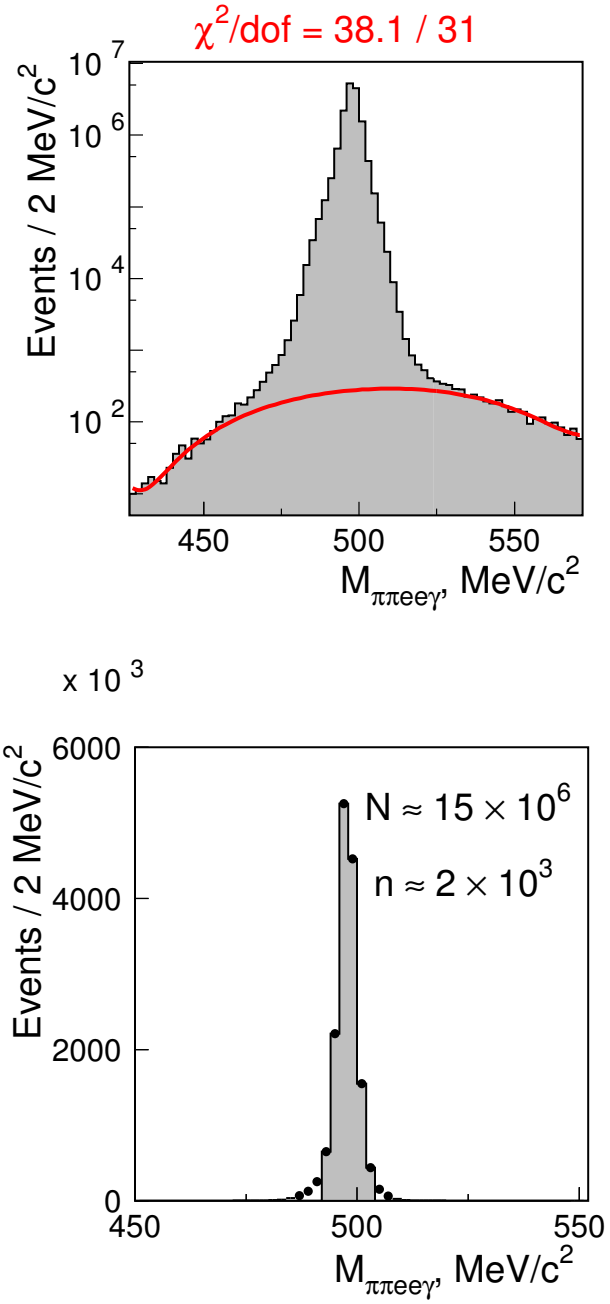

Figure 5.9: Background fit and rate estimation (n) for the $K_L \to \pi^+\pi^-\pi^0_D$ statistical data sample (size N).

Chapter 6

Monte Carlo Simulation Studies

The *Monte Carlo* simulation (MC) was an integral part of the analysis. It was crucial for the estimation of the $K_L \to \pi^+\pi^- e^+ e^-$ model parameters and was used to calculate the acceptance for the asymmetry measurement (chapter 7). In addition the MC simulated sample of $K_L \to \pi^+\pi^-\pi^0_D$ decays was used to verify the overall quality of the KTeV MC by comparing it to the $K_L \to \pi^+\pi^-\pi^0_D$ high-statistics data sample. The detailed simulation of the KTeV experiment was accomplished by a computer program based on the software package KTEVMC (v5_06) developed by the members of the KTeV collaboration.

The simulation procedure included five main stages: (*i*) kaon or hyperon was generated at the BeO target and propagated to the decay point in the vacuum region (see chapter 4); (*ii*) the particle was then forced to decay into a specific final state and the decay products were traced through the detector; (*iii*) the detector response to different secondary and tertiary decay products was simulated, including the digitization of the signals; (*iv*) the trigger requirements were applied and the result was written in the same format as an actual data event with additional data banks providing the *true values* of the generation parameters; (*v*) finally, these two categories of simulated events were reconstructed and processed by the analysis program described in chapter 5 to select the $K_L \to \pi^+\pi^- e^+ e^-$ and

$K_L \rightarrow \pi^+\pi^-\pi^0_D$ *MC samples*. In addition, other modes were generated and passed through the above five stages to estimate the possible background contributions. The details related to the generation of the MC samples are discussed in this chapter; a detailed description of the KTeV Monte Carlo simulation can be found in [38, 42, 46, 47].

6.1 The Parent Particle Production and Decay

The energy and direction of the parent particle (kaon or hyperon) generated within the BeO target was chosen on the basis of the measurements of K^+, K^-, Λ and Ξ production (a detailed discussion of the kaon and hyperon production can be found in section 4.1.1 of [37] and in references therein). The energy spectrum of K_L component was tuned to match the KTeV $K_L \rightarrow \pi^+\pi^-$ data. The particles produced in the target were traced through the beamline into the vacuum decay region along the trajectory defined by the particle's momentum vector. The particles could be lost in the absorbers or in the upstream collimators. For kaons, the regeneration of K_L in the absorbers was taken into account. The scattering in the defining collimator was simulated based on the scattering observed in the $K_L \rightarrow \pi^+\pi^-$ data.

The decay position of hyperons and K'_Ls was determined by the proper life time of a particular particle (see section 4.1). The z-position of a kaon decay was calculated based on the probability for the decay of neutral kaon, either K_L or K_S state, accounting for the interference between K_L and K_S (see section 2.1). For $100\ GeV$ K_L's the mean decay length is about $3\ km$ (section 4.1). Therefore the distribution of the K_L decay z-positions is approximately uniform in the range $90\ m$ to $160\ m$. The parent particle was forced to decay at a z-position according to the decay probability distribution of the K_L or K_S. Once the decay vertex was chosen, a specific decay was generated in the rest frame of the decaying particle.

The generation of all the decay modes relevant to this analysis will be described in sections 6.3, 6.4 and 6.5. After the generation each particle's momentum vector was boosted into the laboratory reference frame for tracing purposes.

The trajectory of the decay products was influenced by the interaction with the detector elements and the effects of the magnetic field. The interaction with the material was simulated taking into account the following physical processes: (*i*) Coulomb multiple scattering of the charged particles; (*ii*) bremsstrahlung for electrons and positrons; (*iii*) photon conversion into e^+e^- pairs; and (*iv*) energy loss according to dE/dx empirical law.

In addition, the charged pions could decay into muon and neutrino. All the secondary and tertiary decay products were also traced through the detector. A *magnetic field map* for the analysis magnet was used to calculate the motion of charged particles in the spectrometer. The magnetic field of the Earth was also taken into account. A detailed description of particle tracing can be found in section 4.3 of [47] and references therein.

Various accidental activity in the detector could result from the high rate of kaons and neutrons in the beam. Also the particles from the decays occurring far upstream of the detector and the interactions of the beam with the detector material could add signals to the the readout of the otherwise good kaon decays. The accidental activity was simulated by superimposing the events accepted by the accidental trigger, based on the 90 degrees monitor described in the section 4.1, on the MC events in the correct proportions. The energy in the calorimeter crystals and hits in the drift chamber wires (recorded in the accidental events) were added to the Monte Carlo simulated events. The accidental activity rate for each MC run was scaled proportionally to the number of $K_L \to \pi^+\pi^-\pi^0_D$ events (section 5.4) in that run.

6.2 The Detector Response to the Decay Products

The response of each detector element was measured with high statistics data samples of K_{e3} and $K_L \rightarrow \pi^+\pi^-$ decays according to the procedures described in chapter 4. These measurements were then used to simulate the detector response for a given particle.

The position of the particle in a drift chamber was smeared according to the resolution determined using K_{e3} data. The distance to the closest wire was then calculated and converted into the drift time TDC counts using the inverse maps measured with K_{e3} decays (see sections 4.2.2 and 5.1.1). The drift chamber hits from the accidental trigger data were used to simulate the effects of the accidental activity.

The energy deposit in each block of the CsI calorimeter and the position of the energy cluster were simulated using the shower libraries generated with GEANT package [64]. The electromagnetic and hadronic showers were generated separately. The libraries contained longitudinal and transverse shower profiles binned according to particle type, energy and position. The effects of the shower leakage across the beam-holes was simulated based on the K_{e3} data. The generated energy of the particle was smeared according to resolution function depending on the particle xy-position, energy and on the size of the CsI block (small or large). The energy was then distributed among the individual blocks according to the shower libraries. Within each block the energy was distributed according the *shower time profile*. These time profiles contained 6 consecutive $19\ ns$ RF buckets (section 4.1) and were determined using K_{e3} data. The energy deposit from the accidental activity was added to each crystal. The simulated energy in each CsI block was converted into ADC counts according to the inverse maps measured with K_{e3} decays (see sections 4.2.4 and 5.1.2).

The other simulated detector elements included: photon vetoes, transition radiation detectors and the muon identification system (section 4.2.6). The pions and muons were traced through the veto detectors. The energy of a minimum ionizing particle was deposited in the scintillating veto and muon counters and the trajectory was changed to account for the effects of the multiple scattering. If the particle left the fiducial volume of the detector it was considered lost. The response of the veto detectors to the electro-magnetically interacting particles was done differently. The energy of a photon or electron was smeared according to the Gaussian resolution function and then converted into ADC values. The transition radiation detectors were treated as the material in the detector and otherwise were not simulated for this analysis. The muons had minimum interaction in the calorimeter and were traced through the steel wall (section 4.2.6) taking into account the $\frac{dE}{dx}$ energy loss according to the Bethe-Bloch equation. The response of the muon scintillators was then simulated.

The trigger requirements (section 4.3) were applied after the responses from all detector elements were simulated. All the KTeV trigger levels were simulated in the Monte Carlo, including the behavior of the hit- and cluster-counting systems (section 5.2).

6.3 The Simulation Check

The copious $K_L \rightarrow \pi^+\pi^-\pi^0_D$ decays were used to check the quality of the simulation. The MC sample was compared to the $K_L \rightarrow \pi^+\pi^-\pi^0_D$ data sample containing $14,629,750$ events (section 5.4). This decay was generated in two stages in the KTeV MC: $K_L \rightarrow \pi^+\pi^-\pi^0$ and $\pi^0 \rightarrow e^+e^-\gamma$. The matrix element for the $K_L \rightarrow \pi^+\pi^-\pi^0$ decays was calculated based on the series expansion suggested by Weinberg [53]. The modern conventional parameterization gives

the following expression for the matrix element (see Meson Particle Listings for K_L in [1])

$$\left|\mathcal{M}\left(K_L \to \pi^+\pi^-\pi^0\right)\right|^2 = 1 + gu + hu^2 + kv^2 \tag{6.1}$$

where the values of the parameters are

$$g = 0.678 \pm 0.008 \tag{6.2}$$

$$h = 0.076 \pm 0.006 \tag{6.3}$$

$$k = 0.0099 \pm 0.0015 \tag{6.4}$$

and the variables u and v are functions of four-vectors of kaon P_K and the three pions P_i:

$$u = \frac{s_3 - s_0}{m_1^2} \tag{6.5}$$

$$v = \frac{s_1 - s_2}{m_1^2} \tag{6.6}$$

$$s_i = (P_K - P_i)^2 = (m_K - m_i)^2 - 2m_K T_i\,,\ i = 1,2,3 \tag{6.7}$$

$$s_0 = \frac{1}{3}\sum_i^3 s_i = \frac{1}{3}\left(m_K^2 + m_1^2 + m_2^2 + m_3^2\right) \tag{6.8}$$

with m_i and T_i denoting the mass and kinetic energy of i^{th} pion and index 3 corresponding to π^0. The decay $\pi^0 \to e^+e^-\gamma$ was simulated based on the formalism developed by Kroll and Wada [54] including the radiative corrections [55] and the empirical form-factor at the $\pi^0\gamma\gamma$ vertex (see Meson Particle Listings for π^0 in [1])

$$F(x) = 1 + ax \tag{6.9}$$

where

$$a = 0.032 \pm 0.004 \tag{6.10}$$

$$x = \left(\frac{m_{ee}}{m_{\pi^0}}\right)^2 \tag{6.11}$$

The decays $K_L \to \pi^+\pi^-\pi^0$ and $\pi^0 \to e^+e^-\gamma$ were generated in the kaon and pion rest frames, correspondingly. The momenta of the decay products were then boosted into the lab reference frame and detector response was simulated as described in section 6.2.

The generated $K_L \to \pi^+\pi^-\pi^0_D$ MC events were reconstructed by the same analysis program which was used to analyze real data. This program selected $1,884,506$ events for the $K_L \to \pi^+\pi^-\pi^0_D$ MC sample to compare against the $K_L \to \pi^+\pi^-\pi^0_D$ data. The selection criteria were identical for data and Monte Carlo. The MC selection efficiencies are shown in the table 6.1. Figure 6.1 shows the kaon invariant mass comparison for both samples after all cuts. The agreement is quite good, showing that the Monte Carlo can simulate the shape of the mass distribution correctly.

The comparison plots are shown on the figures 6.1 to 6.5. The three plots on the figure 6.2 show the position of the decay vertex in x, y, and z. The beam x- and y-profiles agree quite well with some minor disagreement at the level of four orders-of-magnitude less than the maximum of the distribution. Figure 6.3 shows the x-and y-track offsets at the magnet plane for electrons and pions. The visible disagreement for the y-offsets had no effect on the fit results (section 7.1). The x- and y-tracks' projections to the drift chambers and the calorimeter are shown on the figure 6.4. The Monte Carlo simulates the beam regions quite well for both x- and y-views. A number of kinematic variables were also investigated. The shape of the distribution for the kinematic variable $\left[P_L^2\right]_{\pi^0}$ is reproduced by Monte Carlo correctly (see figure 6.5).

6.4 Simulation Of $K_L \to \pi^+\pi^-e^+e^-$ Signal

The $K_L \to \pi^+\pi^-e^+e^-$ decays simulation was based on the phenomenological model described in chapter 3. The matrix element (3.35) was calculated using

Cut	**Meaning**	N	$\varepsilon = \frac{N^{cut}}{N_{\texttt{4TRKGPT}}}$
`4TRKGPT`	*Trigger-accepted MC events*.	$\mathbf{11,685,600}$	$\mathbf{1.000}$
`T3TRAK`	Reconstruct particle tracks.	$\mathbf{11,684,600}$	$\mathbf{9.999 \times 10^{-1}}$
`KTCLUS`	Reconstruct energy clusters.	$\mathbf{11,684,600}$	$\mathbf{9.999 \times 10^{-1}}$
`COMBIN`	Reject high multiplicity events.	$\mathbf{11,621,100}$	$\mathbf{9.945 \times 10^{-1}}$
`T3FVTX4`	Reconstruct 4-track vertex.	$\mathbf{8,297,360}$	$\mathbf{7.101 \times 10^{-1}}$
`NTRK`	Require 4 tracks.	$\mathbf{8,206,790}$	$\mathbf{7.023 \times 10^{-1}}$
`TWOPAIR`	Require 2 π's and 2 e's.	$\mathbf{5,614,410}$	$\mathbf{4.805 \times 10^{-1}}$
`PMPM`	Require $\pi^+\pi^-e^+e^-$.	$\mathbf{5,572,840}$	$\mathbf{4.769 \times 10^{-1}}$
`RPOKIN`	Remove resolution effects.	$\mathbf{4,508,980}$	$\mathbf{3.859 \times 10^{-1}}$
`MEE`	Suppress $K_L \to \pi^+\pi^-\gamma$ decays.	$\mathbf{3,853,540}$	$\mathbf{3.298 \times 10^{-1}}$
`MEEG`	Constrain π^0 mass region.	$\mathbf{3,001,920}$	$\mathbf{2.569 \times 10^{-1}}$
`TRIG`	Verify trigger requirements.	$\mathbf{2,466,430}$	$\mathbf{2.110 \times 10^{-1}}$
`VTXCHI`	Require good vertex quality.	$\mathbf{2,393,110}$	$\mathbf{2.048 \times 10^{-1}}$
`ZVTX`	Constrain vertex z-position.	$\mathbf{2,342,990}$	$\mathbf{2.005 \times 10^{-1}}$
`TPT2TWO`	Momentum conservation.	$\mathbf{2,240,240}$	$\mathbf{1.917 \times 10^{-1}}$
`EG`	Photon minimum energy.	$\mathbf{2,235,210}$	$\mathbf{1.913 \times 10^{-1}}$
`EKAON`	Constrain kaon energy range.	$\mathbf{2,229,610}$	$\mathbf{1.908 \times 10^{-1}}$
`MAGOFF`	Match tracks in the magnet.	$\mathbf{2,140,140}$	$\mathbf{1.831 \times 10^{-1}}$
`TEOP`	Tighten particle ID for e's.	$\mathbf{2,006,520}$	$\mathbf{1.717 \times 10^{-1}}$
`HCLUS`	Require hardware clusters for e's.	$\mathbf{1,980,030}$	$\mathbf{1.694 \times 10^{-1}}$
`MKAON`	Constrain kaon mass region.	$\mathbf{1,884,510}$	$\mathbf{1.613 \times 10^{-1}}$

Table 6.1: Summary of cuts for the selection of $K_L \to \pi^+\pi^-\pi^0_D$ Monte Carlo sample. The meaning of each cut was explained in more detail in chapter 5. N is the number of the MC events accepted by the 4-track trigger and the ratio ε is calculated with respect to that number. Compare the statistics to the table 5.3.

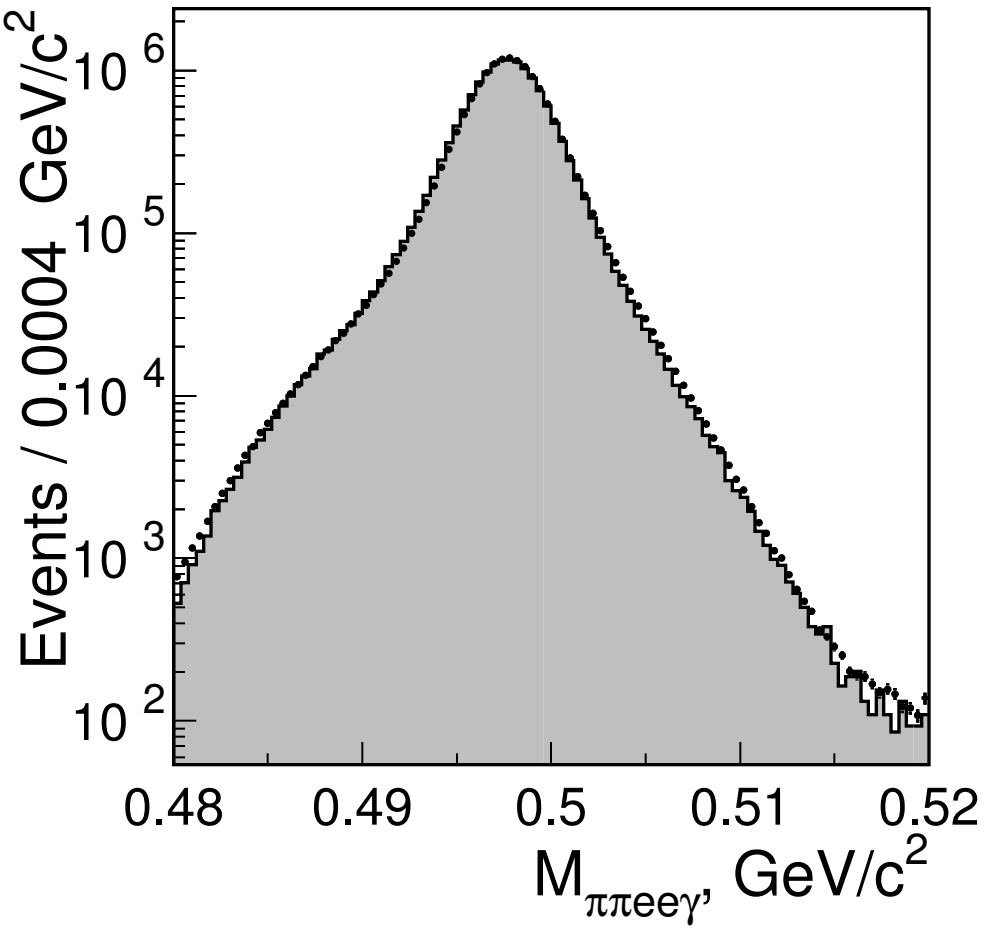

Figure 6.1: Comparison of $M_{\pi\pi ee\gamma}$ distributions for $K_L \to \pi^+\pi^-\pi^0_D$ sample. The dots with error bars show data and the filled histogram corresponds to the Monte Carlo simulation. The ordinate has logarithmic scale.

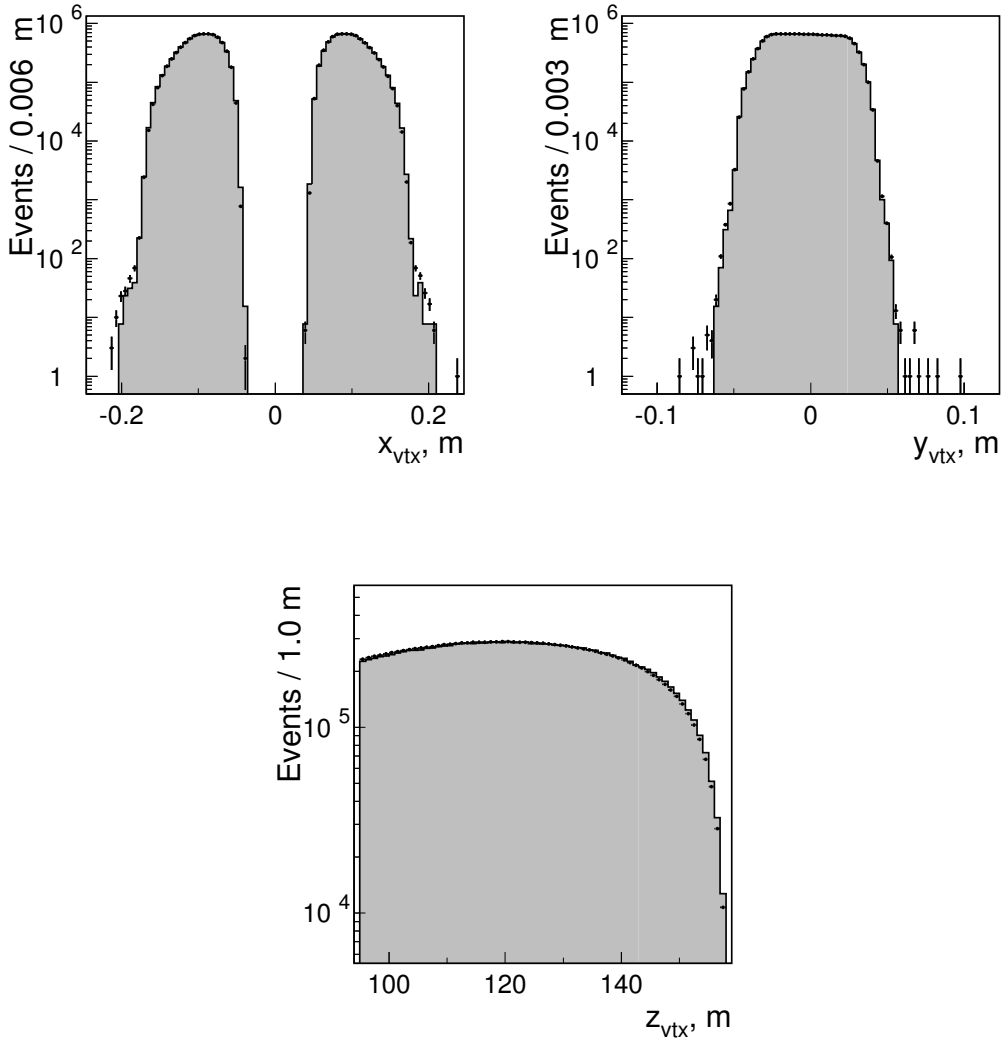

Figure 6.2: Comparison of x_{vtx}, $y_{vtx}$and z_{vtx} distributions for $K_L \to \pi^+\pi^-\pi^0_D$ sample. The dots with error bars show data and the filled histogram corresponds to the Monte Carlo simulation. The ordinate has logarithmic scale.

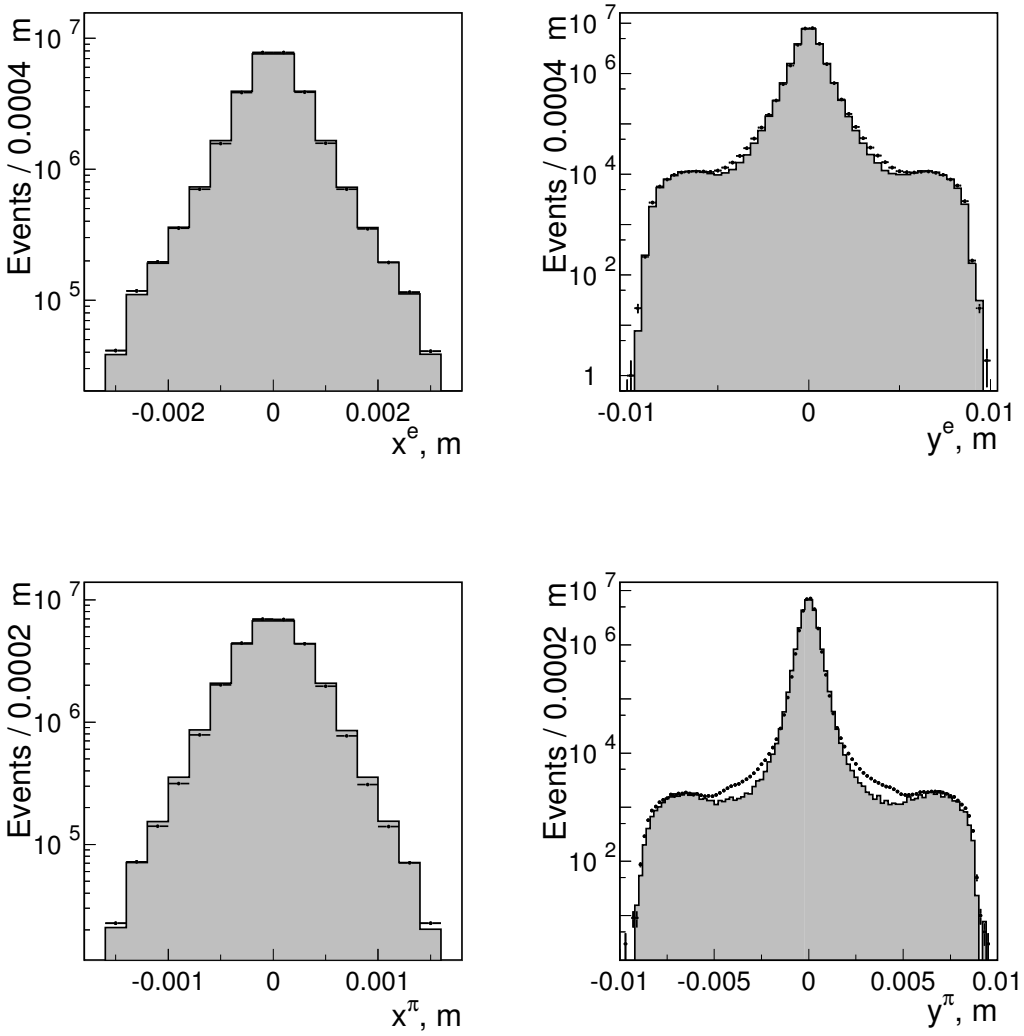

Figure 6.3: Comparison of x^e_{magoff}, y^e_{magoff}, x^π_{magoff} and y^π_{magoff} distributions for $K_L \to \pi^+\pi^-\pi^0_D$ sample. The dots with error bars show data and the filled histogram corresponds to the Monte Carlo simulation. The ordinate has logarithmic scale.

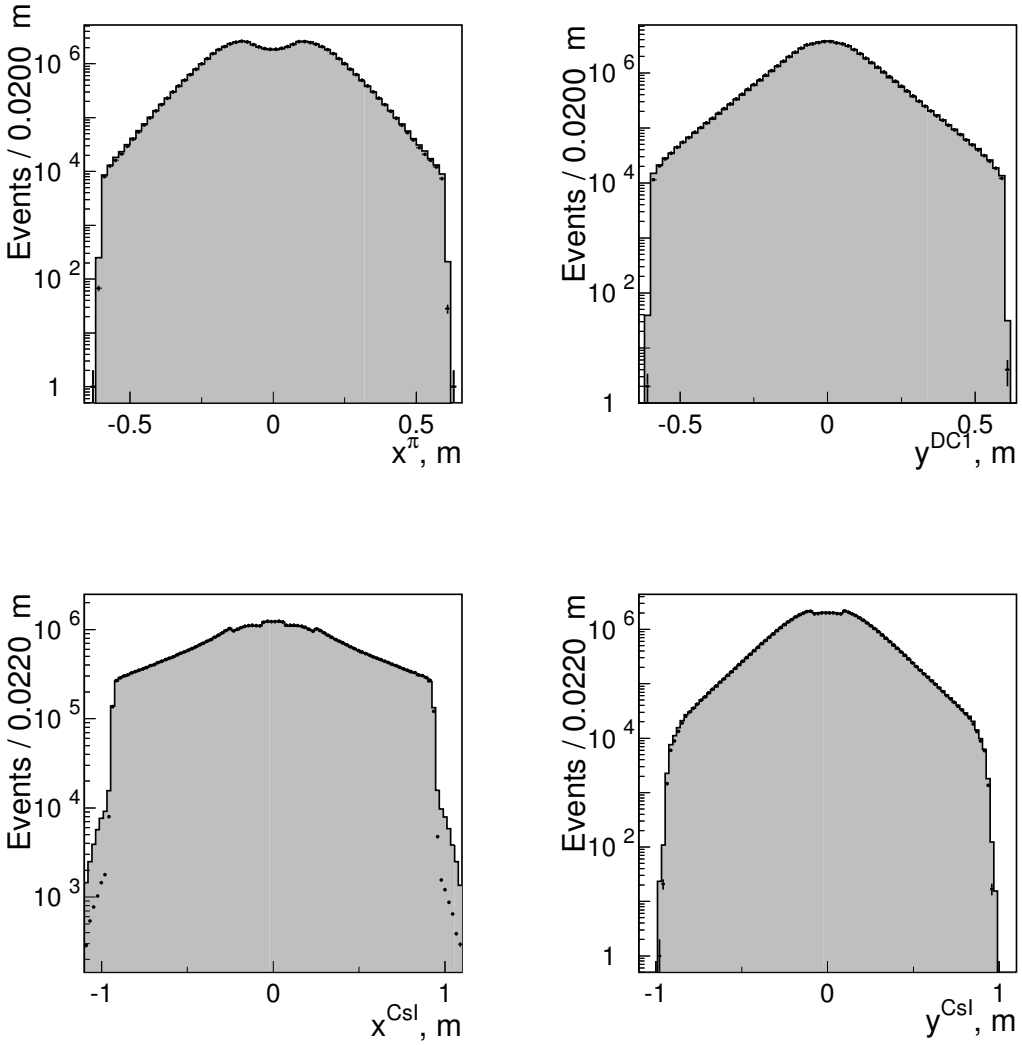

Figure 6.4: Comparison of x_{int}^{DC1}, y_{int}^{DC1}, x_{int}^{CsI} and y_{int}^{CsI} distributions for $K_L \to \pi^+\pi^-\pi_D^0$ sample. The dots with error bars show data and the filled histogram corresponds to the Monte Carlo simulation. The ordinate has logarithmic scale.

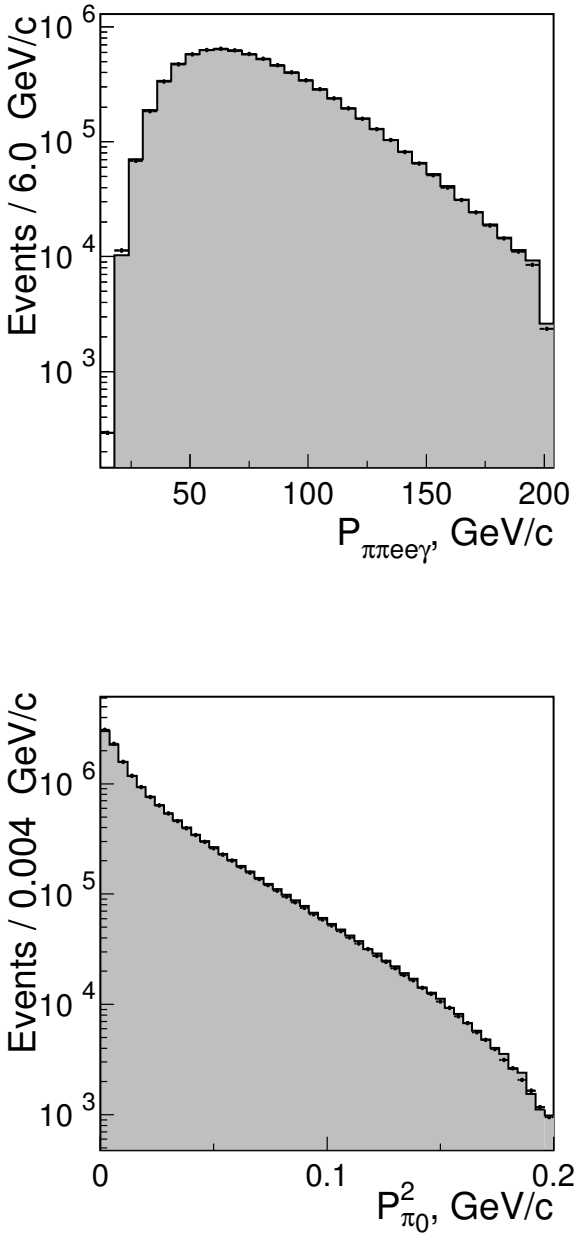

Figure 6.5: Comparison of $P_{\pi\pi ee\gamma}$ and $\left[P_L^2\right]_{\pi^0}$ distributions for $K_L \to \pi^+\pi^-\pi^0_D$ sample. The dots with error bars show data and the filled histogram corresponds to the Monte Carlo simulation. The ordinate has logarithmic scale.

individual contributions to the invariant decay amplitude $K_L \to \pi^+\pi^-\gamma$ (see equations (3.12) to (3.17) and equation (3.24)). And the values of the phase shifts were based on the recent measurements of the K_{e4} decays [32]. The radiative corrections were simulated with PHOTOS package. The simulation procedure allowed to vary the estimated parameters of the invariant amplitude for this decay. The PDG values [1] were used for the rest of the parameters.

The best fit parameters of the model (section 7.1) were used for the final $K_L \to \pi^+\pi^-e^+e^-$ MC samples for acceptance calculation in the measurement of the CP violating asymmetry. The comparison plots for data in Monte Carlo for $K_L \to \pi^+\pi^-e^+e^-$ decays are shown figures 7.6 to 7.8 in chapter 7. Each Monte Carlo sample of these decays used in the analysis section was obtained by processing the Monte Carlo simulated decays with the final analysis program with the selection criteria identical to the ones used for data selection (section 5.3.1). Table 6.2 shows the efficiency in retaining the Monte Carlo signal.

6.5 Estimation of Background Contributions

The $K_L \to \pi^+\pi^-e^+e^-$ data sample contained estimated background of $n = 204 \pm 14$ events (5.4). The major background contribution came from the $K_L \to \pi^+\pi^-\pi^0_D$ decays where π^0 decayed through the Dalitz process $\pi^0 \to e^+e^-\gamma$ and the photon was not detected (87%). The other noticeable backgrounds were contributed by the following processes: $\Xi \to \Lambda\pi^0_D$ decays where $\Lambda \to p\pi^-$ and $\pi^0 \to e^+e^-\gamma$ when proton was misidentified as pion and the photon was not detected (11%); $K_L \to \pi^+\pi^-\pi^0$decays where $\pi^0 \to e^+e^-e^+e^-$and two electrons were not detected (1%); and $K_L \to \pi^+\pi^-\gamma$ decays with the γ converting into the e^+e^- pair in the material of the vacuum window (0.5%). Other possible background sources were considered: $\Xi \to$

Cut	**Meaning**	N	$\varepsilon = \frac{N^{cut}}{N_{\texttt{4TRKGPT}}}$
4TRKGPT	*Trigger-accepted MC events*.	$\mathbf{1,841,010}$	$\mathbf{1.000}$
T3TRAK	Reconstruct particle tracks.	$\mathbf{1,840,860}$	$\mathbf{9.999 \times 10^{-1}}$
KTCLUS	Reconstruct energy clusters.	$\mathbf{1,840,860}$	$\mathbf{9.999 \times 10^{-1}}$
COMBIN	Reject high multiplicity events.	$\mathbf{1,833,410}$	$\mathbf{9.996 \times 10^{-1}}$
T3FVTX4	Reconstruct 4-track vertex.	$\mathbf{1,387,340}$	$\mathbf{7.537 \times 10^{-1}}$
NTRK	Require 4 tracks.	$\mathbf{1,372,800}$	$\mathbf{7.457 \times 10^{-1}}$
TWOPAIR	Require 2 π's and 2 e's.	$\mathbf{991,234}$	$\mathbf{5.384 \times 10^{-1}}$
PMPM	Require $\pi^+\pi^-e^+e^-$.	$\mathbf{985,735}$	$\mathbf{5.354 \times 10^{-1}}$
RPOKIN	Remove resolution effects.	$\mathbf{885,724}$	$\mathbf{4.811 \times 10^{-1}}$
MEE	Suppress $K_L \to \pi^+\pi^-\gamma$ decays.	$\mathbf{752,664}$	$\mathbf{4.088 \times 10^{-1}}$
MEEG	Constrain π^0 mass region.	$\mathbf{752,664}$	$\mathbf{4.088 \times 10^{-1}}$
TRIG	Verify trigger requirements.	$\mathbf{623,688}$	$\mathbf{3.388 \times 10^{-1}}$
VTXCHI	Require good vertex quality.	$\mathbf{602,771}$	$\mathbf{3.274 \times 10^{-1}}$
ZVTX	Constrain vertex z-position.	$\mathbf{588,071}$	$\mathbf{3.194 \times 10^{-1}}$
TPT2TWO	Momentum conservation.	$\mathbf{478,982}$	$\mathbf{2.602 \times 10^{-1}}$
EG	Photon minimum energy.	$\mathbf{478,982}$	$\mathbf{2.602 \times 10^{-1}}$
EKAON	Constrain kaon energy range.	$\mathbf{477,605}$	$\mathbf{2.594 \times 10^{-1}}$
MAGOFF	Match tracks in the magnet.	$\mathbf{461,012}$	$\mathbf{2.504 \times 10^{-1}}$
TEOP	Tighten particle ID for e's.	$\mathbf{436,878}$	$\mathbf{2.373 \times 10^{-1}}$
HCLUS	Require hardware clusters for e's.	$\mathbf{433,156}$	$\mathbf{2.353 \times 10^{-1}}$
MKAON	Constrain kaon mass region.	$\mathbf{416,041}$	$\mathbf{2.226 \times 10^{-1}}$

Table 6.2: Summary of cuts for the selection of $K_L \to \pi^+\pi^-e^+e^-$ Monte Carlo sample. The meaning of each cut is explained in more detail in section 6.4. N is the number of the MC events accepted by the 4-track trigger and the ratio ε is calculated with respect to that number. Compare the statistics to the table 5.2.

$\Lambda\pi^0$ and $K_L \to \pi^+\pi^-\pi^0$ decays with $\pi^0 \to e^+e^-$; just $K_L \to \pi^+\pi^-\pi^0$ decays; overlapping $K_L \to \pi^\pm e^\mp \nu$ decays. Their contribution was found to be negligible.

All these decays were simulated using KTeV Monte Carlo according to the same procedure used for the $K_L \to \pi^+\pi^-e^+e^-$ and $K_L \to \pi^+\pi^-\pi^0_D$ generation. The 4-track trigger requirements (section 4.3) were applied for the generated events. The result of the simulation for each background source was processed by the main analysis program to estimate the contribution to the overall background level (section 5.3.2). Figure 6.6 shows overlaid mass distribution for each contibution and their sum.

The number of events which passed the signal selection criteria for each background source was scaled according to the branching ratio of each decay mode. It was assumed that there were 500 kaon decays for each cascade decay [41]. The acceptance was calculated with the Monte Carlo simulation and the decays $K_L \to \pi^+\pi^-\pi^0_D$ were used as the normalization sample.

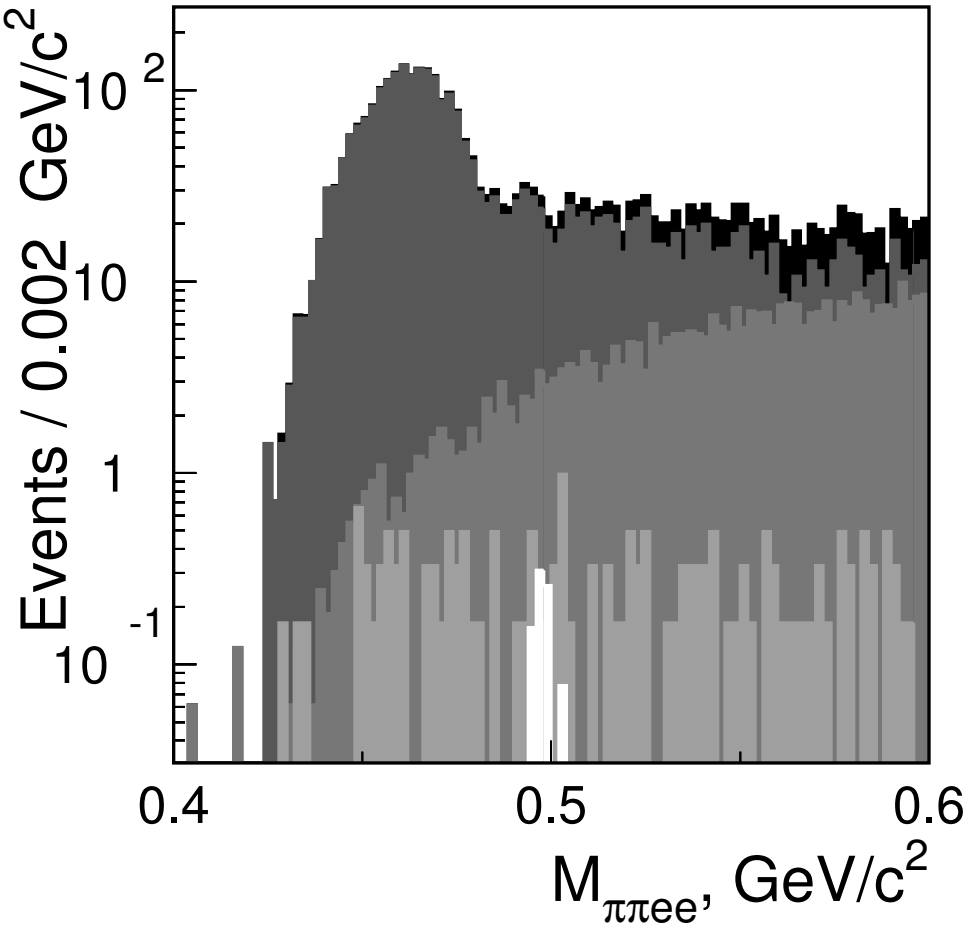

Figure 6.6: $K_L \to \pi^+\pi^-e^+e^-$ background composition. The following contributions are shown: sum of all contributions (black); $K_L \to \pi^+\pi^-\pi^0$, $\pi^0 \to e^+e^-\gamma$ with missing γ (dark gray); $\Xi \to \Lambda\pi^0$ where $\Lambda \to p\pi^-$ and $\pi^0 \to e^+e^-\gamma$ with misidentified p and missing γ (medium gray); $K_L \to \pi^+\pi^-\pi^0$ where $\pi^0 \to e^+e^-e^+e^-$ and two electrons are missing (light gray); $K_L \to \pi^+\pi^-\gamma$ where $\gamma \to e^+e^-$ in the material of the vacuum window (white).

Chapter 7

The Measurements

The details of all the thesis measurements are discussed in this chapter. The $K_L \to \pi^+\pi^-e^+e^-$ data sample, selected according to the procedure described in chapter 5, was analyzed to extract the *parameters of the phenomenological model*, introduced in chapter 3, and to measure CP-violating decay-plane asymmetry, described in section 3.3. This analysis was performed in two stages. First, the best values of the model parameters were estimated by fitting the data to the Monte Carlo simulation (see chapter 6) based on that model. The fit was done using the the *method of maximum likelihood* (ML) as explained in section 7.1. The best values of the the parameters were then used in the Monte Carlo simulation to calculate the acceptance of the KTeV detector in order to perform the *asymmetry measurement* as described in section 7.2. A number of *other* interesting measurements was performed during the analysis. The results of *all* the measurements described in this chapter are summarized and discussed in chapter 8.

7.1 Estimation of The Model Parameters

The parameters of the model were estimated from the $K_L \to \pi^+\pi^-e^+e^-$ data using the *method of maximum likelihood* (ML). Theoretically this is the most important method for parameter estimation. The main ideas and concepts are out-

lined below, and then the method is applied to the problem at hand. The general discussion and details of the ML method can be found elsewhere, e.g. see section 31.1.2. in [1] and references therein.

Suppose that a set of N independently measured physical quantities x_i is described by a hypothetical *probability distribution function* $p(x, \alpha, \beta)$, where α is a set of parameters with unknown values and parameters β are assumed to be known. The mathematical foundation of the method is the fact [57] that the *best estimation* of the parameters α is given by the values which correspond to maximum of the *likelihood function* (LF)

$$\mathcal{L}(\alpha) = \prod_{i=1}^{N} p(x_i, \alpha, \beta) \ , \tag{7.1}$$

where, after the substitution of the measured values x_i and all the known parameters β, the function depends only on parameters α. The product runs over each individual measurement and thus the precise technical term for this particular method is the *unbinned* method of maximum likelihood. The idea of the method is to find the α, which corresponds to maximum of the function $\mathcal{L}(\alpha)$.

This section describes how this method was implemented in the analysis of $K_L \to \pi^+\pi^-e^+e^-$ data. The likelihood function used in this analysis is described in section 7.1.1, where the re-weighting technique is explained as well. The Monte Carlo used in the estimation procedure is discussed in section 7.1.2. The results of the data fits are given in section 7.1.3. The statistical uncertainties on the parameters were calculated using the Monte Carlo simulation as described in the section 7.1.4, where various fit characteristics are discussed as well. The analysis of systematic uncertainties is presented in Section 7.1.5. The estimation of the upper limit on $\frac{|g_{E1}|}{|g_{M1}|}$ is discussed in section 7.1.6. The results of the fits are used in the section 7.1.7 to calculate the mean square charge radius of K^0 and the average $\langle |g_{M1}| \rangle_{E^\star_\gamma}$ introduced in section 3.2.

7.1.1 The Likelihood Function

The role of the measurement x was played in this case by the set of independent variables introduced in chapter 3 and used to parameterize the phase space of the decay $K_L \to \pi^+\pi^- e^+ e^-$:

$$x_i \equiv (\phi, cos\theta_e, cos\theta_\pi, M_{ee}, M_{\pi\pi}) \tag{7.2}$$

These five variables are measured for each event i in the $K_L \to \pi^+\pi^- e^+ e^-$ data sample and the total number of events is $N = 5241$ (which includes a small background contamination (see equation (5.4)) discussed in the section 5.3.2; the effect of the background on the fit results will be discussed in section 7.1.5).

The probability of obtaining each particular measurement x_i is then proportional to the product of the following probabilities: (*i*) the probability of the $K_L \to \pi^+\pi^- e^+ e^-$ decay to take place in a given configuration in the phase space; (*ii*) the probability that the decay occurs within the detector decay volume; (*iii*) the probability that the event satisfies the trigger; (*iv*) and the probability that this event will be successfully reconstructed and will make it through all the selection cuts. The first probability in this chain is given by the partial decay width μ (3.35) and the rest of them are combined in an *overall acceptance* a. The hypothesized data probability distribution function (p.d.f.) p in the equation (7.1) can be written in terms of μ and a. The fact that only the *position* of the maximum of the LF is desired, means that any multiplicative factors independent of α can be ignored in the expression for the function. However, it is important to make sure that the p.d.f. p is properly normalized (since the normalization depends on the parameter α)

$$\int p\,(x, \alpha, \beta)\, dx = 1 \tag{7.3}$$

where the integration is performed over the allowed phase-space region of the variable x. The p was chosen as p.d.f for the data *after all cuts* and can be written

as follows (introducing function $\boldsymbol{f} = \boldsymbol{\mu} \cdot \boldsymbol{a}$ for convenience):

$$\boldsymbol{p}\left(\boldsymbol{x}, \boldsymbol{\alpha}, \boldsymbol{\beta}\right) = \frac{\boldsymbol{f}}{\int \boldsymbol{f} \boldsymbol{dy}} = \frac{\boldsymbol{\mu}\left(\boldsymbol{x}, \boldsymbol{\alpha}, \boldsymbol{\beta}\right) \cdot \boldsymbol{a}\left(\boldsymbol{x}\right)}{\int \boldsymbol{\mu}\left(\boldsymbol{y}, \boldsymbol{\alpha}, \boldsymbol{\beta}\right) \cdot \boldsymbol{a}\left(\boldsymbol{y}\right) \boldsymbol{dy}} \tag{7.4}$$

The integration is performed over the kinematically allowed phase-space region of the variable $\boldsymbol{x}$, and $\boldsymbol{y}$ is just a dummy integration variable. The $\boldsymbol{\alpha}$ in this case denotes the *set* of model parameters to be estimated:

$$\boldsymbol{\alpha} \equiv \left(\left|\boldsymbol{g_{CR}}\right|, \frac{\left|\boldsymbol{g_{E1}}\right|}{\left|\boldsymbol{g_{M1}}\right|}, \frac{\boldsymbol{a_1}}{\boldsymbol{a_2}}, \tilde{\boldsymbol{g}}_{\boldsymbol{M1}} \right) \tag{7.5}$$

which were defined in section 3.2. The rest of the parameters of the model are treated as known and are denoted by $\boldsymbol{\beta}$:

$$\boldsymbol{\beta} \equiv \left(\boldsymbol{\eta_{+-}}, \boldsymbol{\phi_{+-}}, \boldsymbol{\delta_0^0}\left(\boldsymbol{M_{\pi\pi}}\right), \boldsymbol{\delta_1^1}\left(\boldsymbol{M_{\pi\pi}}\right) \right) \ , \tag{7.6}$$

where $\boldsymbol{\delta_0^0}\left(\boldsymbol{M_{\pi\pi}}\right)$ and $\boldsymbol{\delta_1^1}\left(\boldsymbol{M_{\pi\pi}}\right)$ stand for the parameterization of these strong interaction phase shifts (see section 3.2). The normalization integral $\int \boldsymbol{f} \boldsymbol{dx}$ in the denominator must be calculated for each $\boldsymbol{\alpha}$, a formidable task since the acceptance $\boldsymbol{a}$ must be estimated each time the value of $\boldsymbol{\alpha}$ is floated in the fit. To avoid this the *re-weighting technique* was used, which relied on the Monte Carlo integration method [62] to calculate the integral.

The *idea* of the re-weighting technique was as follows. The KTeV Monte Carlo (chapter 6), was used to generate a large sample of events with a given choice of $\boldsymbol{\alpha} = \boldsymbol{\alpha_0}$ (and PDG values of $\boldsymbol{\beta}$) parameters. This MC sample was then re-weighted[1], to simulate a sample which would be generated with a different $\boldsymbol{\alpha}$, and compared to the data to find the optimal agreement (corresponding to the best fit, i.e. the value of $\boldsymbol{\alpha}$ maximizing the LF).

The rest of this section deals with the deriviation of the expression for the likelihood function (7.20), which lead to the re-weighting technique. According

[1]And therefore this MC sample was referred to as *re-weighting Monte Carlo sample*.

to the Monte Carlo integration method (the uncertainty of this approximation is given by equation (7.13) below)

$$\int_V f dx \approx V \langle f \rangle \tag{7.7}$$

where the average

$$\langle f \rangle \equiv \frac{1}{N} \sum_{i=1}^{N} f_i \tag{7.8}$$

and N is the number of randomly generated events *uniformly* distributed over the phase-space volume V. And $f_i \equiv f(x_i)$ is value of the function f for *event* i in phase-space point x_i.

A large number of $K_L \rightarrow \pi^+\pi^-e^+e^-$ Monte Carlo events was generated with certain value $\alpha = \alpha_0$. The function $f(x_j, \alpha_0)$ (7.4) is the distribution of these Monte Carlo events after all cuts and, in this case, is *not uniform* ($j = 1, \ldots, N_{MC}$, where N_{MC} is the total number of Monte Carlo events after all cuts). To use these values for the integration they are *"made uniform"* by weighting each event j, surviving the cuts, with the inverse weight $\frac{1}{f(x_j, \alpha_0)}$. Then the average in (7.7) can be calculated as

$$\langle f \rangle_{N_{MC}} = \frac{\sum_{j=1}^{N_{MC}} \frac{f(x_j, \alpha)}{f(x_j, \alpha_0)}}{\sum_{j=1}^{N_{MC}} \frac{1}{f(x_j, \alpha)}} \tag{7.9}$$

and using the fact that

$$\sum_{j=1}^{N_{MC}} \frac{f(x_j, \alpha)}{f(x_j, \alpha_0)} = \sum_{j=1}^{N_{MC}} \frac{\mu(x_j, \alpha)\, a(x_j)}{\mu(x_j, \alpha_0)\, a(x_j)} = \sum_{j=1}^{N_{MC}} \frac{\mu(x_j, \alpha)}{\mu(x_j, \alpha_0)} \tag{7.10}$$

the normalization integral can be written as

$$\int_V f(x, \alpha)\, dx \approx \frac{V \sum_{j=1}^{N_{MC}} \frac{\mu(x_j, \alpha)}{\mu(x_j, \alpha_0)}}{\sum_{j=1}^{N_{MC}} \frac{1}{\mu(x_j, \alpha_0)\, a(x_j)}} \,. \tag{7.11}$$

The probability then becomes

$$p(x_i,\alpha) = \frac{f(x_i,\alpha)}{\int\limits_V f(x,\alpha)\,dx} \approx \frac{\mu(x_i,\alpha)\,a(x_i)}{V\sum\limits_{j=1}^{N_{MC}}\frac{\mu(x_j,\alpha)}{\mu(x_j,\alpha_0)}} \Big/ \sum_{j=1}^{N_{MC}}\frac{1}{\mu(x_j,\alpha_0)\,a(x_j)}$$

$$= \frac{\mu(x_i,\alpha)\,a(x_i)\sum\limits_{j=1}^{N_{MC}}\frac{1}{\mu(x_j,\alpha_0)\,a(x_j)}}{V\sum\limits_{j=1}^{N_{MC}}\frac{\mu(x_j,\alpha)}{\mu(x_j,\alpha_0)}} \tag{7.12}$$

This is the expression for the p.d.f. p to be used in the likelihood function (7.1). It is an *approximation*. The uncertainty of the normalization integral (7.7) is given by the formula [62]

$$\pm V\sqrt{\frac{\langle f^2\rangle - \langle f\rangle^2}{N}} \tag{7.13}$$

and is only due to the finite number of the Monte Carlo simulated events and therefore can be made sufficiently small. The expression (7.12) would give the accurate probability for any value of α as long as enough MC events N_{MC} were generated to sample the kinematically allowed region of the phase-space points x (7.2) with satisfactory precision.

In general, the value of the likelihood function (7.1) can be very small if the number of measurements N is large, since each $p(x,\alpha,\beta)$ has values from zero to less than one. For actual calculations it is usually convenient to replace a product of small numbers with a sum of logarithms of the small numbers and thus to work with the *logarithm* of LF, which, of course, has the same maximum as the function itself. Using the expression for p.d.f. p (7.12) the logarithm of the LF (7.1) becomes

$$log\mathcal{L}(\alpha) = log\prod_{i=1}^{N} p(x_i,\alpha) = \sum_{i=1}^{N} log\,p(x_i,\alpha)$$

$$\begin{aligned}
&\approx \sum_{i=1}^{N} log\, \mu\left(x_i, \alpha\right) + \sum_{i=1}^{N} log\, a\left(x_i\right) + \\
&+ \sum_{i=1}^{N} log \sum_{j=1}^{N_{MC}} \frac{1}{\mu\left(x_j, \alpha_0\right) a\left(x_j\right)} - \sum_{i=1}^{N} log\, V - \\
&- \sum_{i=1}^{N} log \sum_{j=1}^{N_{MC}} \frac{\mu\left(x_j, \alpha\right)}{\mu\left(x_j, \alpha_0\right)} \\
&= \sum_{i=1}^{N} log\, \mu\left(x_i, \alpha\right) - N \cdot log \sum_{j=1}^{N_{MC}} \frac{\mu\left(x_j, \alpha\right)}{\mu\left(x_j, \alpha_0\right)} + \\
&+ g\left(X, X_{MC}, \alpha_0\right) \ , \qquad (7.14)
\end{aligned}$$

where N is the number of $K_L \rightarrow \pi^+\pi^- e^+ e^-$ events and function g depends on data and Monte Carlo sample, but not on α and thus can be ignored in the calculation of the LF:

$$\begin{aligned}
g\left(X, X_{MC}, \alpha_0\right) \ &\equiv \ \sum_{i=1}^{N} log\, a\left(x_i\right) + \\
&+ N \left[log \sum_{j=1}^{N_{MC}} \frac{1}{\mu\left(x_j, \alpha_0\right) a\left(x_j\right)} - log\, V \right] \qquad (7.15)
\end{aligned}$$

Thus, the likelihood function for different values of α can be obtained by *re-weighting* the events from one sufficiently large Monte Carlo simulated sample, which was generated with $\alpha = \alpha_0$

$$log \mathcal{L}\left(\alpha\right) = \sum_{i=1}^{N} log\, \mu\left(x_i, \alpha\right) - N \cdot log \sum_{j=1}^{N_{MC}} \frac{\mu\left(x_j, \alpha\right)}{\mu\left(x_j, \alpha_0\right)} \qquad (7.16)$$

This expression for the logarithm of the likelihood function can result in ever larger negative numbers as the number of the Monte Carlo events in the re-weighting sample N_{MC} increases. To avoid computation of the unnecessary large numbers, one more term was added to this expression[2]:

$$log \mathcal{L}\left(\alpha\right) = \sum_{i=1}^{N} log\, \mu\left(x_i, \alpha\right) - N \cdot log \sum_{j=1}^{N_{MC}} \frac{\mu\left(x_j, \alpha\right)}{\mu\left(x_j, \alpha_0\right)} + N \cdot log N_{MC} \qquad (7.17)$$

[2]This useful expression was kindly provided by Alexander Ledovskoy [65]. The derivation given here is my own, AG.

This last added term does not depend on α and therefore has no effect on the position of the maximum, but only affects the value of the function at that point.

Finally, due to the difference in the experimental conditions between $'97$ and $'99$ (chapter 4), the likelihoods for these two periods had to be considered separately. In this case the logarithm of the overall likelihood function is simply the sum of the logarithms of the functions corresponding to each period.

$$\mathcal{L}(\alpha) = \prod_{i=1}^{N} p_i = \prod_{i=1}^{N^{97}} p_i \cdot \prod_{j=1}^{N^{99}} p_j = \mathcal{L}^{97} \cdot \mathcal{L}^{99} \tag{7.18}$$

and

$$log\mathcal{L}(\alpha) = log\mathcal{L}^{97} + log\mathcal{L}^{99} \tag{7.19}$$

And the *final expression* for the logarithm of the likelihood function becomes:

$$\begin{aligned} log\mathcal{L}(\alpha) &= \sum_{i=1}^{N^{97}} log\,\mu(x_i,\alpha) - N^{97} \cdot log \sum_{j=1}^{N_{MC}^{97}} \frac{\mu(x_j,\alpha)}{\mu(x_j,\alpha_0)} + \\ &\quad + \sum_{k=1}^{N^{99}} log\,\mu(x_k,\alpha) - N^{99} \cdot log \sum_{m=1}^{N_{MC}^{99}} \frac{\mu(x_m,\alpha)}{\mu(x_m,\alpha_0)} + \\ &\quad + N^{97} \cdot logN_{MC}^{97} + N^{99} \cdot logN_{MC}^{99} \\ &= log\mathcal{L}(X, X_{MC}, \alpha_0, \beta, \alpha) \\ &\equiv \lambda(\alpha)\ , \end{aligned} \tag{7.20}$$

where N^{97} and N^{99} are the numbers of data events in $'97$ and $'99$, correspondingly

$$N = N^{97} + N^{99} = 2012 + 3229 = 5241 \tag{7.21}$$

and N is the size of the data sample

$$X \equiv \{x_i\}\,, \quad i = 1, \ldots, N \tag{7.22}$$

with x_i, α and β defined by (7.2), (7.5) and (7.6), respectively. The size N_{MC} of the re-weighting Monte Carlo sample X_{MC} and it's values α_0 will be determined

in the section 7.1.2. The effect of the background (5.4) present in the sample of $\mathbf{5241}$ $\boldsymbol{K_L \to \pi^+\pi^-e^+e^-}$ decay candidates will be discussed in the section 7.1.5.

In conclusion, it is important to note that the derivation of the likelihood function (7.20) was done without any specific assumptions about the decay at hand. This is a **general expression**, which can be used in an analysis of *any data set* $\boldsymbol{X}$ of *any decays* (specified by $\boldsymbol{\mu, \alpha, \beta}$) from *any experiment* with Monte Carlo simulated sample $\boldsymbol{X_{MC}}$.

7.1.2 The Re-weighting Monte Carlo Sample

The size of the re-weighting Monte Carlo sample $\boldsymbol{N_{MC}}$ used in the likelihood function $\boldsymbol{\lambda}$ (7.20) had to be chosen as a compromise between sufficient population of the decay phase-space in order to reduce the uncertainty in the p.d.f. normalization (7.12) and reasonable computing time for the maximization procedure. To decide on the size $\boldsymbol{N_{MC}}$, 1025 statistically independent Monte Carlo samples were generated for a given values of parameter set $\boldsymbol{\alpha_0}$. Each sample was approximately the size of the data (7.21). One of these MC samples was treated as data and the other 1024 samples were grouped to form various re-weighting samples of different size. The fits were performed with the re-weighting MC constructed using 16, 32, 64, 128, 256 and 512 Monte Carlo samples at a time with the total number of 64, 32, 16, 8, 4, and 2 times, respectively. The result of the fits are shown in the figure 7.1. The statistical fluctuations of the fit outcomes first decrease significantly with the size of the re-weighting Monte Carlo sample, but after approximately $\boldsymbol{N_{MC} = 500,000}$ the size does not matter so much. From this study the re-weighting Monte Carlo sample size was chosen to be at least

$$\boldsymbol{N_{MC} = 128 \cdot N \approx 645 \cdot 10^3} \tag{7.23}$$

events.

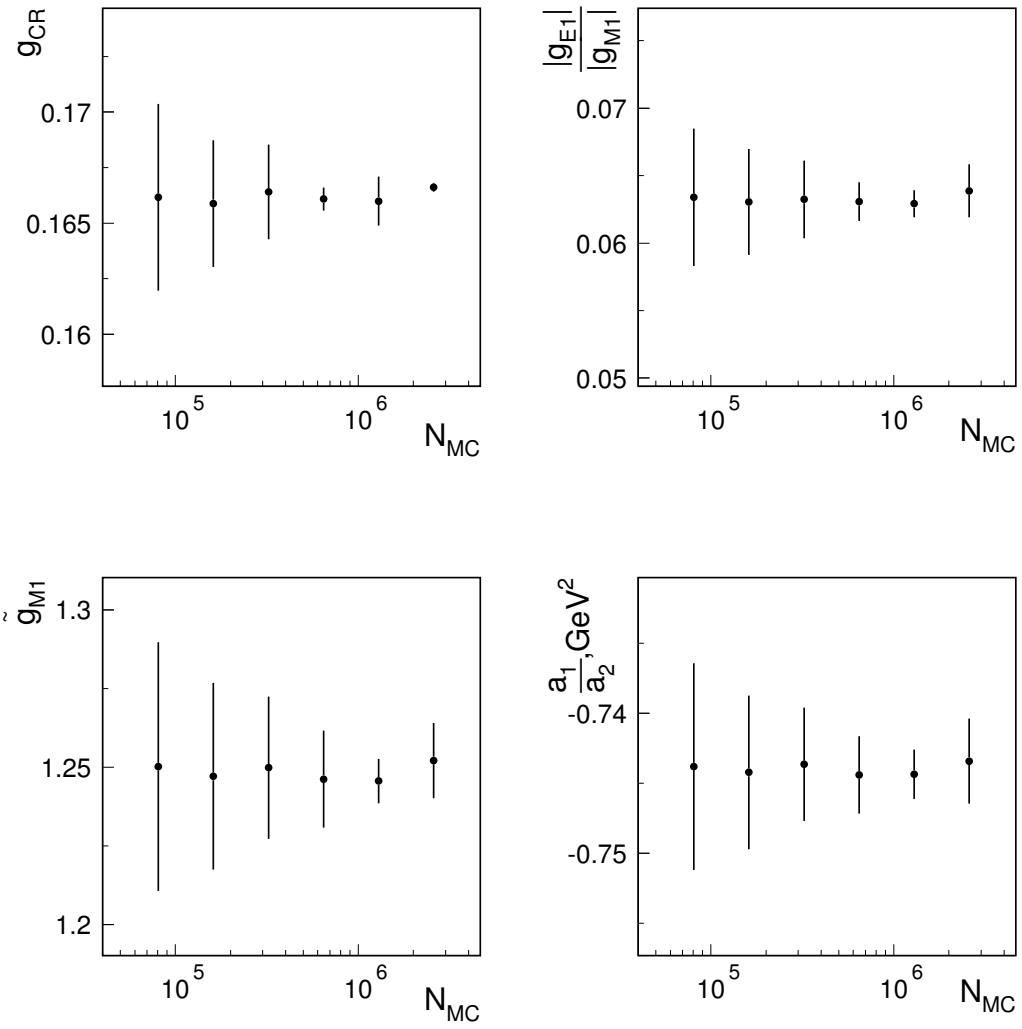

Figure 7.1: The statistical uncertainty in the fit results due to the finite size of the re-weighting Monte Carlo sample size.

To check that this number of Monte Carlo simulated events in the re-weighting sample indeed sufficiently populates the phase-space for the re-weighting to work five statistically independent Monte Carlo samples of size N_{MC} were generated with quite distinct values of α (7.5):

$$\begin{aligned}
\boldsymbol{\alpha_0^{-2}} &= (\mathbf{0.09, 0.0, -0.81, 0.8}) \\
\boldsymbol{\alpha_0^{-}} &= (\mathbf{0.13, 0.0, -0.77, 1.0}) \\
\boldsymbol{\alpha_0} &= (\mathbf{0.16, 0.0, -0.73, 1.2}) \\
\boldsymbol{\alpha_0^{+}} &= (\mathbf{0.20, 0.06, -0.69, 1.4}) \\
\boldsymbol{\alpha_0^{+2}} &= (\mathbf{0.24, 0.09, -0.65, 1.6}) \ . \qquad (7.24)
\end{aligned}$$

The samples generated with parameters other than $\boldsymbol{\alpha_0}$ were then re-weighted to make them look like they were generated with parameter $\boldsymbol{\alpha^0}$ and checked to see how the distributions of five independent variables (7.2) were affected. The re-weighting worked as expected. Figures 7.2 and 7.3 illustrate how the re-weighting affects the distributions of Monte Carlo events generated with different values of $\boldsymbol{\alpha}$.

For the final *fits with data* the following values for the parameters for the re-weighting Monte Carlo sample were chosen

$$\boldsymbol{\alpha_0} = (\mathbf{0.163, 0.0001, -0.745, 1.11}) \qquad (7.25)$$

The fit results did not depend on the values of the input paramters and this choice represented the results of the fits with data. Using these initial values simply reduced the computing time requred to find the maximum of the likelihood function. The size of the sample was

$$\boldsymbol{N_{MC} = 256 \cdot N \approx 1.3 \cdot 10^6} \qquad (7.26)$$

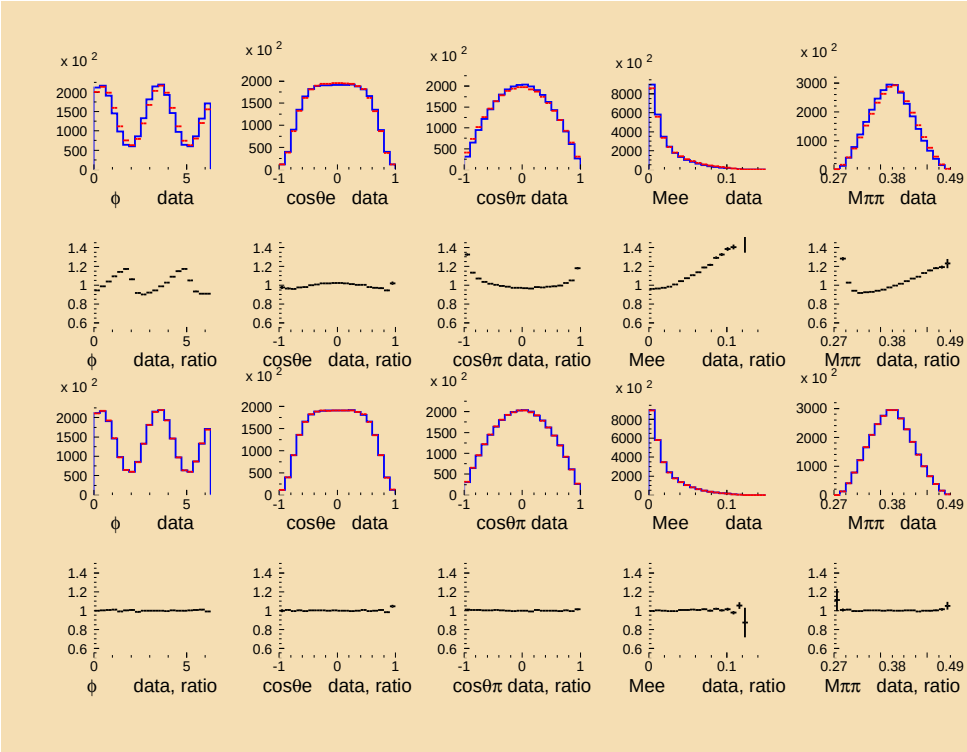

Figure 7.2: The re-weighting technique worked as expected. Two samples were generated with values α_0 and α_0^{-2} (7.24). The values of α_0^{-2} are significantly *smaller* than values of α. The first row of plots shows the overlays of the distributions for the five variables. The second row shows the ratio of the plots above and illustrates how different they look. The third row shows the overlays of distributions after the α_0^{-2} Monte Carlo was re-weighted to look like α_0. The two look identical as demonstrated by the ratios shown in the forth row of plots.

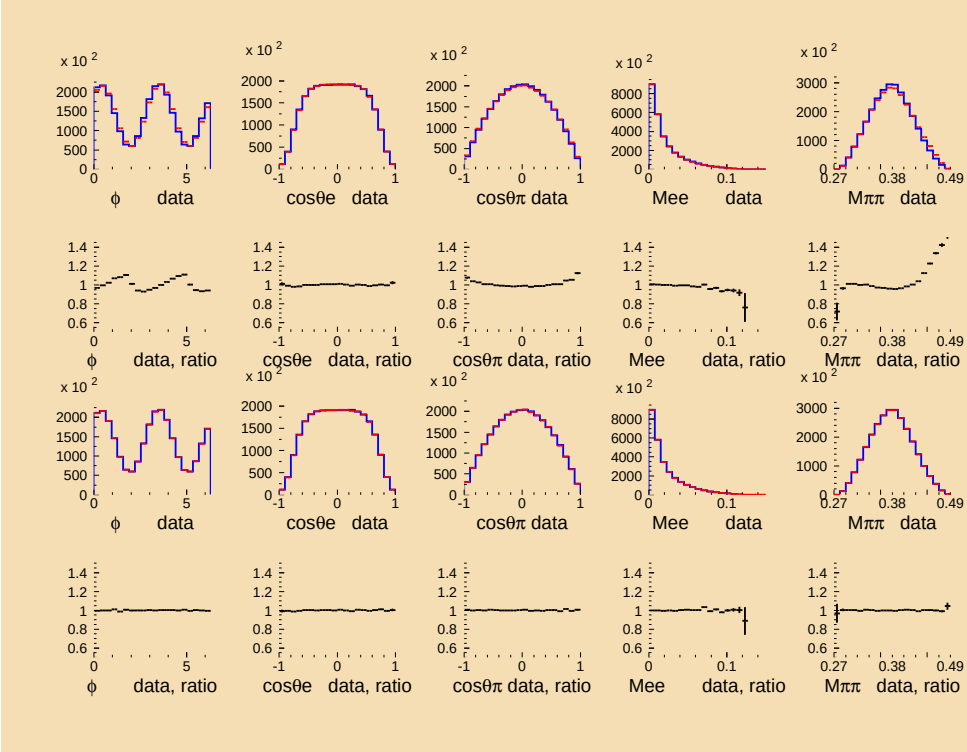

Figure 7.3: The re-weighting of re-weighting Monte Carlo samples worked as expected. Two samples were generated with values $\boldsymbol{\alpha_0}$ and $\boldsymbol{\alpha_0^{+2}}$ (7.24). The values of $\boldsymbol{\alpha_0^{-2}}$ are significantly *larger* than values of $\boldsymbol{\alpha}$. The first row of plots show the overlays of the distributions for the five variables. The second row shows the ratio of the plots above and illustrates how different they look. The third row shows the overlays of distributions after the $\boldsymbol{\alpha_0^{+2}}$ Monte Carlo was re-weighted to look like $\boldsymbol{\alpha_0}$. The two look identical as demonstrated by the ratios shown in the forth row of plots.

events, i.e. twice the amount given by equation (7.23). The fractions of events from $'97$ and $'99$ were chosen according to the ratio in data, see equation (7.21).

7.1.3 The Data Fitting

The best fit between the $K_L \to \pi^+\pi^- e^+ e^-$ data and the Monte Carlo simulation based on the phenomenological model corresponds to the maximum of the likelihood function (7.20) with respect to the parameters α (7.5). To calculate this function the set of reconstructed variables x (7.2) for each event in both data and Monte Carlo samples was used to calculate the partial matrix element μ (3.35) for each choice of α. The Powell's algorithm [62] gradient search was used to find the maximum by allowing α to float. As an alternative, the *MINUIT* program [56], [63] was used. The results of the fits did not depend on the procedure used. The maximization of the likelihood function with respect to α yielded the best estimates for these parameters $\hat{\alpha}$ as summarized in the table 7.1. The statistical uncertainties $\sigma(\hat{\alpha})$ were calculated from Monte Carlo as explained in the section 7.1.4. The correlations and goodness-of-fit are discussed there as well.

parameter α	*estimated value* $\hat{\alpha}$	*statistical uncertainty* $\sigma(\hat{\alpha})$
$\lvert g_{CR}\rvert$	0.163	0.014
$\frac{\lvert g_{E1}\rvert}{\lvert g_{M1}\rvert}$	0.0001	0.024
$\tilde{g}_{M1}$	1.11	0.12
a1/a2	-0.744	0.027

Table 7.1: The best fit parameter values $\hat{\alpha}$ estimated from the data.

7.1.4 The Fit Studies with MC Simulated Experiments

After obtaining the final results for the estimated parameters, $N_{fits} = 512$ statistically independent Monte Carlo simulated experiments[3] were generated with the same number of events as in data (7.21) and the values of $\alpha^0 = \alpha_{max}$ from the table 7.1. These simulated experiments were then fitted in the same way as data and the results of the fits

$$\hat{\alpha}^i \,, \qquad i = 1, \ldots, N_{fits} \tag{7.27}$$

were used: (*i*) to check for bias in the estimation of the parameters α, (*ii*) to calculate the correlation matrix, (*iii*) the statistical uncertainties and (*iv*) to estimate the goodness-of-fit.

To check for possible *bias* in the estimation of the parameters, the known true values α^0 used in Monte Carlo simulation were compared with the mean values of the results obtained from the simulated fits

$$\overline{\hat{\alpha}_j} = \frac{1}{N_{fits}} \sum_{i=1}^{N_{fits}} \hat{\alpha}_j{}^i \,, \qquad j = 1, 2, 3, 4 \tag{7.28}$$

where the lower index j refers to a specific component of the vector of parameters α (7.5). Table 7.2 shows the biases for different parameters. The bias is present in the case of g_{M1} and $\frac{|g_{E1}|}{|g_{M1}|}$ because the distributions of their fit results appear to be non-Gaussian, see figures see figures 7.4 and 7.9. The other two parameters show virtually no bias. The bias was included as a part of the systematic uncertainty in the table 7.7 (section 7.1.5).

The *correlation matrix* was calculated using the results of the four-parameter fits. The correlation coefficient is defined as

$$\rho_{ij} = \frac{V_{ij}}{\sigma_i \sigma_j} \tag{7.29}$$

[3]Note that these *simulated experiments* are conceptually different and statistically independent from the *re-weighting Monte Carlo* sample described in section 7.1.2, although the same procedure was used to generate both types of the samples.

parameter	*true value*	*mean from the fits*	*bias*
$\lvert g_{CR}\rvert$	0.163	0.165	0.002 +- 0.001
$\frac{\lvert g_{E1}\rvert}{\lvert g_{M1}\rvert}$	0.0001	0.012	0.012 +- 0.001
$\tilde{g}_{M1}$	1.111	1.144	0.033 +- 0.005
a1/a2	-0.744	-0.743	0.001 +- 0.001

Table 7.2: Check for bias with Monte Carlo simulated experiments.

The covariance matrix V_{ij} was estimated directly according to the formula

$$V_{ij} = \frac{1}{N_{fits}} \sum_{k=1}^{N_{fits}} \left(\hat{\alpha_i}^k - \alpha_i^0\right)\left(\hat{\alpha_j}^k - \alpha_j^0\right) , \qquad i,j = 1,2,3,4 \tag{7.30}$$

where the lower index for the α^0 refers to the fit input for particular component (compare to (7.28)) of the vector of parameters α (7.5). The *true values* α^0 were used, rather then mean value $\overline{\hat{\alpha}}$ (7.28), to obtain somewhat better estimate[4] of the covariance matrix V. The correlation coefficients are shown in the table 7.3. One can see that there is strong correlation between parameters $\tilde{g}_{M1}$ and $\frac{a_1}{a_2}$, as can be expected from the equation (8.15).

The *statistical uncertainty* on the estimated parameters was estimated by calculating the variances (V is defined by equation (7.30))

$$\sigma_i^2 = V_{ii} \tag{7.31}$$

for each component i of the vector of parameters α. In general, the statistical uncertainty on the parameters can be evaluated by several different methods (e.g. see chapter 6 in [58]). The Monte Carlo method chosen in this analysis is universal, conceptually simple and allows to increase the accuracy of the variance

[4] Also, for this reason the factor of $\frac{1}{N}$ is used in the equation (7.30) rather than the more familiar $\frac{1}{N-1}$.

$\lvert g_{CR}\rvert$	$\frac{\lvert g_{E1}\rvert}{\lvert g_{M1}\rvert}$	$\tilde{g}_{M1}$	$\frac{a_1}{a_2}$
$\mathbf{1}$	$\mathbf{0.33 \pm 0.04}$	$\mathbf{0.36 \pm 0.04}$	$\mathbf{0.24 \pm 0.04}$
	$\mathbf{1}$	$\mathbf{0.29 \pm 0.04}$	$\mathbf{0.03 \pm 0.04}$
		$\mathbf{1}$	$\mathbf{0.924 \pm 0.007}$
			$\mathbf{1}$

Table 7.3: The matrix of correlation coefficients $\boldsymbol{\rho}$. There is a strong correlation between $\tilde{g}_{M1}$ and $\frac{a_1}{a_2}$. The diagonal elements are exactly unity by definition.

estimation by simply increasing the number of simulated experiments. The results of the fits with simulated experiments produced the *marginal distributions*, i.e. the distributions of each particular $\hat{\alpha}_i$ (e.g. $i = 2$) integrated over all values of the rest of the components $\hat{\alpha_{j \neq i}}$ (i.e. j=1,3,4). The standard deviations (7.31) of these distributions then were used to quantify the statistical uncertainty on the parameters at the 68.3% confidence level (figure 7.4). The values of the uncertainties $\sigma\,(\hat{\alpha})$ are summarized in the table 7.1. The case of $\frac{|g_{E1}|}{|g_{M1}|}$ required special treatment to estimate the *upper limit* on this parameter (section 7.1.6), since the best estimation from the data $\frac{|\hat{g_{E1}}|}{|g_{M1}|}$ was zero and the parameter must be positive definite.

Finally, the *goodness-of-fit* (g.o.f.) was estimated. In general, a *g.o.f. test statistics* t is defined as a function (e.g. χ^2) of the data whose value reflects the agreement between the data and the hypothesized model. The agreement is conventionally quantified by giving the *p-value*, defined as the probability to find t in the region of equal or lesser compatibility with the model than the level of compatibility observed with the actual data (see section 31 in [1]). In other words, it is the probability of obtaining the data at least as incompatible with the model as the actually observed data, assuming that the data is indeed described by the model.

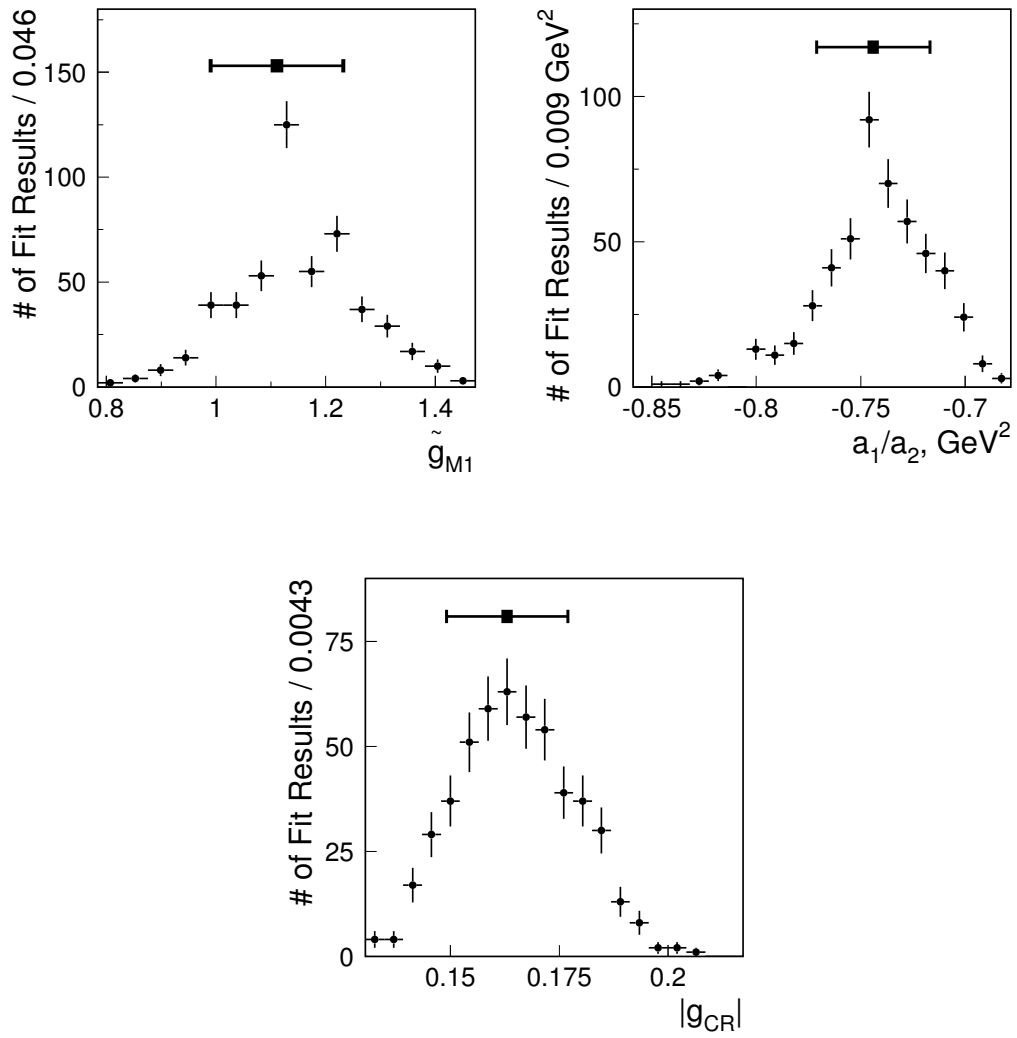

Figure 7.4: Distribution of the fit results for the 512 simulated experiments. The square dots show the results of the data fits and the error bars represent the assigned statistical uncertainties based on the region where 68.3% of the simulated fit results fall.

Presently, there is no standard way to estimate the g.o.f. for an *unbinned* likelihood fit, [60, 59]. The *common practice*, e.g. see section 6.11 in [58], is to use the maximum value of the likelihood function $\boldsymbol{\lambda}$ (7.20) obtained in the fit as the statistics $\boldsymbol{t}$. The idea is to compare the distribution of the values obtained from the simulated fits $\boldsymbol{\lambda}\left(\hat{\boldsymbol{\alpha}^{i}}\right)$, with the value obtained from the fit of the actual data $\boldsymbol{\lambda}\left(\hat{\alpha}\right)$. This comparison allows to calculate the $\boldsymbol{p}$-value. Such a comparison is shown in the figure 7.5. The fit result with the actual data gives the value $\boldsymbol{\lambda}\left(\hat{\alpha}\right) = \mathbf{34,992.801}$, which is close to the most probable value of the distribution and corresponds to the $\boldsymbol{p}$-value of $\mathbf{33\%}$. This supports the hypothesis that the phenomenological model (section 3.2) describes the observed data.

It has been pointed out recently [61] however, that the method described above is not guaranteed to provide useful information about the goodness-of-fit. This issue is a subject of current investigation. Since no standard method exists, the goodness-of-fit was *also estimated* by comparing the agreement of the distributions of independent variables (7.2), for the completely reconstructed data and Monte Carlo simulated events, generated using the best values of the fit parameters. Figures 7.6 to 7.8 show such comparisons for the the five independent variables used in the fit and $\boldsymbol{E^{\star}_{\gamma}}$. In this case the value of the $\boldsymbol{\chi^2}$ per degrees of freedom represents the statistics $\boldsymbol{t}$ for each distribution. Assuming that fluctuations are Gaussian, $\boldsymbol{\chi^2}$ values for each plot can be used to calculate the $\boldsymbol{p}$-values for a given number of degrees of freedom (DOF). The agreement between these distributions is summarized in the table 7.4. These $\boldsymbol{p}$-values are not related to the $\mathbf{33\%}$ in the previous section. They serve as the *independent* indication for the validity of the hypothesis of the model.

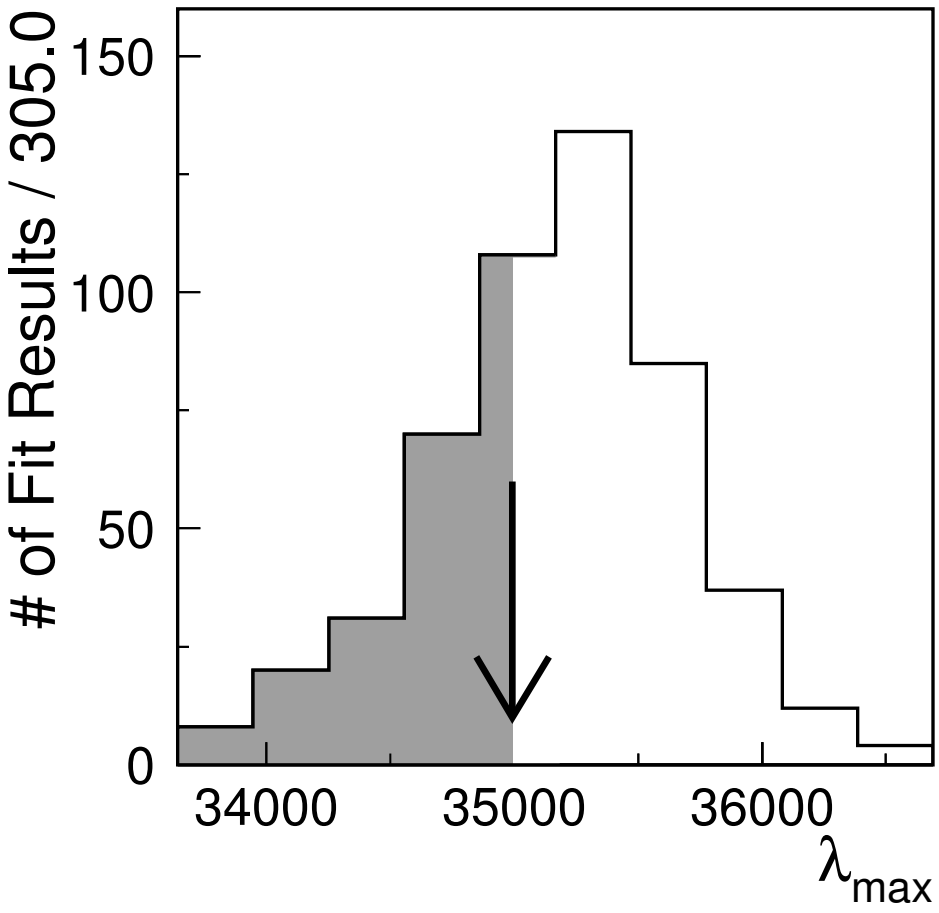

Figure 7.5: Distribution of $\boldsymbol{\lambda}$ (7.20) values at the maximum. The histogram is filled with the results of 512 fits of simulated experiments $\boldsymbol{\lambda}^{\boldsymbol{i}}_{\boldsymbol{max}} = \boldsymbol{\lambda}\left(\hat{\boldsymbol{\alpha}}^{\boldsymbol{i}}\right)$. The arrow points to the value $\boldsymbol{\lambda}\left(\hat{\boldsymbol{\alpha}}\right)$ obtained from the fit of actual data. The shaded area corresponds to the integral resulting in the $\boldsymbol{p}$-value of $\mathbf{33\%}$.

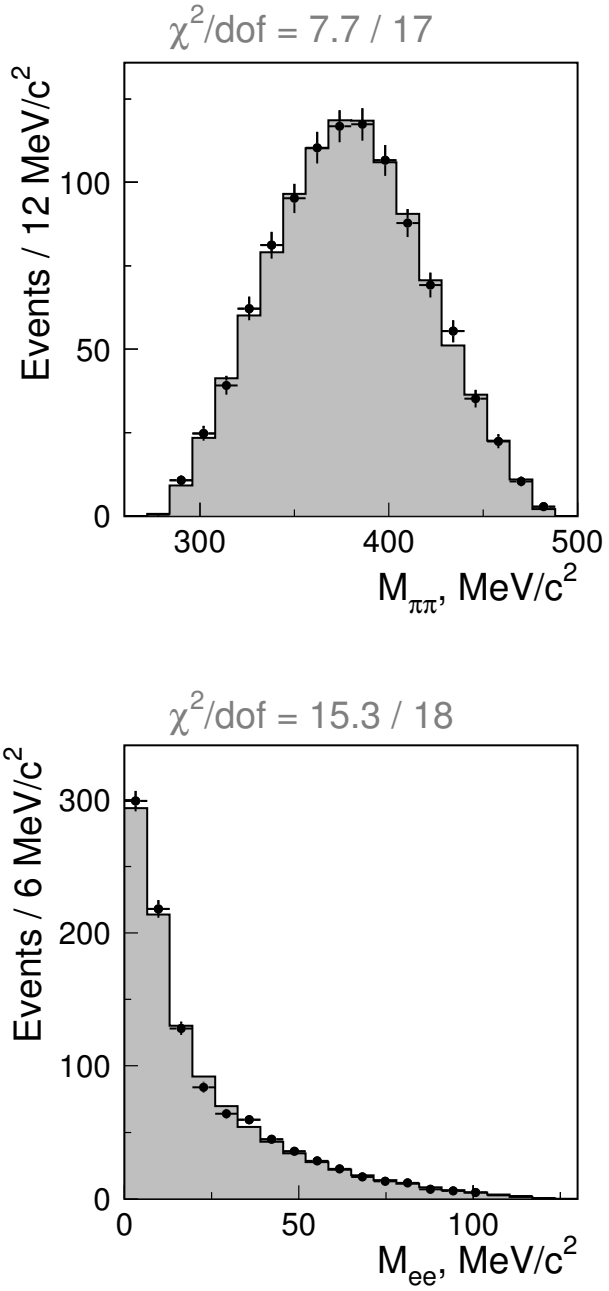

Figure 7.6: Comparison of the invariant mass distributions for $\pi^+\pi^-$ and e^+e^- systems. The dots with error bars show data and the filled histogram corresponds to the Monte Carlo simulation based on the model with parameter values obtained from the maximum likelihood fit.

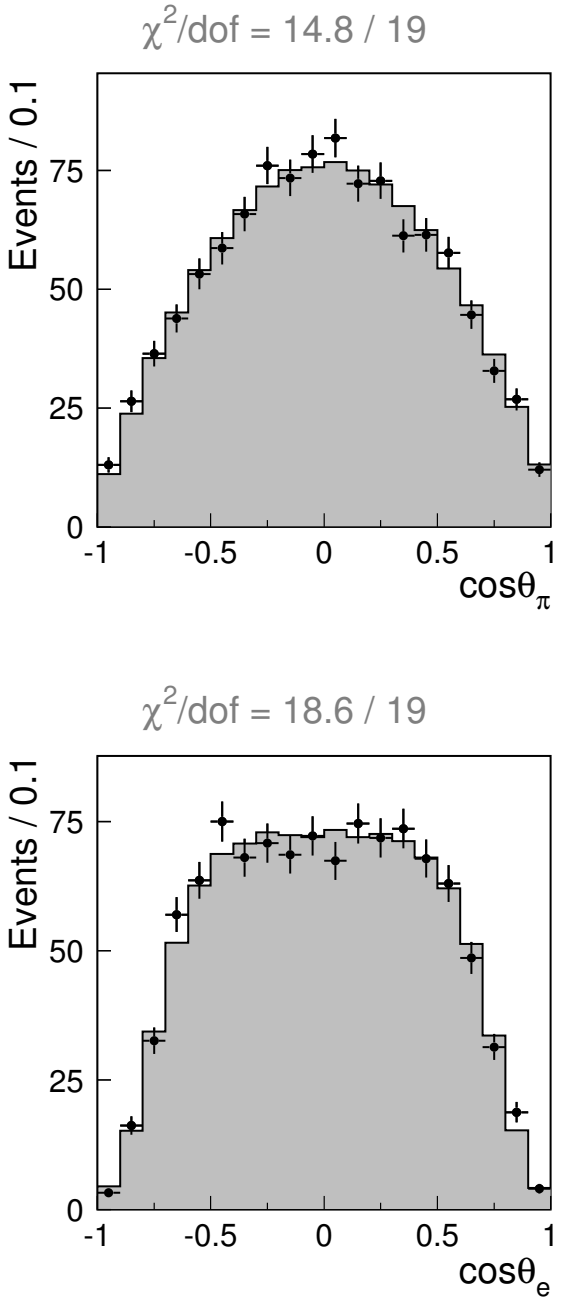

Figure 7.7: Comparison of the $\boldsymbol{cos\theta_\pi}$ and $\boldsymbol{cos\theta_e}$ distributions, see Figure 3.4 for the definition of the angles. The dots with error bars show data and the filled histogram corresponds to the Monte Carlo simulation based on the model with parameter values obtained from the maximum likelihood fit.

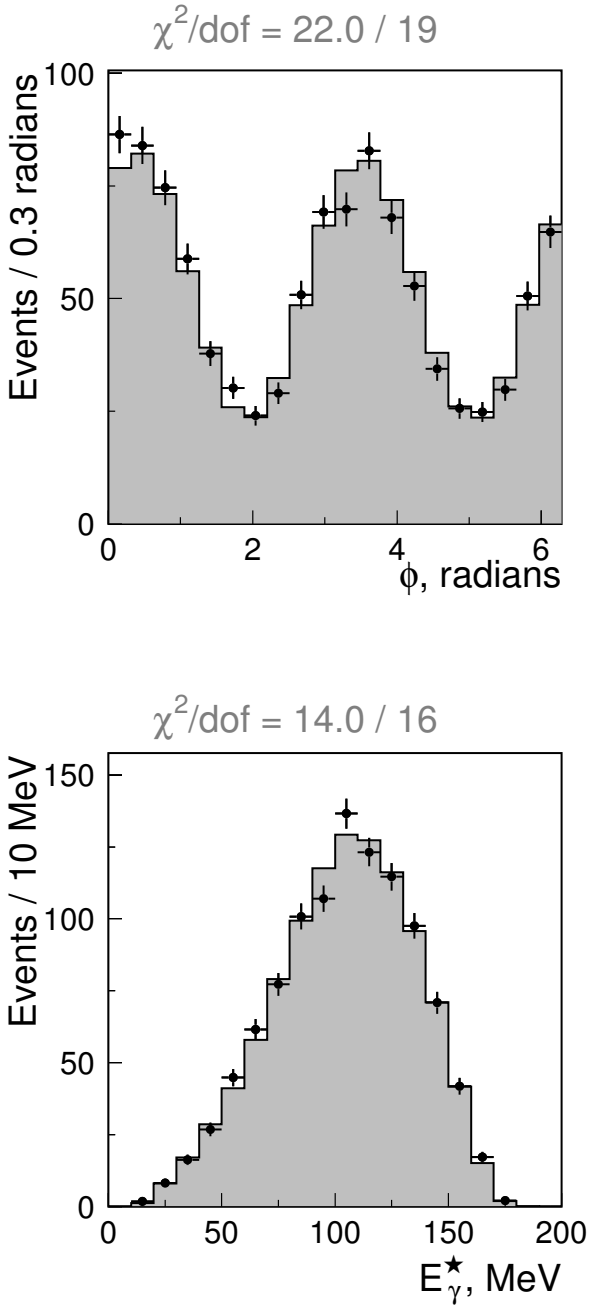

Figure 7.8: Comparison of the angle ϕ distribution (see Figure 3.4 for the definition of this angle) and the distribution of the virtual photon energy calculated in the kaon rest frame. The dots with error bars show data and the filled histogram corresponds to the Monte Carlo simulation based on the model with parameter values obtained from the maximum likelihood fit.

variable	χ^2	DOF	p-value, %
$M_{\pi\pi}$	7.7	17	97
$cos\theta_{\pi}$	14.8	19	73
M_{ee}	15.3	18	64
$E^{\star}_{\gamma}$	14.0	16	60
$cos\theta_{e}$	18.6	19	48
ϕ	22.0	19	29

Table 7.4: The p-values for the agreement between the distributions shown on figures 7.6 to 7.8

7.1.5 The Systematic Uncertainties

After the best values of the parameters $\hat{\alpha}$ and their statistical uncertainties $\sigma(\hat{\alpha})$ were obtained, the systematic uncertainties $\eta(\hat{\alpha})$ of the measurements were estimated. The equation (7.20) shows that, aside from α, the maximum of the LF may depend on: (*i*) the data sample X_D; (*ii*) the re-weighting Monte Carlo sample X_{MC}; (*iii*) the fit input values for the floating parameters α_0; and (*iv*) the external parameters of the model β. Ideally the data X_D would contain only the decays $K_L \rightarrow \pi^+\pi^- e^+ e^-$ (with no background) and the result $\hat{\alpha}$ would depend only on the data X_D itself, regardless of the way that particular data sample was chosen. In reality, however, there is always some dependence on these other factors which results in the systematic uncertainty. There is no universal method to estimate the systematic effects, but one can always vary the the factors listed above within their own uncertainties and observe the change (if any) in the results of the analysis. The desired systematic uncertainty can then be estimated based on these observations. Both X_{MC} and X_D can be modified, by varying the selection criteria of the analysis, and the uncertainties due to data selection can

Cut	$\delta \lvert g_{CR} \rvert$	$\delta \frac{\lvert g_{E1} \rvert}{\lvert g_{M1} \rvert}$	$\delta \tilde{g}_{M1}$	$\delta \frac{a_1}{a_2}$
Kaon Mass	**0.003**	**0.008**	**0.0**	**0.01**
P_t^2	**0.0**	**0.0**	**0.05**	**0.02**
$\left[P_L^2\right]_{\pi^0}$	**0.01**	**0.0**	**0.0**	**0.0**
Assigned Error	**0.01**	**0.008**	**0.05**	**0.022**
Statistical Error	**0.013**	**0.011**	**0.12**	**0.027**

Table 7.5: The summary of systematic uncertainty due to the background present in the final data sample. Statistical uncertainty is given for comparison.

be obtained. By generating different MC samples one can vary X_{MC}, α_0 and β (the errors on the values of the parameters β constitute the external uncertainty of the model). This section summarizes the variation of the fit results due to various sources of the systematic effects.

`Background` The results of the fit may depend on the amount of the background present in the data sample (5.4). To estimate the effect of the background the three cuts, which were most effective for the background suppression: kaon mass cut, P_t^2 cut and $\left[P_L^2\right]_{\pi^0}$ cut (section 5.3.1), were varied. This changed the amount of the background in X_D together with size the data sample itself. The statistical fluctuations due to the mere change in data size would result in the uncertainty for the results of the fit, even if the sample contained no background at all. The variations in the fit result, beyond these statistical uncertainties were attributed to the effect of the background. These variations are summarized in table 7.5

Cut	$\delta \lvert g_{CR} \rvert$	$\delta \frac{\lvert g_{E1} \rvert}{\lvert g_{M1} \rvert}$	$\delta \tilde{g}_{M1}$	$\delta \frac{a_1}{a_2}$
χ^2_{vtx}	**0.002**	**0.0**	**0.0**	**0.0**
M_{ee}	**0.005**	**0.01**	**0.0**	**0.01**
z_{vtx}	**0.0**	**0.0**	**0.02**	**0.02**
$\frac{E}{P}$	**0.0**	**0.0**	**0.02**	**0.005**
E_{kaon}	**0.02**	**0.015**	**0.03**	**0.0**
Assigned Error	**0.021**	**0.018**	**0.041**	**0.022**
Statistical Error	**0.013**	**0.011**	**0.12**	**0.027**

Table 7.6: The summary of systematic uncertainty due to the variation of cuts. All cuts (section 5.3.1) were studied. In this table only those cuts are included which exhibited non-zero variation in the fit results beyond the statistical fluctuations expected from the change in the size of data sample.

`Data/MC Disagreement` The Monte Carlo simulation replicated the data, even after background subtraction, only to a certain degree (chapter 6). The remaining disagreement could have affected the results of the fit. To estimate this effect, the selection criteria applied to the data sample were varied by changing the values of all the cuts (section 5.3.1) (except the ones mentioned in the background systematics). The systematic uncertainties due to the cut variation are summarized in table 7.6

N_{MC} The finite size of the re-weighting Monte Carlo sample contributes a small uncertainty as shown in figure 7.1 for the $N_{MC} = 256 \cdot N \approx 1.3 \cdot 10^6$(section 7.1.2).

α_0 Another possible systematic effect was due to the choice of the α_0 for the re-weighting Monte Carlo sample used in the fit. To estimate this effect the

value of α_0 was varied according to the equation (7.24) and the fits of the data were performed with each of the new re-weighting samples.

β Finally, the values of the invariant amplitude parameters β (7.6) were obtained from other experiments and had finite accuracy (section 3.2). To estimate the corresponding uncertainties in the fit result these parameters were varied within their errors and different re-weighting Monte Carlo samples, corresponding to each parameter variation, were generated. These MC samples were then used to perform the fit to the data and the variations in the results represented the systematic uncertainties. The functions $\delta_0^0(M_{\pi\pi})$ and $\delta_1^1(M_{\pi\pi})$, see equations (3.26) to (3.30), were varied within the data errors shown on figure 3.3. Since $\delta_1^1(M_{\pi\pi})$ is positive definite and becomes small for small values of $M_{\pi\pi}$, it was varied only in one direction.

The results of *all systematic uncertainties* are summarized in the table 7.7.

7.1.6 The Upper Limit on $\frac{|g_{E1}|}{|g_{M1}|}$

Although the fits were performed by floating simultaneously all the parameters α, the case of $\frac{|g_{E1}|}{|g_{M1}|}$ required additional work since the best estimated value was consistent with zero and this parameter must be positive. The distribution of the fit results for simulated experiments in this case was clearly non-Gaussian (figure 7.9). For this parameter the *upper limit* was estimated according to the procedure suggested in the reference [66].

To set the upper limit at 90% *confidence level* (CL), four additional statistically independent sets of 256 simulated experiments were generated. Each set was generated with the best values for all parameters, see table 7.1, except for $\frac{|g_{E1}|}{|g_{M1}|}$, whose values were chosen as follows:

$$\frac{|g_{E1}|}{|g_{M1}|} = 0.05,\ 0.10,\ 0.15,\ 0.20\ . \tag{7.32}$$

Systematic Effect	Parameters' Variations			
	$\delta\,\lvert g_{CR}\rvert$	$\delta\frac{\lvert g_{E1}\rvert}{\lvert g_{M1}\rvert}$	$\delta\tilde{g}_{M1}$	$\delta\frac{a_1}{a_2}$
Background	**0.01**	**0.008**	**0.05**	**0.022**
Variation of Cuts	**0.021**	**0.018**	**0.041**	**0.022**
Bias	**0.002**	**0.01**	**0.028**	**0.0**
Variation of α_0	**0.001**	**0.001**	**0.02**	**0.005**
Limited MC	**0.001**	**0.001**	**0.01**	**0.002**
$\Delta\eta_{+-}$	**0.002**	**0.0002**	**0.01**	**0.0001**
$\Delta\Phi_{+-}$	**0.0002**	**0.0005**	**0.002**	**0.0003**
$\Delta\delta'$s	**0.001**	**0.0003**	**0.004**	**0.001**
Total Systematic Error $\eta\,(\hat{\alpha})$	**0.023**	**0.023**	**0.08**	**0.032**
Statistical Error $\sigma\,(\hat{\alpha})$	**0.014**	**0.024**	**0.12**	**0.027**

Table 7.7: The summary of systematic and statistical uncertainties for the estimation of the parameters $\alpha = \left(\lvert g_{CR}\rvert\,, \frac{\lvert g_{E1}\rvert}{\lvert g_{M1}\rvert}, \frac{a_1}{a_2}, \tilde{g}_{M1}\right)$.

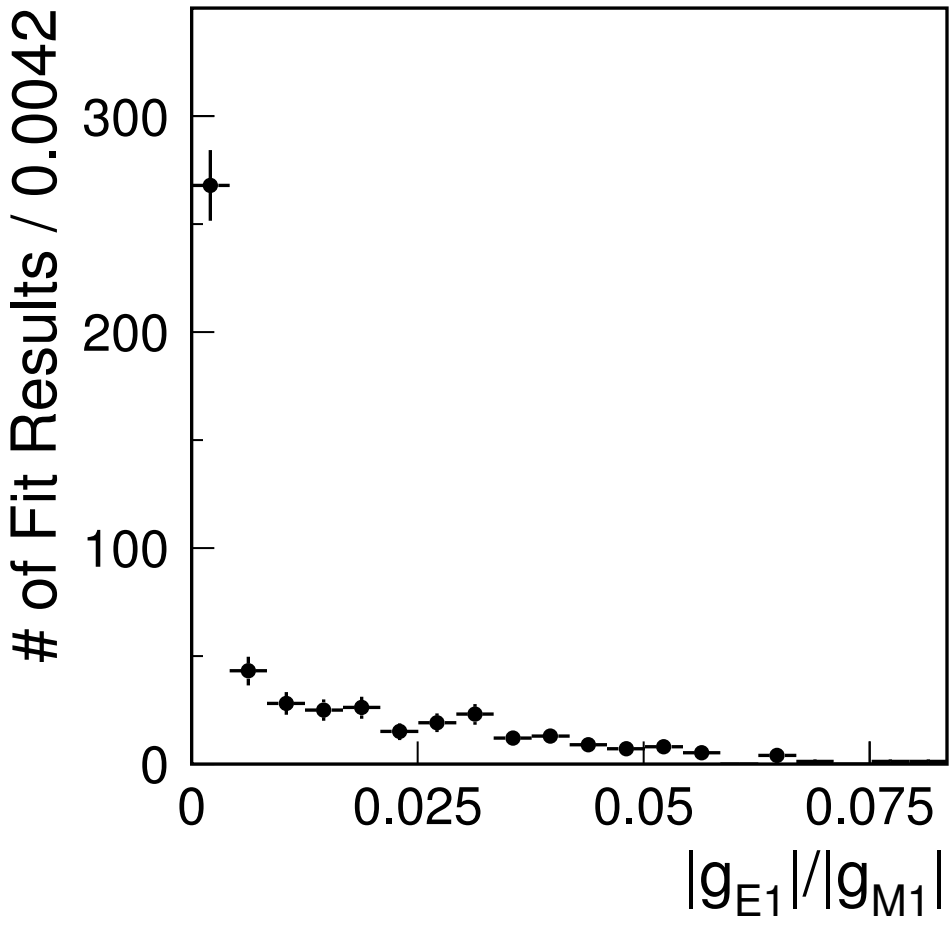

Figure 7.9: Distribution of the $\frac{|g_{E1}|}{|g_{M1}|}$fit results for the 512 simulated experiments.

Each simulated experiment in these sets was fitted in the same way as data and the best $\frac{|g_{E1}|}{|g_{M1}|}$ was estimated as the most probable value from the distribution of the fit results. These distributions were inspected to obtain the limits below[5] which $\mathbf{10\%}$ of the fit results fell for each value of $\frac{|g_{E1}|}{|g_{M1}|}$. The results of the fits and the corresponding limits are shown in the figure 7.10.

To include the systematic uncertainty on $\frac{|g_{E1}|}{|g_{M1}|}$, the systematic effects were assumed to be *essentially Gaussian* and the systematic uncertainty at the $\mathbf{90\%}$ CL was calculated as follows

$$\boldsymbol{\delta}\frac{|\boldsymbol{g_{E1}}|}{|\boldsymbol{g_{M1}}|}_{\boldsymbol{syst\ (90\%\ CL)}} \approx \mathbf{1.28 \cdot 0.023 = 0.029}\ , \tag{7.33}$$

taking the $\mathbf{0.023}$ value at the $\mathbf{68\%}$ CL from the table 7.7 and using the fact that for Gaussian distribution, the area of the tail located $\mathbf{1.28\sigma}$ away from the mean contains $\mathbf{10\%}$ of the total area of the distribution. This uncertainty was then added in quadrature to the statistical uncertainty obtained as the difference between the best value of $\frac{|g_{E1}|}{|g_{M1}|}$ and the $\mathbf{90\%}$ limit for each set of the simulated samples, see figure 7.10. The resulting error obtained in that way was treated as the total uncertainty on the parameter $\frac{|g_{E1}|}{|g_{M1}|}$ and was subtracted from the best value to obtain the total limit below which $\mathbf{10\%}$ the fit results would fall. The limits were then fitted to a line to obtain the $\mathbf{90\%}$ confidence level boundary for the upper limit estimation, see figure 7.11:

$$\frac{|\boldsymbol{g_{E1}}|}{|\boldsymbol{g_{M1}}|} < \mathbf{0.04\ (90\%\ CL)}\ . \tag{7.34}$$

The distributions of the fit results for the simulated experiments shown in figure 7.10 were also used to estimate the statistical uncertainty given in the table 7.1 (section 7.1.3).

[5] For the upper limit on the estimated parameter.

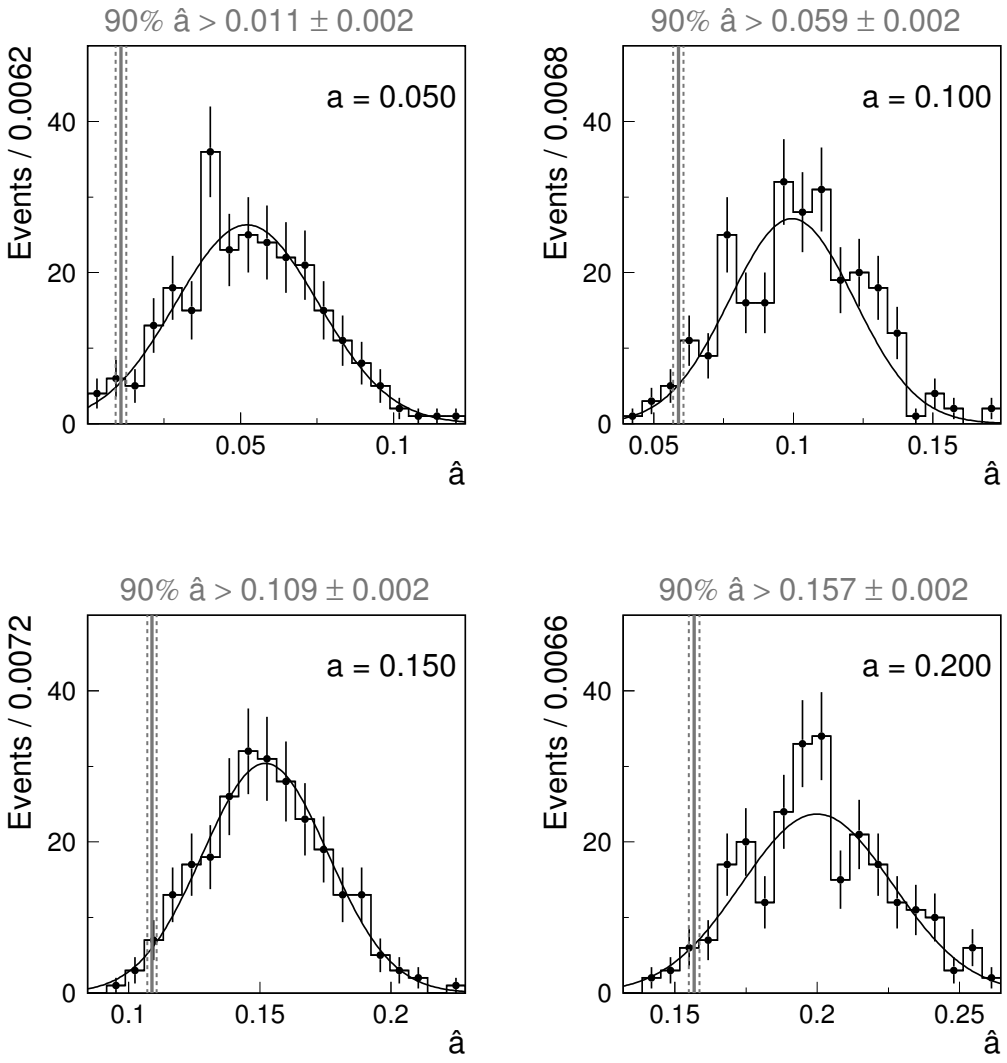

Figure 7.10: Distribution of the $\frac{|g_{E1}|}{|g_{M1}|}$ fit results for the four statistically independent sets of 256 simulated experiments ($\hat{\mathbf{a}}$ on the plots stands for the estimated value of $\frac{|g_{E1}|}{|g_{M1}|}$). Each set was generated with different values of $\frac{|g_{E1}|}{|g_{M1}|}$, see (7.32). In all four plots $\mathbf{10\%}$ of the fit results fall to the left of the solid vertical line. The effect of systematic uncertainties is included. The dashed lines show the statistical uncertainty of the vertical line due to the fact that only 256 fits were performed.

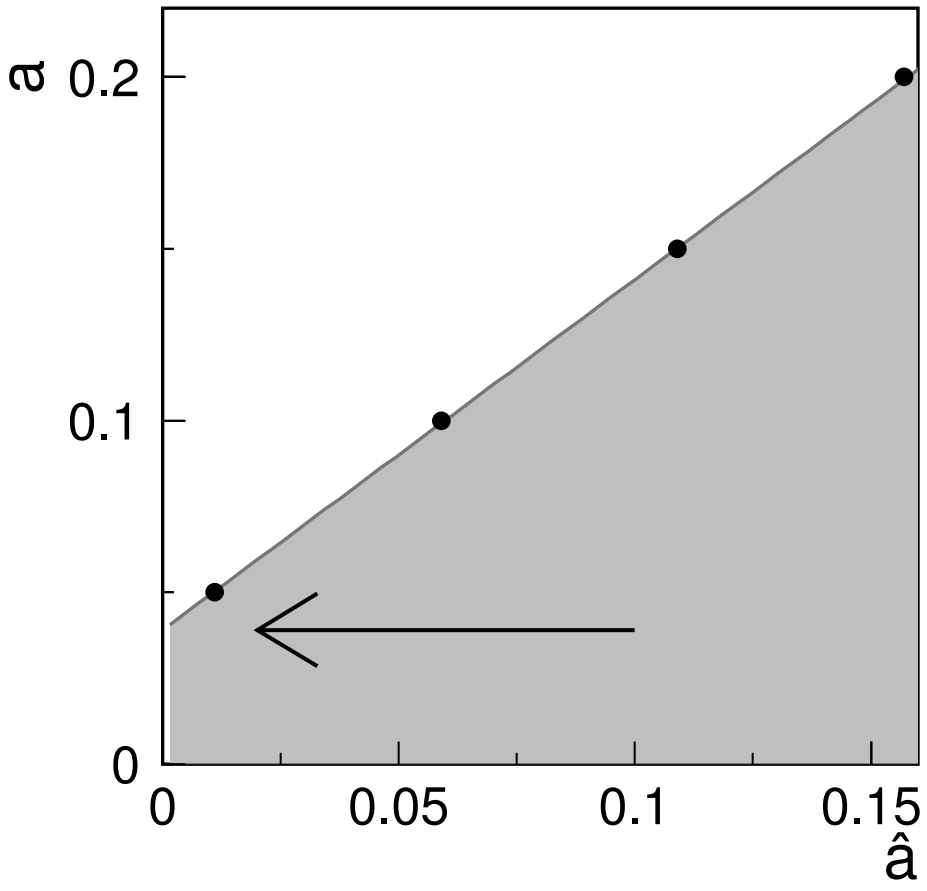

Figure 7.11: The 90% confidence level boundary for the upper limit on $\frac{|g_{E1}|}{|g_{M1}|}$. The letter $\hat{\mathbf{a}}$ stands for the estimated value of $\frac{|g_{E1}|}{|g_{M1}|}$ and $\mathbf{a}$ for the true value. The dots correspond to the four pairs of these values shown on figure figure 7.10). The shaded area contains 90% of all the fit results of the simulated experiments. The arrow shows the upper limit (7.34) corresponding to the zero value of $\frac{|g_{E1}|}{|g_{M1}|}$ estimated from the data.

7.1.7 Calculation of $\langle|g_{M1}|\rangle_{E^\star_\gamma}$, $\langle|g_{E1}|\rangle_{E^\star_\gamma}$ and $\left\langle r^2_{K^0}\right\rangle$

The averages of magnetic and electric dipole form-factors $\langle|g_{M1}|\rangle_{E^\star_\gamma}$ and $\langle|g_{E1}|\rangle_{E^\star_\gamma}$ and the mean square charge radius of K^0 $\left\langle r^2_{K^0}\right\rangle$ could be calculated with the measured values of parameters $\hat{\alpha}$ and their uncertainties $\sigma(\hat{\alpha})$ and $\eta(\hat{\alpha})$. The energy dependence of the form factor $|g_{M1}|$ is defined by equation (8.15). The estimated values of $\tilde{g}_{M1}$ and $\frac{a_1}{a_2}$ were used along with the errors and correlations from tables 7.1, 7.3 and 7.7 to measure the average value of this form factor over the range of energies of the virtual photon $E^\star_\gamma$ observed in the $K_L \to \pi^+\pi^-e^+e^-$ data sample. The result for the average $\langle|g_{M1}|\rangle_{E^\star_\gamma}$ is

$$\langle|g_{M1}|\rangle_{E^\star_\gamma} = 0.74 \pm 0.04 \tag{7.35}$$

This result along with the upper limit for $\frac{|g_{E1}|}{|g_{M1}|}$ (7.34) were used to estimate the upper limit on $\langle|g_{E1}|\rangle_{E^\star_\gamma}$:

$$\begin{aligned}\langle|g_{E1}|\rangle_{E^\star_\gamma} &< \frac{|g_{E1}|}{|g_{M1}|}\cdot\langle|g_{M1}|\rangle_{E^\star_\gamma} \\ &= 0.04\cdot(0.74+1.28\cdot 0.04) \\ &\approx 0.03\ (90\%\ CL)\end{aligned} \tag{7.36}$$

Finally, the result for the $|g_{CR}|$ was used to calculate the mean square charge radius of K^0 from the defining equation (3.24) as suggested in reference [8]

$$\left\langle r^2_{K^0}\right\rangle = -\frac{3\cdot|g_{CR}|}{M_K^2} \tag{7.37}$$

where M_K is the kaon mass. After including the errors from tables 7.1, and 7.7 I obtained the following result for the mean square charge radius of K^0 :

$$\left\langle r^2_{K^0}\right\rangle = [-0.077 \pm 0.007(stat) \pm 0.011(syst)]\ \ (fm)^2 \tag{7.38}$$

7.2 The Asymmetry Analysis

The best values of the parameters $\hat{\alpha}$, obtained in the section 7.1 (table 7.1), were used in the Monte Carlo simulation to calculate the acceptance for the measurement of the CP-violating decay-plane asymmetry introduced in section 3.3. The asymmetry analysis is described in the following sections.

7.2.1 The Observation of CP-Violating Asymmetry

To observe the CP-violating asymmetry, the final $K_L \to \pi^+\pi^-e^+e^-$ data sample was divided into two subsets consisting from events with $sin\phi \cdot cos\phi > 0$ and $sin\phi \cdot cos\phi < 0$ (see (3.41) and figure 3.4 defining the angle ϕ). Figure 7.12 shows the mass distributions for these subsets. One can clearly see the asymmetry in the peak region, whereas the background shows virtually no asymmetry. The asymmetry can be measured from the distribution of the $sin\phi \cdot cos\phi$ shown in the figure 7.13.

7.2.2 The Measurement Technique

The measurement of the CP-violating asymmetry involves counting the number of events of different types. The following *notation* was used: *(i)* the calligraphic capital letter $\mathcal{N}$ denoted the number of *true* (no background) $K_L \to \pi^+\pi^-e^+e^-$ events; *(ii)* the regular capital letter N represented the observed number of events (with background); and *(iii)* the small letter n was used for the number of background events. The subscript d was used to distinguish decays $K_L \to \pi^+\pi^-e^+e^-$ which took place in the KTeV decay volume (section 4.1) from the decays obtained after all cuts (section 6.4). The "$\pm$" was the short-hand notation for $sin\phi \cdot cos\phi > 0$ and $sin\phi \cdot cos\phi < 0$, respectively; and the subscript MC was used to distinguish the Monte Carlo events from the actual data.

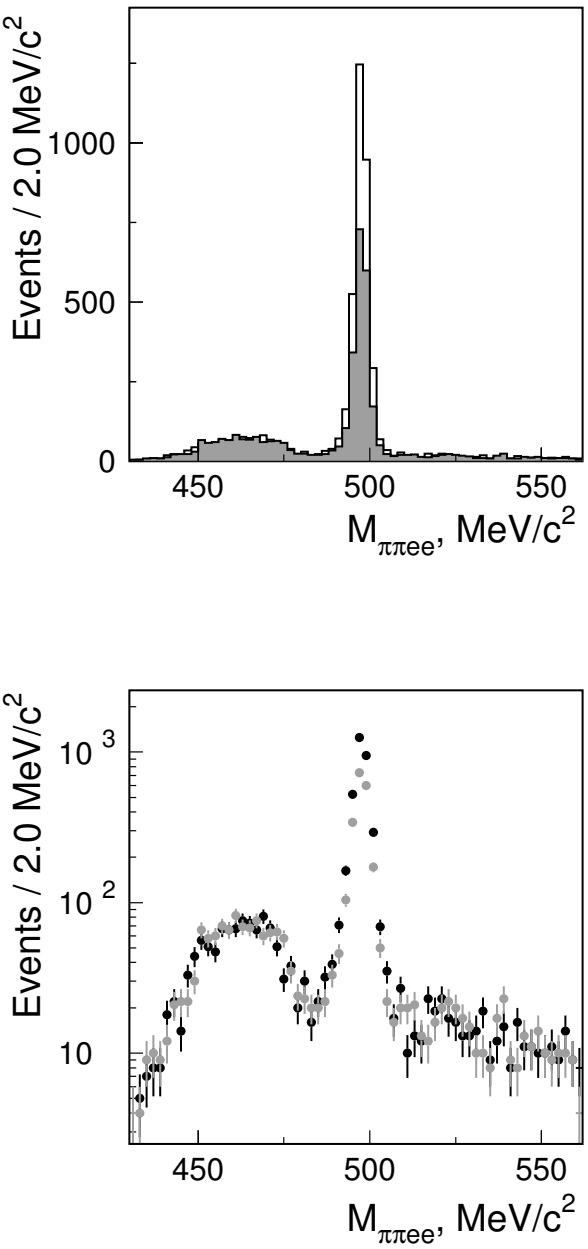

Figure 7.12: The CP-violating asymmetry is clearly observed in the peak region. On the top plot the gray histogram shows only events with $sin\phi \cdot cos\phi < 0$ and the clear histogram only the events with $sin\phi \cdot cos\phi > 0$. The bottom plot has the logarithmic abscissa and shows more clearly taht the background has no asymmetry. The gray color on both plots corresponds to events with $sin\phi \cdot cos\phi < 0$ and black to the case $sin\phi \cdot cos\phi > 0$.

The asymmetry (3.40) can be calculated using the distribution of the variable $sin\phi \cdot cos\phi$. The number of decays with $sin\phi \cdot cos\phi$ less and more than zero are counted and the asymmetry is calculated as follows

$$\mathcal{A} = \frac{\mathcal{N}_d^+ - \mathcal{N}_d^-}{\mathcal{N}_d^+ + \mathcal{N}_d^-} \tag{7.39}$$

The equation (7.39) would give the *true* value of the asymmetry if all decays, which took place in the detector, were included. What is observed directly, however, is the *raw asymmetry* calculated from the number of events after all cuts where background is present (note the regular N)

$$\mathcal{A}_{raw} = \frac{N^+ - N^-}{N^+ + N^-} \tag{7.40}$$

The asymmetry calculation therefore must include *correction for the acceptance and background*. To calculate the acceptance a Monte Carlo simulation of these decays was generated (chapter 6) with the best values of the fit parameters (section 7.1.3). The acceptance was assumed to be the same for data and Monte Carlo events:

$$a \equiv \frac{\mathcal{N}}{\mathcal{N}_d} = \left(\frac{\mathcal{N}}{\mathcal{N}_d}\right)_{MC} \tag{7.41}$$

where the Monte Carlo was generated with the best values of the parameters in the invariant amplitude obtained in the section 7.1.

Assuming that the amount of background is known, the formula for the asymmetry calculation becomes more complicated:

$$\mathcal{A} \equiv A_{true} = \frac{\mathcal{N}_d^+ - \mathcal{N}_d^-}{\mathcal{N}_d^+ + \mathcal{N}_d^-} = \frac{\left(N^+ - n^+\right)/a^+ - \left(N^- - n^-\right)/a^-}{\left(N^+ - n^+\right)/a^+ + \left(N^- - n^-\right)/a^-} \tag{7.42}$$

where a^+, a^- and n^+, n^- are the acceptances and the estimated background rates for the subsets of events with $sin\phi \cdot cos\phi > 0$ and $sin\phi \cdot cos\phi < 0$. If the background has no asymmetry, i.e.

$$n^+ = n^- = n/2 \tag{7.43}$$

Subset	$\mathcal{N}_d^{MC}$	$\mathcal{N}^{MC}$	a, %
all events	52,561,100	1,231,825	2.344 $\pm$ 0.002
$sin\phi \cdot cos\phi > 0$	29,962,700	770,016	2.570 $\pm$ 0.003
$sin\phi \cdot cos\phi < 0$	22,598,400	461,809	2.043 $\pm$ 0.003

Table 7.8: The summary of acceptance calculations. The errors are statistical, i.e. they are due to the finite size of Monte Carlo samples. The $\mathcal{N}_d^{MC}$ and $\mathcal{N}^{MC}$ represent the number of generated and reconstructed Monte Carlo decays.

then the formula for the asymmetry can be simplified:

$$\mathcal{A} = \frac{(N^+ - n/2)/a^+ - (N^- - n/2)/a^-}{(N^+ - n/2)/a^+ + (N^- - n/2)/a^-} \tag{7.44}$$

7.2.3 The Asymmetry Measurement

The distribution $sin\phi \cdot cos\phi$ for the $K_L \to \pi^+\pi^-e^+e^-$ data sample is shown on figure 7.13. The number of decays with $sin\phi \cdot cos\phi$ less and more than zero was as follows:

$$N^+ = 3241 \quad N^- = 2000 \tag{7.45}$$

which corresponds to the the *raw asymmetry* value of

$$\mathcal{A}_{raw} = 24.4\% \tag{7.46}$$

This number had to be corrected for acceptance and background (section 7.2.2). The acceptance was calculated with Monte Carlo. A total of about 50 million $K_L \to \pi^+\pi^-e^+e^-$ events were generated with the best fit parameters $\hat{\alpha}$ (table 7.1). The acceptance calculation is summarized in the table 7.8. The acceptance as a function of the variable $sin\phi \cdot cos\phi$ is shown in the figure 7.13.

The background rate was estimated (5.4) in section 5.3.2

$$n = 204 \pm 14 \tag{7.47}$$

Figure 7.12 shows that the background on either side of the kaon mass peak did not depend on the sign of $sin\phi cos\phi$. Therefore the *background had no asymmetry* and could be assumed to be equally split between the datasets with different signs of $sin\phi \cdot cos\phi$. To check this assumption the estimation of background rate was done individually for each of these subsets as was done for the total data set (section 5.3.2). The background rate for each data set was the same within the statistical errors. As an additional illustration for the validity of this assumption, the $sin\phi \cdot cos\phi$ distribution for the most dominant background mode $K_L \rightarrow \pi^+\pi^-\pi^0_D$ shows zero asymmetry (figure 7.14). With all this information at hand the asymmetry was calculated according to the equation (7.44):

$$\mathcal{A} = 13.61\ \% \ . \tag{7.48}$$

7.2.4 The Statistical Uncertainty

The statistical uncertainty of the asymmetry measurement can be estimated explicitly, since the expression for the asymmetry is known. The asymmetry formula (7.39) can be transformed as follows:

$$\mathcal{A} = \frac{\mathcal{N}^+ - \mathcal{N}^-}{\mathcal{N}^+ + \mathcal{N}^-} = 2\frac{\mathcal{N}^+}{\mathcal{N}} - 1 \ , \tag{7.49}$$

where the total number of true, i.e background-subtracted and acceptance-corrected, true data events

$$\mathcal{N} = \mathcal{N}^+ + \mathcal{N}^- \tag{7.50}$$

The variance for of the asymmetry value is then

$$\sigma^2(\mathcal{A}) = \overline{\mathcal{A}^2} - \overline{\mathcal{A}}^2 = 4\frac{\overline{\mathcal{N}^{+2}} - \overline{\mathcal{N}^+}^2}{\mathcal{N}^2} = 4\frac{\mathcal{N}x(1-x)}{\mathcal{N}^2} \tag{7.51}$$

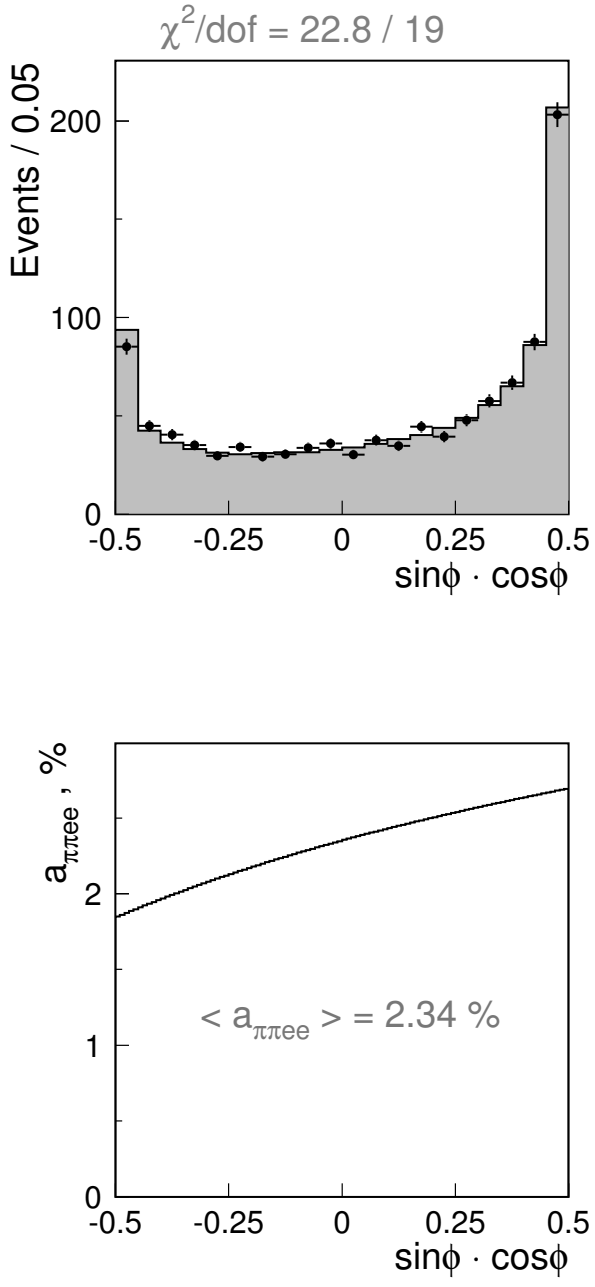

Figure 7.13: The $sin\phi \cdot cos\phi$ distribution shows the CP-violating asymmetry, see figure 3.4 for the definition of the angle ϕ. The dots with error bars show data and the filled histogram corresponds to the Monte Carlo simulation based on the model with parameter values obtained from the maximum likelihood fit.The bottom plot shows the acceptance as a function of $sin\phi \cdot cos\phi$ obtained from the Monte Carlo.

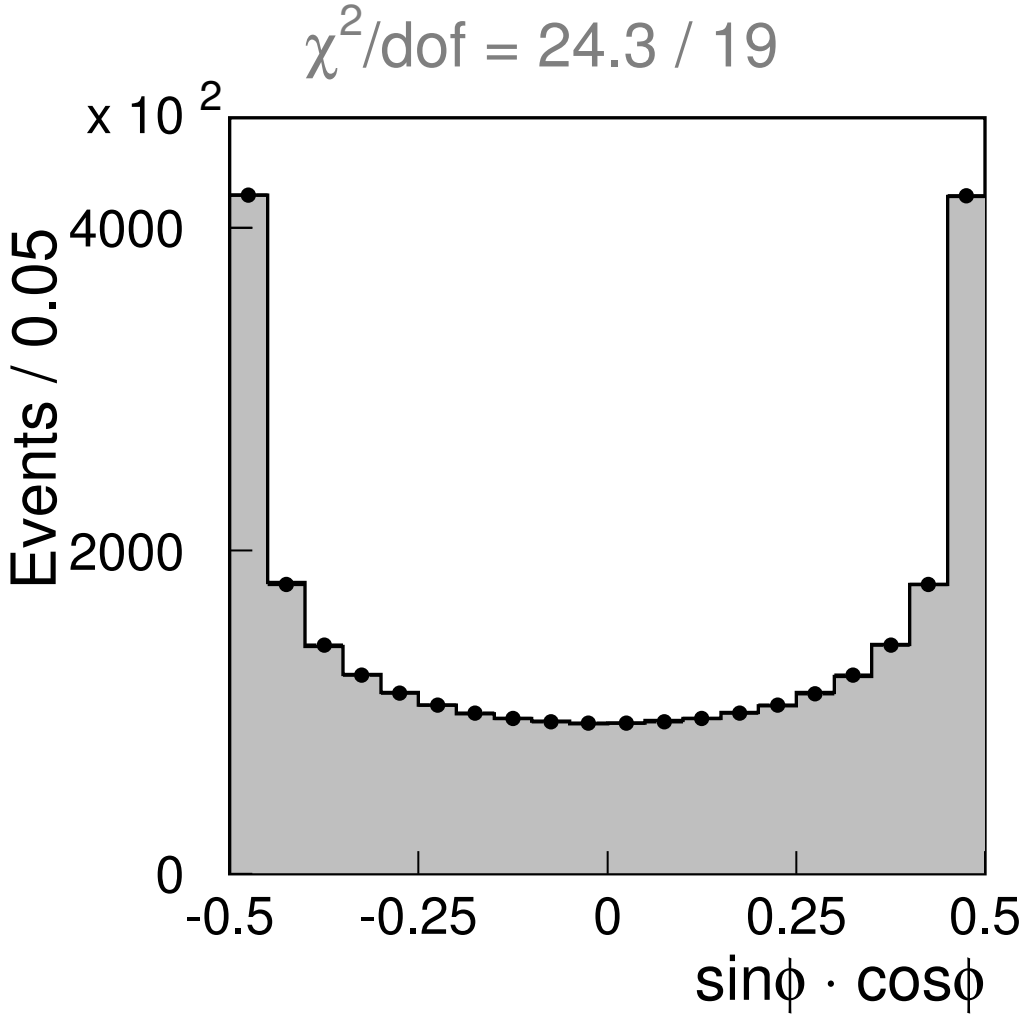

Figure 7.14: The $sin\phi \cdot cos\phi$ distribution for $K_L \to \pi^+\pi^-\pi^0_D$ decays shows no asymmetry. The dots with error bars show data and the filled histogram corresponds to the Monte Carlo simulation based on the model with parameter values obtained from the maximum likelihood fit.

where

$$\overline{\mathcal{N}^{+^2}} - \overline{\mathcal{N}^{+}}^2 = \mathcal{N}x(1-x) \tag{7.52}$$

is the variance for the number of events $\mathcal{N}^+$, which according to the equation (7.50) is governed by a *binomial* distribution with success probability (which in this case could be defined as the probability to obtain $sin\phi \cdot cos\phi > 0$) equal to $x \approx \frac{\mathcal{N}^+}{\mathcal{N}} = \frac{\mathcal{A}+1}{2}$, see equation (7.49). Therefore the following equation can be used to estimate the uncertainty

$$\sigma(\mathcal{A}) = \frac{2\sqrt{x(1-x)}}{\sqrt{\mathcal{N}}}\,. \tag{7.53}$$

Figure 7.15 shows the function in the numerator ploted versus the argument x. For the asymmetry $\mathcal{A} = (13 \pm 2)\%$ the value of that function can be approximated by unity and the final expression for the uncertainty on the asymmetry value becomes

$$\sigma(\mathcal{A}) = \frac{1}{\sqrt{\mathcal{N}}} = \frac{1}{\sqrt{5037}} \approx 1.40\%\,. \tag{7.54}$$

7.2.5 The Systematic Uncertainty

The systematic uncertainty in the asymmetry value was estimated from

studies similar to the likelihood analysis (section 7.1.5). According to the formula (7.44) the value of the asymmetry depends on the estimation for the background rate. The uncertainty due to the background subtraction was evaluated in *two* different ways. *First*, by analogy with systematics for the parameter estimation (section 7.1.5), the following three cuts were varied: kaon mass M_K cut, P_t^2 cut and $\left[P_L^2\right]_{\pi^0}$ cut (section 5.3.1). These cuts were most effective for the background suppression (table 5.2) and their variation changed the amount of the background in the final data sample, along with the size of the data sample itself. The statistical fluctuations due to the change in the size of the data sample would

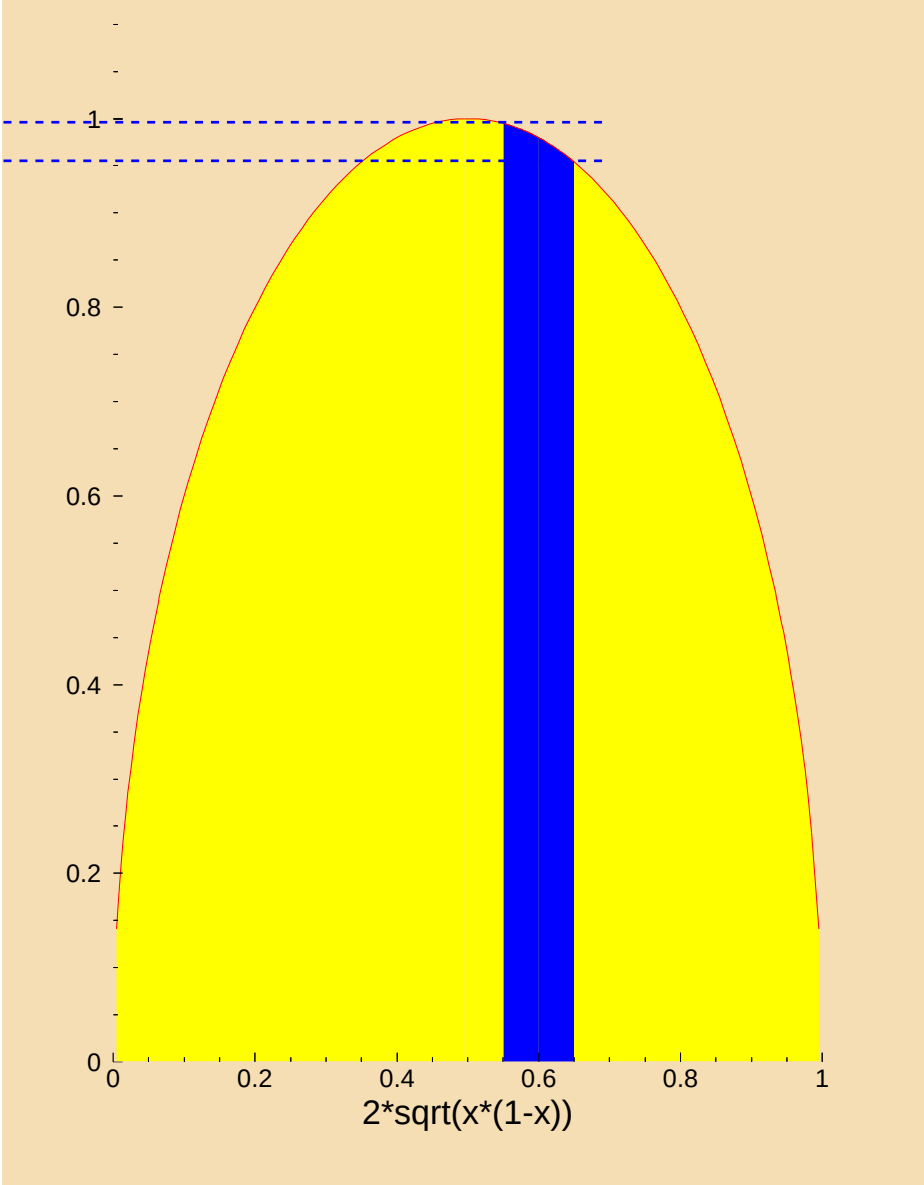

Figure 7.15: Function $2\sqrt{x(1-x)}$ used in the estimation of the statistical error on the asymmetry $\mathcal{A}$. The region $x \approx \frac{\mathcal{N}^+}{\mathcal{N}} = \frac{(\mathcal{A}\pm\delta\mathcal{A})+1}{2}$ corresponds to the value of the function approximately equal to unity.

result in the uncertainty in the results of the asymmetry calculation even when no background was present at all (Cf. section 7.1.5). In this case the expected statistical uncertainty due to the change of the data samples could be estimated by using the following expression:

$$\sigma^2(\mathcal{A}_2 - \mathcal{A}_1) = \frac{N_1}{(N_0 + N_1)^2} + \frac{N_2}{(N_0 + N_2)^2} \tag{7.55}$$

In other words, if $N_{old} = N_0 + N_1$ and $N_{new} = N_0 + N_2$ correspond to the number of events after the old and new analyses, then the expected statistical error on the asymmetry difference can be found using that formula.

The variations in the asymmetry measurement, beyond the expected statistical uncertainties were attributed to the presence of background. These systematic variations are summarized in table 7.9. *Alternatively* the number n in the asymmetry formula (7.44) was varied simply by ± 14 according to the uncertainty in the background rate estimation (5.4) and the shift in the asymmetry value was checked. The uncertainty estimated in this way was the same as the one shown in table 7.9.

The Monte Carlo simulation was used to calculate the acceptance and any disagreement between data and Monte Carlo could have affected the results of the asymmetry measurement. To estimate this effect, the remaining selection criteria applied to the data sample (i.e. all the other cuts, except the ones used for the background systematics) were varied. Any *systematic shifts* beyond the statistical fluctuations (7.55) expected due to the change in size of the data sample, are summarized in the table 7.10.

Finally, the invariant amplitude parameters α and β were varied within their errors (see section 3.2 and table 7.7) to generate different Monte Carlo samples, which were used in the acceptance calculation (section 7.2.2). The shifts in the asymmetry measurements were interpreted as the systematic uncertainties due to

Cut	*variation range*	$\delta\mathcal{A}$, %
MKAON	$(0.497,\ 0.499) - (0.482,\ 0.514)\ GeV/c^2$	0.0
TPT2ONE	$(1.0 - 10.0) \times 10^{-5}\ GeV^2/c^2$	0.0
LPOKIN	$-0.07 - 0.0\ GeV^2/c^2$	0.3
Assigned Error		0.3
Statistical Error		1.40

Table 7.9: The summary of systematic uncertainty on the asymmetry due to the background subtraction. See section 5.3.1 for the meaning and the nominal values of the cuts.

Cut	*variation range*	$\delta\mathcal{A}$, %
VTXCHI	$3 - 30$	0.4
MAGOFF for π's	$0.0007 - 0.005\ m$	0.3
EKAON	$70 - 200\ GeV$	0.5
Assigned Error		0.71
Statistical Error		1.40

Table 7.10: The summary of systematic uncertainty in the asymmetry value due to the variation of selection criteria. See section 5.3.1 for the meaning and the nominal values of the cuts.

systematic effect	$\delta\mathcal{A}$, %
Background	**0.3**
Variation of Cuts	**0.71**
$\delta\eta_{+-}$	**0.163**
$\delta\Phi_{+-}$	**0.111**
$\delta\delta$'s	**0.325**
$\delta\frac{\lvert g_{E1}\rvert}{\lvert g_{M1}\rvert}$	**0.326**
$\delta\tilde{g}_{M1}$ $\delta\frac{a_1}{a_2}$	**0.335**
$\delta\lvert g_{CR}\rvert$	**0.335**
Total Systematic Error η ($\mathcal{A}$)	**1.46**
Statistical Error σ ($\mathcal{A}$)	**1.40**

Table 7.11: The summary of systematic and statistical uncertainties in the asymmetry measurement.

the finite precision on the parameters. Note, that the functions $\delta_0^0(M_{\pi\pi})$ and $\delta_1^1(M_{\pi\pi})$ (3.26) – (3.30) were varied within the data errors shown in figure 3.3. Since $\delta_1^1(M_{\pi\pi})$ is positive definite and becomes small for small values of $M_{\pi\pi}$, it was varied only in one direction.

The results of *all systematic uncertainties* are summarized in the table 7.11.

Chapter 8

Discussion of Results

The main results of this thesis are the measurements of CP-violating effects in the decay $K_L \to \pi^+\pi^-e^+e^-$ (chapter 3) and the measurement of the K^0 charge radius using these decays. Specifically, the unique CP-violating decay-plane asymmetry was measured along with the parameters of individual contributions to the decay invariant amplitude: (*i*) CP-conserving magnetic dipole direct emission form factor, (*ii*) CP-conserving K^0 charge radius transition amplitude and (*iii*) an upper limit for the CP-violating electric dipole direct emission amplitude. The measurements were obtained from the world's largest $K_L \to \pi^+\pi^-e^+e^-$ data sample (chapter 5) accumulated by the KTeV experiment (chapter 4) at Fermilab.

These measurements and their implications are discussed in this chapter. The results are summarized (section 8.1) and compared to the previously published measurements (section 8.2) and theoretical calculations (section 8.3).

8.1 The Summary of Results

In the analysis of the rare decay mode $K_L \to \pi^+\pi^- e^+ e^-$ presented in this thesis,

$$N = 5241 \tag{8.1}$$

candidate events were selected from the entire KTeV dataset (section 5.3.1). This data sample included an estimated background of

$$n = 204 \pm 14 \tag{8.2}$$

events (section 5.3.2). The data was analyzed using the method of maximum likelihood to obtain parameters of the decay invariant amplitude (section 7.1). Namely, coefficients of the magnetic dipole (M1) direct emission form factor (8.15)

$$\tilde{g}_{M1} = 1.11 \pm 0.12(stat) \pm 0.08(syst) \tag{8.3}$$

$$\frac{a_1}{a_2} = [-0.744 \pm 0.027(stat) \pm 0.032(syst)] \ (GeV)^2 \tag{8.4}$$

and the amplitude of K^0 charge radius (CR) transition (3.24)

$$|g_{CR}| = 0.163 \pm 0.014(stat) \pm 0.023(syst) \tag{8.5}$$

were measured; and an upper limit for the CP-violating electric dipole (E1) direct emission process

$$\frac{|g_{E1}|}{|g_{M1}|} < 0.04 \ (90\% \ CL) \tag{8.6}$$

was determined. The result for g_{CR} allowed to calculate the approximate value of the mean square charge radius of K^0 , using the relationship (7.37)

$$\left\langle r^2_{K^0} \right\rangle = [-0.077 \pm 0.007(stat) \pm 0.011(syst)] \ (fm)^2 \tag{8.7}$$

in a novel way. Using the measured values for the parameters $\tilde{g}_{M1}$, $\frac{a_1}{a_2}$ and $\frac{|g_{E1}|}{|g_{M1}|}$ and the matrix of their correlations (table 7.3), the averages of $|g_{M1}|$ and $|g_{E1}|$ over the observed range of energies of the e^+e^- pair were calculated

$$\langle |g_{M1}| \rangle_{E^\star_\gamma} = 0.74 \pm 0.04 \tag{8.8}$$

$$\langle |g_{E1}| \rangle_{E^\star_\gamma} < 0.03 \ (90\% \ CL) \ . \tag{8.9}$$

Finally, using the above values for the individual contributions in the invariant amplitude of the decay, the CP-violating decay-plane asymmetry (section 3.3) was measured

$$\mathcal{A} = [13.6 \pm 1.4(stat) \pm 1.5(syst)] \ \% \ . \tag{8.10}$$

8.2 The Comparison to Previous Measurements

The comparisons of the results from this thesis to previously published measurements are summarized in tables 8.1 to 8.4.

N	n	*comments*
46	9.4	FNAL KTeV [67]
13.5 ± 4.0	—	KEK 00[68]
1856	45	FNAL KTeV [34]
1162	36.9 ± 5.9	CERN NA48 [35]
5241	204 ± 14	*this result*

Table 8.1: The comparison of the results of this thesis for the number of $K_L \to \pi^+\pi^-e^+e^-$ candidates N and background rate estimation n with previously published measurements.

$\tilde{g}_{M1}$	$\frac{a_1}{a_2}$, GeV^2	$\langle\lvert g_{M1}\rvert\rangle_{E^\star_\gamma}$	ρ	*comments*
$1.35^{+0.20}_{-0.17}$	-0.720 ± 0.029	0.84 ± 0.10	0.89	$\pi\pi ee$ [34]
—	-0.737 ± 0.034	—	—	$\pi\pi\gamma$ [48]
$0.99^{+0.29}_{-0.28}$	$-0.81^{+0.07}_{-0.13}$	0.78 ± 0.05	0.979	$\pi\pi ee$ [35]
1.229 ± 0.094	-0.733 ± 0.016	—	0.93	$\pi\pi\gamma$ [82]
1.11 ± 0.14	-0.744 ± 0.042	0.74 ± 0.04	0.924	*this result*

Table 8.2: The comparison of the results of this thesis for the magnetic dipole direct photon emission form-factor parameters ($\tilde{g}_{M1}$, $\frac{a_1}{a_2}$ and $\langle\lvert g_{M1}\rvert\rangle_{E^\star_\gamma}$) with previously published measurements.

The parameters $\tilde{g}_{M1}$ and $\frac{a_1}{a_2}$ are strongly *correlated* (table 7.3). Therefore the comparison of these results must be done in two dimensions, taking correlations into account. Such comparison for the results listed in the table 8.2 is shown in figure 8.1. The correlation ellipses were produced using the values of *statistical* correlation coefficients between the two parameters and the *total* uncertainty on each parameter.

The values for the correlation coefficients from this result (table 7.3) and for the measurement by NA48 collaboration [35] are available explicitly. For the other measurements [34, 82] these coefficients were extracted from the correlation ellipses, which were reported along with the measurements. All the correlation coefficients ρ are listed in the table 8.2. The earlier KTeV result [34] and NA48 measurement [35] had *asymmetric errors*. For the purpose of comparison to this thesis result, the corresponding correlation ellipses in figure 8.1 were produced using the *lower* and *upper* errors, respectively for KTeV and NA48.

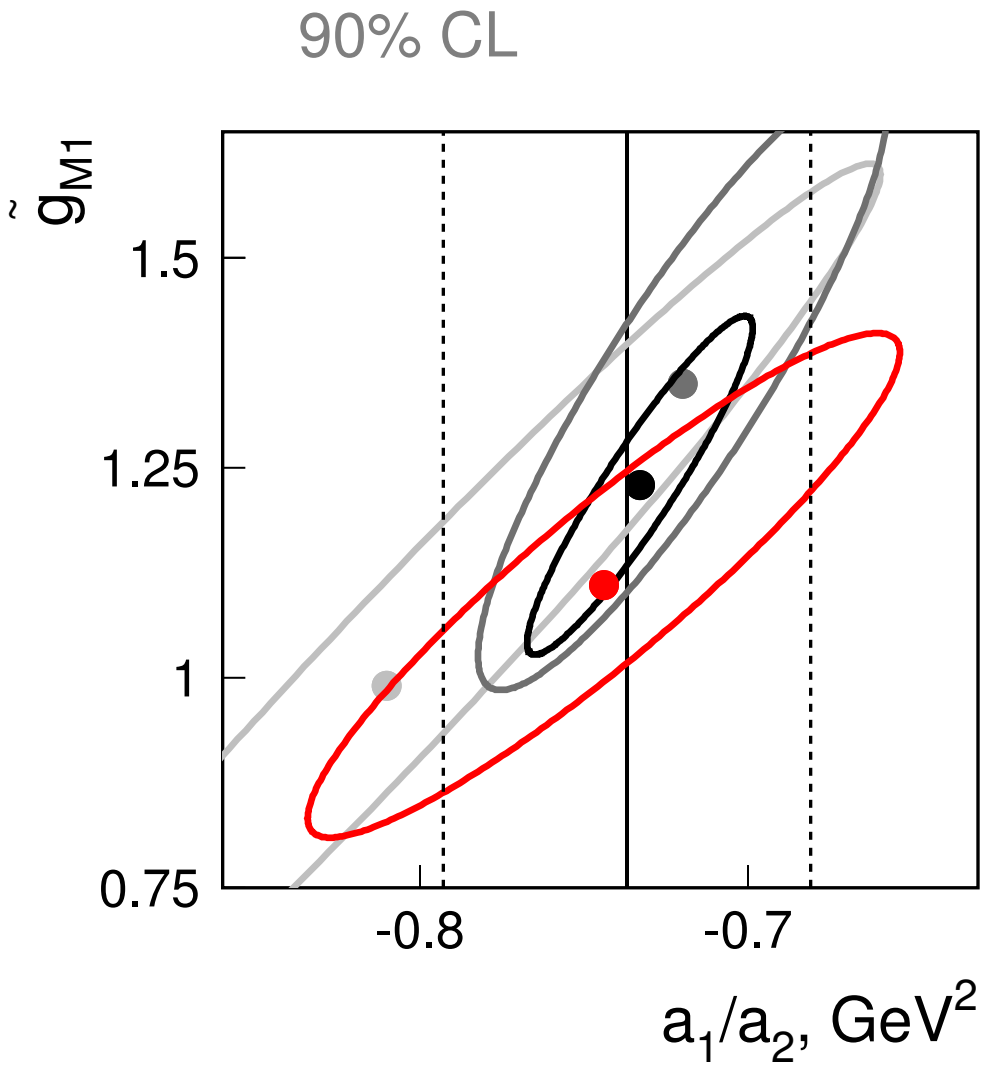

Figure 8.1: Correlation ellipses for four measurements of the magnetic form-factor parameters $\tilde{g}_{M1}$ and $\frac{a_1}{a_2}$: NA48 (light grey) [35], KTeV $'97$ (dark grey) [34], KTeV $'97 +' 99$ $\pi\pi\gamma$ (black) [82] and *this result (red)*. The KTeV $'97$ $\pi\pi\gamma$ measurement of $\frac{a_1}{a_2}$ [48] is represented by vertical strip (three lines). The ellipses and the strip correspond to 90% confidence level (CL).

$\mathcal{A}$, %	*comments*
$\mathbf{13.6 \pm 2.8}$	FNAL KTeV [34]
$\mathbf{14.2 \pm 3.6}$	CERN NA48 [35]
$\mathbf{13.6 \pm 2.1}$	*this result*

Table 8.3: The comparison of the results of this thesis for asymmetry $\mathcal{A}$ with previously published measurements.

The $\left\langle r^2_{K^0} \right\rangle$ measurements published before 2003 were based on kaon regeneration on free electrons [69, 70, 71]. The measurement from NA48 [35] used the technique presented in this thesis to extract the $\left\langle r^2_{K^0} \right\rangle$ measurement from the charge radius amplitude in the $K_L \to \pi^+\pi^- e^+ e^-$ decays.

g_{CR}	$\left\langle r^2_{K^0} \right\rangle$, fm^2	*comments*
—	$\mathbf{0.05 \pm 0.13}$	K_S regen. by electrons [69]
—	$\mathbf{0.08 \pm 0.05}$	K_S regen. by electrons [70]
—	$\mathbf{-0.054 \pm 0.026}$	K_S regen. by electrons [71]
$\mathbf{0.19 \pm 0.045}$	$\mathbf{-0.090 \pm 0.021}$	$K_L \to \pi^+\pi^- e^+ e^-$ [35]
$\mathbf{0.163 \pm 0.027}$	$\mathbf{-0.077 \pm 0.014}$	*this result*

Table 8.4: The comparison of the results of this thesis for charge radius amplitude g_{CR} and mean square charge radius of K^0 $\left\langle r^2_{K^0} \right\rangle$ with previously published measurements.

All the results are in good agreement. The precision of the measurements from

this thesis is comparable or better than that of the previously published measurements. The upper limit on the amplitude of CP-violating electric dipole direct photon emission is the first attempt at such a measurement. There are no published results of this parameter.

8.3 The Theoretical Implications

The comparisons of the results for $\left\langle r^2_{K^0}\right\rangle$ and $\langle|g_{M1}|\rangle_{E^*_\gamma}$ from this thesis to published[1] theoretical calculations are summarized in tables 8.5 and 8.6. The

$\left\langle r^2_{K^0}\right\rangle$, fm^2	*comments*
$\mathbf{-0.076}$	CM VDM [13]
$\mathbf{-0.025}$	[80]
$\mathbf{-0.087 \pm 0.046}$	VDM + DR [79]
$\mathbf{-0.049}$	ACD [78]
$\mathbf{-0.04 \pm 0.03}$	[74]
$\mathbf{-0.077}$	[73]
$\mathbf{-0.036}$	[77]
$\mathbf{-0.020}$	DSEs in QCD [75]
$\mathbf{-0.078}$	RIQM [76]
$\mathbf{-0.077 \pm 0.014}$	*this result*

Table 8.5: The comparison of the results of this thesis for mean square charge radius of K^0 $\left\langle r^2_{K^0}\right\rangle$ with previously published theoretical calculations.

K^0 charge radius is most sensitive to the mass difference between the strange

[1] An effort was made to locate as many publications as possible. However, completeness is not claimed.

and down quarks [75]. Based on a covariant Salpeter model [72] and the result for the mean square charge radius of K^0 measured in this thesis, one can estimate the lower limit on the mass difference between strange and down quarks:

$$m_s - m_d > 150\ MeV/c^2 \tag{8.11}$$

(assuming that $M_d + M_s$ to be fixed at $560\ MeV$) (figure 8.2). In addition, using the $\left\langle r^2_{K^0} \right\rangle$ result and the PDG average $\langle r_{K^+} \rangle = 0.560 \pm 0.031$ value [2], one can calculate the ratio

$$\frac{\left\langle r^2_{K^0} \right\rangle}{\left\langle r^2_{K^+} \right\rangle} = -0.246 \pm 0.052 \tag{8.12}$$

which can be used to calculate the dependence of quark masses on their sum by employing the formula [81, 83]:

$$\frac{\left\langle r^2_{K^0} \right\rangle}{\left\langle r^2_{K^+} \right\rangle} = -\frac{m_s^2 - m_d^2}{m_d^2 + 2m_s^2}\ . \tag{8.13}$$

The measured value of the mean square charge radius of K^0 supports some theoretical models: (*i*) current mixing (CM) vector dominance model (VDM) [13], (*ii*) VDM + dispersion relations (DR) [79], (*iii*) the relativistic independent quark model (RIQM) with a scaler-vector harmonic potential [76]; and disagrees with others: (*i*) anisotropic chromodynamics (ACD) theory of hadrons [78], (*ii*) calculated via a phenomenological application of the Dyson-Schwinger equations (DSEs) in QCD [75], as seen from table 8.5.

It is interesting to compare the $\left\langle r^2_{K^0} \right\rangle \approx 0.077\ fm^2$ absolute value to the Compton wavelength of K^0:

$$\frac{1}{2}\left(\frac{\lambda_{K^0}}{2\pi}\right)^2 \approx 0.07893\ fm^2\ , \qquad \frac{\lambda_{K^0}}{2\pi} \equiv \frac{\hbar}{c} \cdot \frac{1}{m_{K^0}} \tag{8.14}$$

The agreement may be coincidental, but on the other hand one may consider Compton scattering of the virtual photon on K^0as probing the size of the K^0(although in this case the factor of $\frac{1}{2}$ will need explanation).

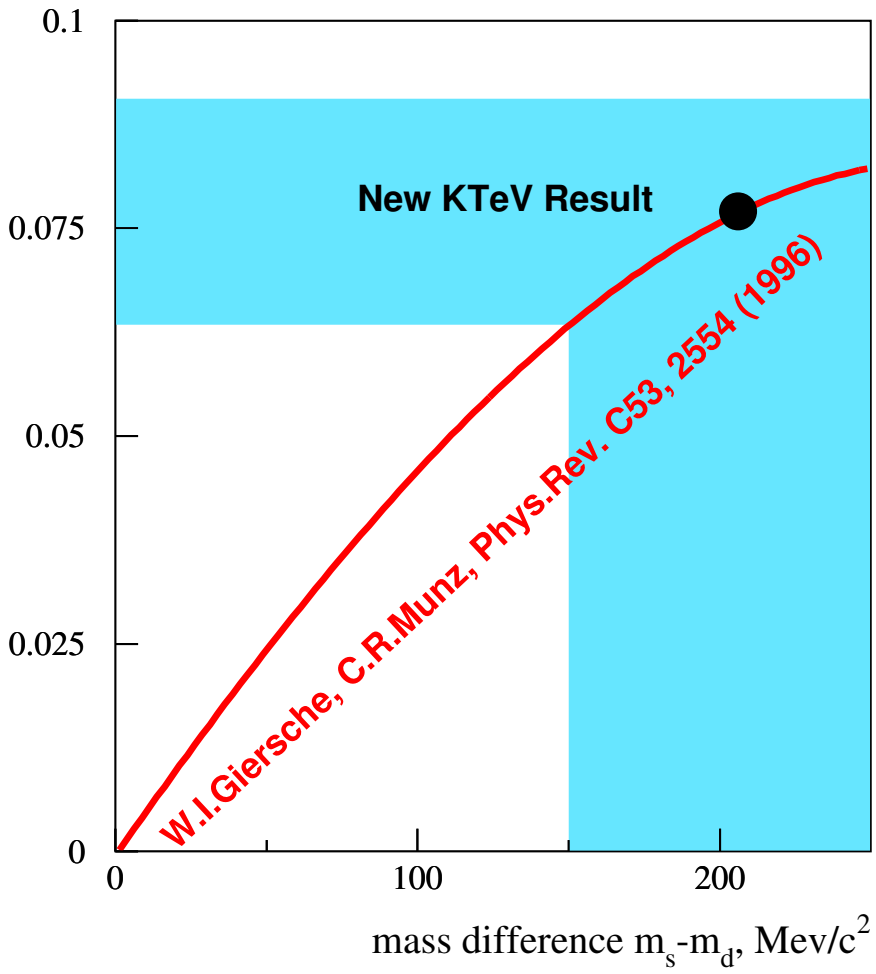

Figure 8.2: Estimation of mass difference between strange and down quarks based on a theoretical model and measurement of the mean square charge radius of K^0 .

The presence of the form factor

$$|g_{M1}| = \tilde{g}_{M1}\left[1 + \frac{a_1/a_2}{\left(M_\rho^2 - M_K^2\right) + 2M_K\left(E_{e^+} + E_{e^-}\right)}\right] \tag{8.15}$$

serves as experimental evidence for the vector dominance models [13], and favors the vector dominance model at the O(p^4) rather then O(p^6). The values of parameter a_1/a_2 could be related to the angle θ_P for the octet-singlet mixing of the pseudoscalar mesons $\eta - \eta'$ (see [14] and Section 13.2 in [1]). The average $\langle|g_{M1}|\rangle_{E^\star_\gamma}$ is in good agreement with theoretical estimation [8, 9] (table 8.6).

$\langle\|g_{M1}\|\rangle_{E^\star_\gamma}$	*comments*
$\mathbf{0.76 \pm 0.11}$	[8, 9]
$\mathbf{0.74 \pm 0.04}$	*this result*

Table 8.6: The comparison of the results of this thesis for the magnetic dipole direct photon emission form-factor parameter $\langle|g_{M1}|\rangle_{E^\star_\gamma}$ with previously published theoretical calculations.

The asymmetry value may have an impact on models in chiral perturbation theory [27, 28, 29, 30]. The measured asymmetry is in good agreement with theoretical calculation $\mathcal{A} = 14.0\%$ based on the phenomenological model [8, 9].

List of Figures

List of Tables

Bibliography

[1] K. Hagiwara *et al.* Particle Data Group Collaboration.
Review Of Particle Physics.
Physical Review D 66(1-I):1-974, 2002.

[2] S. Eidelman *et al.* [Particle Data Group Collaboration].
Review of particle physics.
Physics Letters B 592:1, 2004.

[3] R. Belusevic.
Neutral kaons.
Springer-Verlag, 1999.

[4] G. C. Branco, L. Lavoura and J. P. Silva.
CP violation.
Oxford University Press, 1999.

[5] I. I. Y. Bigi and A. I. Sanda.
CP violation.
Cambridge University Press, 2000.

[6] K. Kleinknecht.
Uncovering CP violation:
Experimental clarification in the neutral K meson and B meson.
Springer-Verlag, 2003.

[7] G. D. Rochester and C. C. Butler.
Evidence For The Existence Of New Unstable Elementary Particles.
Nature 160:855, 1947.

[8] L. M. Sehgal and M. Wanninger.
CP Violation In The Decay $K_L \to \pi^+\pi^- e^+ e^-$.
Physical Review D 46(3):1035-1041, 1992.
Erratum ibid. 46(11):5209, 1992.

[9] P. Heiliger and L. M. Sehgal.
Direct and indirect CP violation in the decay $K_L \to \pi^+\pi^- e^+ e^-$.
Physical Review D 48(9):4146-4154, 1993.
Erratum ibid. 60:079902, 1999.

[10] L. M. Sehgal.
CP and T violation in the decay $K_L \to \pi^+\pi^- e^+ e^-$ and related processes.
In J. L. Rosner and B. D. Winstein, editors, *Kaon Physics*, pages 181-187.
The Unversity of Chicago Press, 1999.
arXiv:hep-ph/9908338.

[11] A. D. Dolgov and L. A. Ponomarev.
On Possible Effects of the Violation of CP Invariance in the Radiative Decays of Neutral K Mesons.
Soviet Journal of Nuclear Physics 4:262, 1967.
Translated from *Yadernaya Fizika* 4:367, 1966.

[12] H. Chew.
Final State Interaction and CP Invariance in Radiative $K_{\pi 2}$ Decay.
Il Nuovo Cimento 26(6):1109, 1962.

[13] N. M. Kroll, T. D. Lee and B. Zumino.
Neutral Vector Mesons And The Hadronic Electromagnetic Current.
Physical Review 157:1376, 1967.

[14] Y. C. R. Lin and G. Valencia.
CP Violation In $K_L \to \pi^+\pi^-\gamma$.
Physical Review D 37:143, 1988.

[15] L. Maiani, G. Pancheri and N. Paver.
"The Daphne Physics Handbook. Vol. 1, 2".
Servizio Documentazione dei Laboratori Nazionali di Frascati, 1992.

[16] E. J. Ramberg *et al.* [E731 Collaboration].
Simultaneous measurement of K_S and K_L decays into $\pi^+\pi^-\gamma$.
Physical Review Letters 70:2525, 1993.

[17] J. Adams *et al.* [The KTeV Collaboration].
Measurement of the branching fraction of the decay $K_L \to \pi^+\pi^-e^+e^-$.
Physical Review Letters 80:4123, 1998.

[18] A. Alavi-Harati *et al.* [KTeV Collaboration].
Observation of CP violation in $K_L \to \pi^+\pi^-e^+e^-$ decays.
Physical Review Letters 84:408, 2000.

[19] Ya. B. Zel'dovich.
The transformation $K_2^0 \to K_1^0$ by electrons.
Soviet Physics JETP 9:984, 1959.

[20] L. A. Kondratyuk, L. A. Ponomarev and V. I. Zakharov.
The Decay $K_2^0 \to \pi^+\pi^-e^+e^-$ And The Radius of $K_2^0 - K_1^0$ Electromagnetic Transition.
Physics Letters B 27:655, 1968.

[21] G. Feinberg.
Electromagnetic Interaction of the Neutral K Meson.
Physical Review 109:1381, 1958.

[22] N. Cabibbo, A. Maksymowicz.
Angular Correlations in K_{e4} Decays and Determination of Low-Energy $\pi\pi$ Phase Shifts.
Physical Review 137:438, 1965.

[23] D. P. Majumdar and J. Smith.
Current Algebra, Field-Current Identity, The $K_2^0 K_1^0$ Electromagnetic Transition, And The Decays $K^0 \rightarrow \pi\pi e^+ e^-$.
Physical Review 187:2039, 1969.

[24] F. E. Low.
Bremsstrahlung Of Very Low-Energy Quanta In Elementary Particle Collisions.
Physical Review 110:974, 1958.

[25] K. M. Watson.
Some General Relations Between The Photoproduction And Scattering Of π Mesons.
Physical Review 95:228, 1954.

[26] G. Costa and P. Kabir.
Possible CP-Noninvariant Effects in $\pi\pi\gamma$ Decay of Neutral Kaons.
Il Nuovo Cimento 51:564, 1967.

[27] J. K. Elwood, M. B. Wise, M. J. Savage and J. W. Walden.
Final state interactions and CP violation in $K_L \rightarrow \pi^+\pi^- e^+ e^-$.
Physical Review D 53:4078, 1996.

[28] J. K. Elwood, M. B. Wise and M. J. Savage.
$K_L \to \pi^+\pi^-e^+e^-$.
Physical Review D 52:5095, 1995.
Erratum-ibid. 53:2855, 1996.

[29] G. Ecker and H. Pichl.
The CP-violating asymmetry in $K_L \to \pi^+\pi^-e^+e^-$.
Physics Letters B 507:193, 2001.

[30] H. Pichl.
$K \to \pi\pi e^+e^-$ decays and chiral low-energy constants.
European Physical Journal C 20:371, 2001.

[31] E. Barberio and Z. Was.
PHOTOS: A Universal Monte Carlo for QED radiative corrections: version 2.0.
Computer Physics Communications 79:291, 1994.

[32] S. Pislak *et al.* [BNL-E865 Collaboration].
A new measurement of K^+_{e4} decay and the s-Wave $\pi\pi$-scattering length a^0_0.
Physical Review Letters 87:221801, 2001.

[33] G. Colangelo, J. Gasser and H. Leutwyler.
$\pi\pi$ scattering.
Nuclear Physics B 603:125, 2001.

[34] A. Alav-Harati *et al.* [KTeV Collaboration].
Observation of CP violation in $K_L \to \pi^+\pi^-e^+e^-$ decays.
Physical Review Letters 84:408, 2000.

[35] A. Lai *et al.* [NA48 Collaboration].
Investigation of $K_{L,S} \to \pi^+\pi^- e^+ e^-$ decays.
European Physical Journal C 30:33, 2003.

[36] L. M. Sehgal and J. van Leusen.
Violation of time reversal invariance in the decays $K_L \to \pi^+\pi^-\gamma$ and $K_L \to \pi^+\pi^- e^+ e^-$.
Physical Review Letters 83:4933, 1999.

[37] K. Hanagaki.
Search for the Decay $K_L \to \pi^0\nu\bar{\nu}$.
PhD thesis, Osaka University, 1998.

[38] E. D. Zimmerman.
A Measurement of the Branching Ratio of $\pi^0 \to e^+e^-$ *using* $K_L \to 3\pi^0$ *Decays in Flight*.
PhD thesis, University of Chicago, 1999.

[39] G. E. Graham.
First Observation of the Rare Decay $K_L \to \pi^0 e^+ e^-\gamma$.
PhD thesis, University of Chicago, 1999.

[40] P. L. Mikelsons.
Search for the Decay KL to pi0 e+ e- and Study of the Decay KL to e+ e- gamma gamma.
PhD thesis, University of Colorado, 1999.

[41] A. Alavi-Harati.
Observation and Branching Fraction Measurement of $\Xi^0 \to \Sigma^+ e^-\bar{\nu}_e$ *at KTEV/E799-II*.
PhD thesis, University of Wisconsin-Madison, 1999.

[42] P. S. Shawhan.

Observation of Direct CP-Violation in $K_{S,L} \to \pi\pi$ Decays.

PhD thesis, University of Chicago, 1999.

[43] J. A. Graham.

Measurements of the Direct CP-Violating Parameter $Re\,(\varepsilon'/\varepsilon)$ and the Kaon Sector Parameters δm, τ_S and ϕ_{+-}.

PhD thesis, University of Chicago, 2001.

[44] V. Prasad.

Measurements of the Direct CP-Violation and CPT-Invariance in the Neutral Kaon System.

PhD thesis, University of Chicago, 2002.

[45] J. C. Hamm.

Study of the Rare Decay $K_L \to \pi^+\pi^-\mu^+\mu^-$ at KTeV.

PhD thesis, University of Arizona, 2002.

[46] J. R. LaDue.

Understanding Dalitz Decays of the K_L, in particular the decays of $K_L \to e^+e^-\gamma$ and $K_L \to e^+e^-e^+e^-$.

PhD thesis, University of Colorado, 2003.

[47] P. A. Toale.

A Study of the Decay $\pi^0 \to e^+e^-e^+e^-$ Using $K_L \to \pi^0\pi^0\pi^0$ Decays in Flight.

PhD thesis, University of Colorado, 2004.

[48] A. Alavi-Harati *et al.* [The KTeV Collaboration].

Study of the $K_L \to \pi^+\pi^-\gamma$direct emission vertex.

Physical Review Letters 86:761, 2001.

[49] A. Alavi-Harati *et al.* [KTeV Collaboration].
Measurements of direct CP violation, CPT symmetry, and other parameters in the neutral kaon system.
Physical Review D 67:012005, 2003.

[50] T. Kobilarcik.
Results of the Stability for the KTeV Beam.
Technical Report TM-2037, Fermilab, 1997.

[51] A. Roodman.
The KTeV Pure CsI Calorimeter.
In E. Cheu, T. Embry, J. Rutherfoord and R. Wigmans, editors, *Proceedings of the Seventh International Conference on Calorimetry In High Energy Physics*, pages 89-98.
World Scientific, 1998.

[52] J. Whitmore.
The performance of a high speed pipelined photomultiplier readout system in the Fermilab KTeV experiment.
Nuclear Instruments & Methods In Physics Research A 409:687, 1998.

[53] S. Weinberg.
New Test for Delta $\boldsymbol{\Delta I = 1/2}$ in $\boldsymbol{K^+}$ Decay.
Physical Review Letters 4:87, 1960.

[54] N. M. Kroll and W. Wada.
Internal Pair Production Associated With The Emission Of High-Energy Gamma Rays.
Physical Review 98:1355, 1955.

[55] K. O. Mikaelian and J. Smith.
Radiative Corrections To The Decay $\pi^0 \to \gamma e^+ e^-$.
Physical Review D 5:1763, 1972.

[56] F. James and M. Roos.
'Minuit' A System For Function Minimization And Analysis Of The Parameter Errors And Correlations.
Computer Physics Communications 10:343, 1975.

[57] H. Cramer.
Mathematical Methods of Statistics.
Princeton University Press, 1946.

[58] G. Cowan.
Statistical Data Analysis.
Clarendon Press, 1998.

[59] R. Raja.
A measure of the goodness of fit in unbinned likelihood fits: End of Bayesianism?
eConf **C030908** MOCT003, 2003.

[60] K. Kinoshita [BELLE Collaboration].
Evaluating quality of fit in unbinned maximum likelihood fitting.
Prepared for Conference on Advanced Statistical Techniques in Particle Physics, Durham, England, 18-22 Mar 2002

[61] J. Heinrich, Pitfalls of goodness-of-fit from likelihood.
eConf **C030908** MOCT001, 2003.

[62] W. H. Press, S .A. Teukolsky, W. T. Vettering, and B. P. Flannery.
Numerical Recipes.
Cambridge University Press, 1992.

[63] F. James.
MINUIT - Function Minimization and Error Analysis.
Reference Manual.
CERN Program Library Long Writeup D506.
CERN, 1998.

[64] R.Brun et al.
GEANT - Detector Description and Simulation Tool.
Version 3.21.
CERN, 1998.

[65] Alexander Ledovskoy, Department of Physics and Institute of Nuclear and Particle Physics, University of Virginia.
Private communication, 5 September 2001.

[66] G. J. Feldman and R. D. Cousins.
A Unified approach to the classical statistical analysis of small signals.
Physical Review D 57:3873, 1998.

[67] J. Adams *et al.* [The KTeV Collaboration].
Measurement of the branching fraction of the decay $K_L \to \pi^+\pi^- e^+ e^-$.
Physical Review Letters 80:4123, 1998.

[68] Y. Takeuchi *et al.*.
Observation of the decay mode $K_L \to \pi^+\pi^- e^+ e^-$.
Physical Letters B 443:409, 1998.

[69] H. Foeth *et al.*.
Search For Coherent Regeneration From Electrons – The K_0 Charge Radius.
Physics Letters B 30:276, 1969.

[70] F. Dydak *et al.*.
Measurement Of The Electromagnetic Interaction Of The Neutral Kaon.
Nuclear Physics B 102:253, 1976.

[71] W. R. Molzon *et al.*.
K_SRegeneration on Electrons from 30 to 100 GeV/c: A Measurement of the K^0Radius.
Physical Review Letters 41:1213, 1978. Erratum-ibid. 41:1523, 1978. Erratum-ibid. 41:1835, 1978.

[72] W. I. Giersche and C. R. Munz.
K^0 form factor and charge radius in a covariant Salpeter model.
Physical Review C 53:2554, 1996.

[73] C. R. Munz, J. Resag, B. C. Metsch and H. R. Petry.
A Bethe-Salpeter model for light mesons: Spectra and decays.
Nuclear Physics A 578:418, 1994.

[74] J. Gasser and H. Leutwyler.
Low-Energy Expansion Of Meson Form-Factors.
Nuclear Physics B 250:517, 1985.

[75] C. J. Burden, C. D. Roberts and M. J. Thomson.
Electromagnetic Form Factors of Charged and Neutral Kaons.
Physics Letters B 371:163, 1996.

[76] N. Barik, S. Kar, S. Naimuddin and P. C. Dash.
Elastic form-factors and charge radii of pi and K mesons.
Physical Review D 59:037301, 1999.

[77] F. Cardarelli, I. L. Grach, I. M. Narodetsky, E. Pace, G. Salme and S. Simula.
Hard constituent quarks and electroweak properties of pseudoscalar mesons.
Physics Letters B 332:1, 1994.

[78] L. Cosmai, M. Pellicoro and G. Preparata.
Mesons In Anisotropic Chromodynamics: The Electromagnetic Form-Factors Of Pseudoscalars.
Physics Letters B 121:272, 1983.

[79] S. Blatnik, J. Stahov and C. B. Lang.
The Isovector Part Of The Kaon Form-Factor And The Kaon Charge Radii.
Lettere al Nuovo Cimento 24:39, 1979.

[80] M. Abud, R. Lacaze and C. A. Savoy.
Properties Of Hadrons As Quark Bound States On The Null - Plane.
Nuclear Physics B 98:215, 1975.

[81] O. W. Greenberg, S. Nussinov and J. Sucher.
Quark Model Relation For Kaon Charge Radii.
Physics Letters B 72:83, 1977.

[82] J. Shields.
The Search for the Emission of a CP-Violating E1 Photon in the $K_L \to \pi^+\pi^-\gamma$ *Decay*.
PhD thesis, University of Virginia, 2005.

[83] N. Isgur.
Medium Mass Quarks And The Charge Radius Of The Neutral Kaon.
Physical Review D 17:369, 1978.